The Development of an Experimental Technique to Measure the Influence of Temperature on the Mechanical Properties of Weldments

A dissertation submitted to the Faculty of Engineering and the Built Environment at the University of Cape Town, in fulfilment of the requirements for the degree of Master of Science in Engineering

Kashir Singh

Department of Mechanical Engineering

University of Cape Town

April 2018

PLAGIARISM DECLARATION

Declaration:

1. I know that plagiarism is wrong. Plagiarism is to use another's work and pretend that it is one's own.
2. I have used the IEEE 2006 convention for citation and referencing. Each significant contribution to, and quotation in, this report from the work(s) of other people has been attributed, and has been cited and referenced.
3. This report/project is my own work.
4. I have not allowed, and will not allow anyone to copy my work with the intention of passing it off as his or her own work.

Signature…… Signed by candidate .....

ABSTRACT

In large industries, such as in power stations, welds are widely employed to join different components together to meet various property requirements. The thermal gradient that develops during welding causes an inhomogeneous distribution of material properties, in areas adjacent to the weld, known as the Heat Affected Zones (HAZ). Welded joints subjected to elevated temperatures and loads during operations often experience a degradation of mechanical properties and performance of the joint. Studies have found that mechanical phenomena's such as, fatigue and creep have compromised the structural integrity of weld zones. In essence a welded component acts as a composite material, for which it's overall performance is dependent on its weakest material component.

This study focuses on developing an experimental technique that is capable of measuring the influence of temperature on the mechanical and material properties across a weldment. The development of the experimental technique includes the design and optimisation of the hot zone of a welded tensile specimen, identification and characterisation of the different weld zones as well as, refining a strain recording strategy to detect the localised strains in each of the different weld zones. The application of the experimental technique is applied to welded components from turbine steam penetrations, which were extracted from a coal fired power station. The steam penetrations are a low Cr structural steel; (Cr 0.66, C 0.24 by wt. %) and have been in service for approximately 24 year (± 212 000 hrs).

Two primary systems namely the Gleeble 3800 thermo-mechanical simulator and digital image correlation are used in this study. In order to accurately map the in-service evolution of material properties, each of the welds were mechanically loaded in tension and exposed to elevated operating temperatures. To induce mechanical loading at constant elevated temperatures, a Gleeble 3800 thermo-mechanical simulator with a tensile module was used to deform specimens at a strain rate of 50 $\mu\varepsilon.s^{-1}$. Experiments were conducted at various temperatures, ranging from room temperature (RT) to 535 ^{o}C. The evolution of material properties across the weldment was evaluated using Digital Image Correlation (DIC). DIC is a non-contact digital technique, capable of measuring localized strain during mechanical loading at elevated temperatures.

In order to investigate the localized strain across the different weld zones, virtual strain gauges of one millimetre in length were simulated at intervals of one millimetre. It was found that there was a continuous accumulation of strain from the Fusion Line (FL) into the Parent Material (PM). This finding suggested that the HAZ nearest to the PM; which was the Fine Grained Heat Affected Zone (FGHAZ) was the weakest zone as it strained the most. The FL was found to be the least ductile region of the weld as most of the absorbed thermal energy provided during the welding process was used for strain hardening. At elevated temperatures, localised strain occurred at lower strain values than those at RT. This finding suggested that at elevated temperatures there was more thermal energy available for dislocation activation and mobilization.

The influence of temperature on the local weld zones were evaluated by extending a specimen, containing just the parent material. A simulation of a virtual strain gauge across the monolithic specimen's gauge length, revealed that necking occurred at the centre of the specimen which corresponded to the hot zone. In contrast, a simulation of virtual strain gauges across both welds revealed that necking occurred in the region between the HAZ and weld material. This finding inferred that the presence of a weld reduced the strength of the component, as the weld material was the weakest material. Furthermore, the in-service operating conditions was found to have significantly influenced the material behaviour of the welds. A weld that was exposed to a more elevated temperatures and loads, was found to have undergone a higher degree of material degradation, and strained to a larger extent when compared to a weld that was exposed to a more moderate operating environment.

ACKNOWLEDGEMENTS

To achieve something as great as this, is by no means an accomplishment of a single individual, but rather a collective accomplishment by all those who played a role in this study. I would like to extend a heart full thanks to all those who assisted and supported me throughout the duration of my study.

Firstly, I would like to express my most sincere gratitude to my supervisor, Professor Robert Knutsen for his unwavering support and supervision. I am extremely grateful for his continuous encouragement and motivation through periods when circumstances threatened the completion of my MSc. By following his expertise within the field of material science and engineering, I have acquired invaluable knowledge that will hold me in steadfast in the years to come.

I would also like to extend my appreciation to the entire Centre for Materials Engineering (CME) family, at the University of Cape Town (UCT). Under the guidance of Professor Knutsen, I was privileged enough to benefit from this friendly, comfortable, supportive and, challenging environment, created at the CME. I am eternally thankful for being a part of this environment where learning, research and, personal development occurred in a holistic manner.

I am sincerely grateful to Mr Richard Curry, for all his motivation and experienced advice. I truly appreciate all the efforts he has made in guiding me through learning about Digital Image Correlation and, for always lending a hand in solving all my technical hiccups. My appreciation also goes out to Dr Sarah George for helping with the Gleeble and, to Ms. Penny Louw for ever willing to assist me with laboratory equipment.

Furthermore, my gratitude is also extended to the Mechanical Engineering Workshop at UCT, for machining my specimens and, for accommodating the modifications that I needed. Particular recognition needs to be made to Mr Pierre Smith, Mr Hubert Tomlinson and Mr Peter Jacobs.

This project would not have been possible without the financial support and guidance from the Eskom Power Plant Engineering Institute (EPPEI) Material Science Specialisation. In addition,

my appreciation is expressed for the supplied material, and for the technical information and advice.

My studies would not have realised without the funding provided by the National Research Fund (NRF), and the Technology and Human Resource for Industry Programme (THRIP) in partnership with CME. The funding provided me with the opportunity to further develop my tertiary education in manner that also aided my personal development.

Finally, to my family...words cannot express my gratitude for your unwavering support, encouragement and inspiration that you provide in my life. I am eternally grateful!

TABLE OF CONTENTS

LIST OF FIGURES

LIST OF TABLES

LIST OF ABBREVIATIONS

CGHAZ	Coarse Grained Heat Affected Zone
DIC	Digital Image Correlation
EPPIE	Eskom Power Plant Engineering Institute
FGHAZ	Fine Grained Heat Affected Zone
FL	Fusion Line
HAZ	Heat Affected Zone
IR	Infrared
LED	Light Emitting Diode
LPW	Loop Pipe Weld
NDT	Non-destructive testing
PM	Parent Material
ROI	Region of Interest
SP	Steam Penetration
THW	Turbine Housing Weld

1 INTRODUCTION

To ensure a sustainable electricity generation capacity in South Africa, extensive efforts have been made to extend the reliability of coal fired power plants. The reliability of a power plant is directly influenced by the integrity of the individual components. As a result of long exposure periods, high pressures, and elevated temperatures, power plant components experience severe material degradation mechanisms, such as: creep, corrosion and thermo-mechanical fatigue. Monitoring and assessing these material damage mechanisms are essential to maximise plant life, and to reduce the risks of power outages.

Components that are most susceptible to material degradation are the extrados of bends in steam pipes and weld zones [1]. Weld zones are of particular concern due to the thermal gradient that develops during the welding process. The presence of a thermal gradient during welding causes an inhomogeneous distribution of material properties in areas adjacent to the weld. To fully understand the material degradation that occurs at a weld at elevated operating temperatures, knowledge of the localised performance of the individual weld zones is critical. This study focuses developing an experimental technique to record the influence of temperature on the evolution in mechanical and material properties across dissimilar low alloy welds, using Digital Image Correlation (DIC).

1.1 PROJECT BACKGROUND

Currently South Africa's electricity utility, Eskom, operates 13 coal fired power plants [2]. These coal fired power plants have been in operation for several decades and in 2014, 64 % of Eskom's coal fired power plants had past their midlife [3]. However, due to actual service conditions, component performances and material degradation, the calculated design life is not always equal to the actual life. Therefore, in order to prevent catastrophic and unforeseen failures, preventative maintenance and monitoring practices are employed. During any planned or forced outage, non-destructive testing (NDT) techniques are used to examine and test components for damage due to corrosion, erosion, fatigue and creep. By having knowledge of the damage state, component refurbishment or replacements can be accounted for, and the remaining in-service component life can be estimated.

Eskom has identified material condition assessments as a pivotal component to extend the operating lives of its fleet of coal fired power plants. In order to extend reliable plant operations, material integrity and component life management are critical. Knowledge of component life estimations allows for adequate inspection techniques, component refurbishments and/or replacements, and preventative maintenance strategies to be implemented.

Aggressive operating conditions have been found to be one of the dominant damage mechanisms that limits component life. For example, high temperature and pressure components such as boiler tubes have been found to be the largest contributor to unplanned forced outages [4]. In view of the hostile in-service environment, it was found that the cause of these tube ruptures were due to fly ash erosion which thinned the tube walls, and resulted in component failure. Material degradation of critical components limit its remnant life, and the ability to extend the service life of coal fired power plant.

Over time, material degradation at high temperature and pressure, is monitored by utilising both off and on line systems. Integrity management and continuous monitoring of induvial power plant components play a critical role in remnant life prediction calculations. At present, Eskom uses metallographic replication techniques accompanied with life estimation, and creep damage models to determine the remnant life of aged components. Capacitive and passive strain gauges are also used to enhance these calculations. Eskom currently takes about 60 000 metallographic replicas each year from approximately 1 500 different components [5]. These replicas are analysed, and the ratio of number of voids per millimetre to the number of voids per millimetre at fracture, is used to determine the time left to fracture. Extensive monitoring of scaled down welded vessels is also achieved by laboratory experiments.

This study will focus on developing an experimental technique that will be used to gain an understanding of the component behaviour, and material degradation at in-service elevated temperatures. Specimens containing a weld zone will be used to map the change in mechanical and material properties with respect to varying elevated temperatures. A thermo-mechanical simulator will be used to mimic actual industrial temperatures, and a non-contact strain based technique will be used to identify and characterize the change in properties across the different weld zones.

1.2 PROBLEM DEFINITION

Extending the reliability of a power plant requires monitoring of the remnant life of critical components. In a coal fired power plant, there are three main parameters that influences a component's life. These are: temperature, stress and material [5]. The intricate influences that these three parameters have on each other makes it difficult to accurately determine the remnant life of components, especially in inhomogeneous components where welds are present. The process of welding involves high temperatures, which causes a thermal gradient to develop across the welded region. Due to the presence of a thermal gradient, the material's microstructure is inhomogeneous, which in turn results in a spread in mechanical and material properties in areas surrounding the weld.

The remnant life estimation calculation for a welded component is not as straight forward as that of a homogeneous component. In essence, a welded component is composite in nature, and its overall performance is dependent on the strength of the individual localised zones. In service, these welded components undergo considerable material degradation. At present, Eskom assesses the remnant life of a weld by counting the voids within the localised weld zones from metallographic replication. By analysing the grain size, the localised weld zones are identified, and the voids pertaining to a specific zone are counted and reported. Metallographic replications provide useful information pertaining to the extent of material degradation. However, these replicas can only be taken at ambient conditions when the power station units are taken off-line and is therefore, not always the most suitable method to assess material degradation.

There are other techniques that are capable of monitoring the performance of a welded zone both on and off-line, namely strain gauges and extensometers. Strain gauges are capable of being connected both actively and passively, and by doing so are able to detect strains due to both the application of a load, and due to the effects of elevated temperatures. Both strain gauges and extensometers are versatile in that they both have reasonable spatial resolution of strain measurements, however, they are not suitable to detect strain in the individual localised weld zones. Another disadvantage of these two techniques is that they have been found to be inadequate for operations at high temperatures for a prolonged period of time. Strain gauges were found to have debonded at high temperatures, and although noncontact extensometers

exist, such as laser and video extensometer, these have been found to be not a viable choice for testing for extended periods of time under aggressive conditions due to cost implications.

A relatively new method of measuring surface deformation or strain is Digital Image Correlation (DIC). DIC is a noncontact strain measuring technique, with excellent full field spatial resolution of strain measurements [6]. DIC is capable of capturing highly localised strain fields across the different weld zones. The noncontact operations of DIC allows for a welded component to be exposed to elevated temperatures whilst under load, and for localised deformations to be recorded. DIC works on the basic principal of capturing digital images of a material's surface before and during mechanical loading. Thereafter, by correlating the deformation of pixels relative to the initial undeformed pixels, it is able determine strain measurements. The correlation process uses a matching algorithm that compares the grey level intensities between the undeformed and deformed images. Heating and loading of the welded components will be performed on a Gleeble thermo-mechanical simulator, which is capable of inducing a prescribed load (up to 100 kN in tension) whilst maintaining a constant elevated temperature (up to 1 600 ^{o}C). Combining the benefits of DIC with the use of a Gleeble thermo-mechanical simulator allows for a distribution of material properties to be extracted from the localised weld zones.

This study focuses on developing an experimental technique capable of measuring the mechanical and material property evolution across a weldment. An in-depth understanding of the localised material behaviour will ultimately provide useful information for component remnant life estimation models.

1.3 SCOPE AND OBJECTIVES

The overarching aim of this study is to contribute to Eskom's component material damage estimation models. This will be achieved by investigating the mechanical and material property variation of a weld zone as a function of temperature. Experiments will be conducted on aged weldments that were extracted from a coal powered power station.

The welded components had an in-service life of approximately 212 000 hours, and therefore, prolonged laboratory experimentation at elevated temperatures will not have a significant effect on the material behaviour. With this in mind, laboratory experiments were designed to be approximately an hour long. All tensile tests will be conducted within a Gleeble thermo-mechanical simulator with temperatures ranging from room temperature (RT), to 300 ^{o}C, to the operating temperature of 535 ^{o}C. A commercial two dimensional DIC system will be used to measure deformation, which will be processed on Instra-4D, and subsequently converted into strain maps using MATLAB.

The primary objective of this study is to develop an experimental technique that is capable of recording the strain deformation across the localised zones of a weldment at elevated temperature. Subsidiary objectives include:

- Designing a tensile specimen to include a weldment at its centre.
- Optimising the thermal profile of the designed tensile specimen.
- Accurately identify and characterize the different weld heat affected zones.
- Evaluating the experimental technique by monitoring the evolution in material properties across two dissimilar weldments.

2 LITERATURE REVIEW

This chapter outlines the findings of a literature review conducted on the material properties of the component to be investigated, the evolution in material and mechanical properties of a weldment, and material property extraction methods. The photomechanical extraction application of DIC is also explored in the light of high temperature tensile tests.

2.1 WELDING OF FERRITIC MATERIAL

2.1.1 WELDING PROCESS

Welding is a joining process used to fuse components together. This process is commonly employed in the engineering and production processing sectors to create high strength joints; such as in the power industry to join large industrial components [7].

In general, two materials, known as the parent materials are fused together by a selected welding material (or filler material). There are a variety of welding techniques, each characterised according to the application, function, and required properties of the weld [8]. The choice in welding technique and parameters are crucial in achieving the required strength and ductility. Welding properties such as temperature and composition of the parent material significantly affects the strength and microstructural evolution of the welded joint [9], [10].

2.1.2 CLASSIFICATION OF WELD ZONES

In order to successfully join two materials together, sufficient energy in the form of heat and/or pressure, is required to form chemical bonds between the two materials [8]. Sources of heat into the weldment arises from the various welding parameters such as: electrode feed speed, current and welding speed [11].

Melting of the base material, dilution of the filler material, and solidification of the weld causes a thermal gradient to develop across the weld zone, which, in turn gives rise to the development of material zones with different microstructural properties [11], [12]. It has been found that the

welding process reduces the material properties such as: toughness, ductility and corrosion resistance due to microstructural alternations [12].

The source of heat generation depends on which welding parameter is dominant. For example, at low electrode speeds, about 60 % of the total heat transfer is due to the arc; however, as the electrode speed increases, the source of heat transfer changes to the heat associated with the filler material droplet [11]. Similarly, Fujii et al. reported that the heat input (energy input per unit weld length) decreased with increasing welding speed; which in turn resulted in an increase in both strength and hardness [9], [12].

An inhomogeneous microstructure infers that there will be a variation in material and mechanical properties across the weld zone. The degree of variation in both material and mechanical properties is a function of the heat induced during the welding process [9], [13].

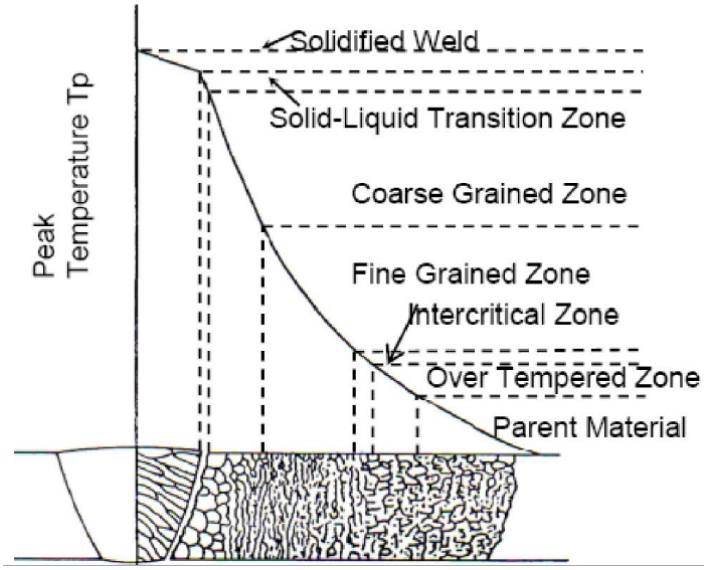

Figure 2.1.2-1: Cross-section of a butt weld, illustrating the different weld zones, the formation temperature and the evolution in microstructure [13].

Figure 2.1.2-1 illustrates the microstructural evolution across a butt weld. The classification of the different weld zones is strongly influenced by the heat transfer induced during the welding process. The highest recorded temperature in the parent material nucleates at the weld nugget, and distributes through the material creating heat affected zones (HAZ). The main features of a weld are the fusion line (FL), the coarse grained heat affected zone (CGHAZ), the fine grained heat affected zones (FGHAZ) and the unaffected parent material (PM). The FL is the region at which material fusion occurs with the highest temperature. At the FL, the dislocation density increases quickly due to small amounts of plastic deformation, however, during the

post weld heat treatment (PWHT), the dislocation density is relieved by recovery and recrystallization processes [10]. The CGHAZ is adjacent to the FL, and experiences the second highest temperature. The CGHAZ is characterised by grain coarsening [10]. The FGHAZ forms by heating into the low temperature zone of the austenitic region, and hence forms martensite during cooling. The FGHAZ is often considered as the weakest zone, as microstructural restoration processes are less significant due to it being furthest from the heat source (FL) [10].

The carbon content of a material has been found to have a strong influence on the transformation of the mechanical properties, and microstructures of a weld [9]. Microstructural changes that occur during and post welding can be mapped using the iron-carbon phase diagram. The steam penetration has a carbon content in the range of 0.23 wt. %; this is indicated on the iron-carbon phase diagram illustrated by Figure 2.1.2-2 (a). However, reference to the iron-carbon phase diagram should only be considered as a guideline since other minor alloying elements are also present in the steels in question. During the welding process, the temperature required to melt the parent materials is in the range of above 1 500 ^{o}C, which is above the 727 ^{o}C eutectoid phase transformation temperature. Thus, the microstructure during the welding process, is fully austenitic (γ) in locations close to the fusion line. As the workpiece cools post the welding process, to about 800 ^{o}C, microstructure enters the two phase region, comprising of both austenite and ferrite ($\gamma + \alpha$).

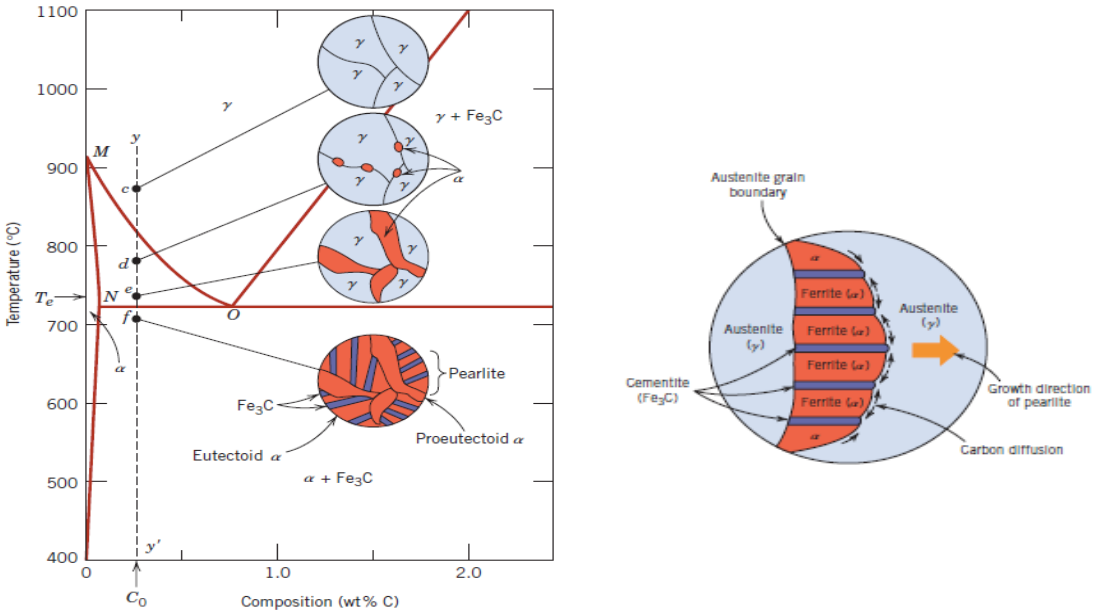

Figure 2.1.2-2: Schematic representation of (a) the microstructures for an iron-carbon hypoeutectoid alloy and, (b) of the formation pearlite from austenite [14].

Subsequent cooling to below the eutectoid phase transformation temperature further alters the microstructure. At lower temperatures, carbon is allowed to diffuse out of the austenite and transforms into an alternating lamellae of ferrite and cementite ($\alpha + Fe_3C$), known as pearlite [14], Figure 2.1.2-2 (b) illustrates the growth of pearlite from austenite. Pearlite, being composed of both ferrite and cementite, has the benefits of both of these two phases. Delta ferrite imparts the added benefits of softness and ductility, whist cementite imparts hardness and brittleness.

The growth of pearlite is dependent on the cooling rate. A continuous cooling transformation (CCT) diagram is used to represent which type of phase changes will occur in a material as it is cooled at different rates, as illustrated in Figure 2.1.2-3. Post welding the weld zone will be exposed to room temperature, which will result in the weld zone cooling very quickly from the high welding temperatures. From the CCT diagram of a low carbon steel, a fast cooling rate will result in the carbon being trapped in solid solution, and the unstable phase martensite is formed.

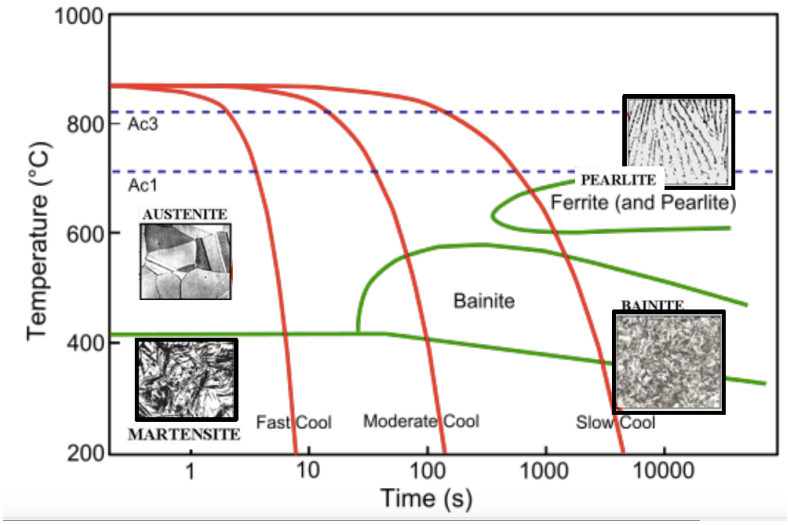

Figure 2.1.2-3: Continuous cooling transformation diagram for a low carbon steel illustrating the different microstructural phases and temperatures bands [18].

In steel pipeline welds, the formation of martensite in the HAZ is avoided as it results in crack-prone zone formations. Therefore, a PWHT is performed to increase the resistance to brittle fracture, and to enhance the material's strength by relaxing residual stresses, which occur due to the resistance of the material during weld solidification [15], [16].

2.1.3 MICROSTRUCTURAL TRANSFORMATION DURING POST WELD HEAT TREATMENT

The primary function of a PWHT is to temper martensite in the weld material and HAZ [17]; this is done in order to reduce hardness, and to increase toughness. The PWHT provides an opportunity for limited microstructural changes, thus achieving a more stable perarlitic or bainitic microstructure [18]. Research conducted by Olabi et al. reported that the use of a PWHT improved the toughness by 15 %, and reduced the residual stresses by approximately 70 % [19]. Uniformly heating of the weldment to a sufficiently high temperature, but below the transformation temperature, and then cooling it provides adequate thermal energy and time for residual stresses to be relieved [17].

Two of the most common types of PWHT are post heating and stress relieving. Post heating is used to minimise the potential for hydrogen induced cracking by diffusing hydrogen from the welded area before it cools [15]. Stress relieving occurs at higher temperatures than post heating, and is used to reduce the stresses that are locked in the microstructure due to solidification; which can be of a magnitude roughly equal to the yield strength of the parent material [15]

The nature of the PWHT is governed by the type of welding used, the chemical composition of the weld filler material, as well as the thickness and restraint of the welded joint [17]. The choice of temperature and duration of the PWHT is critical in determining the welded joint's mechanical performance. For example, if the PWHT temperature is too low, then the weld will inherit inadequate toughness; however, if the PWHT is too high, then the microstructure becomes over tempered and the tensile strength becomes inadequate [20]. In the extreme instance where the PWHT temperature exceeded the AC1 transformation temperature and is cooled abruptly, then the weld material undergo reverse transformation as new martensite laths will form with high strength and low toughness [20]. However, if a slow cooling rate is applied alternative thin layers of ferrite and cementite will form, whilst an even slower cooling rate will result in alternative thick layers of ferrite and cementite.

In general, martensite tempers fairy quickly as the main driving force is the supersaturation of the matrix structure [21]. Prior to PWHT, the martensite structure is a fine dispersion of needle like carbides in a ferritic matrix [21]. During tempering at a suitable temperature, the needle like carbide coarsen, resulting in a decrease in hardness and an increase in toughness[21].

A similar stress relaxation process is seen for a pearlitic microstructure. During PWHT, the pearlitic microstructure changes from alternating ferrite (α) and cementite (Fe_3C) lamellae to spherical cementite particles embedded in a ferrite matrix [14]. The driving force for this transformation is that pearlitic strives to reach a lower energy configuration. The carbon diffuses from the high energy state lamellae into a lower energy spherical configuration.

Despite the benefits of PWHT, it has also been found that if the PWHT temperatures exceeds that of the tempering temperatures of the parent material, then previous quenching and tempering properties will be adversely affected [15]. Another draw back from PWHT is that over tempering of precipitates leads to the nucleation of voids which ultimately propagates into cracks. In a study by Abson et al. it was found that void nucleation and crack formation occurred mostly in the FGHAZ [22].

2.2 MEASURING OF MATERIAL PROPERTY VARIATION ACROSS A WELD

A few methods have been developed to measure the local response of the different weld regions; these include testing of miniature specimens extracted from the different weld regions, instrumented ball indentation testing, testing of bulk material produced by thermal weld experiments and digital image correlation. In order to fully understand the mechanical response of a weld, it is critical to have constitutive data for each of the different weld zones.

2.2.1 CORRELATION BETWEEN MICRO-HARDNESS & STRENGTH OF MATERIALS

One of the most common and easiest methods to evaluate the property variation across a weld is the use of mico-hardness measurements. This method uses a diamond indenter or an instrument ball to dent the surface of the material. Thereafter, the size on the indent is measured and a corresponding hardness value is recorded. This method is relatively straight forward and can be performed semi-non-destructively. However, hardness measurements are confined to the response of the surface layer [8], and is therefore, not a true representation of the bulk material. Furthermore, material properties such as yield strength requires curve fitting of flow stress data, and knowledge of empirically derived hardness to strength conversation equations [23].

Due to the inhomogeneous microstructure present across the weld zone, there will undoubtedly be variation in hardness values across the weld [8]. Vickers micro-hardness measurements were reported to have varied across the various weld zones. In a study on mild steel conducted by Saranath et al, it was reported that the highest hardness value was recorded at the fusion line (FL), whilst the lowest hardness was recorded for the parent material [8]. The peak in hardness at the FL is due to the deformation experienced during the welding process, the phase of the microstructure, as well as the fine crystals or grains formed during the recrystallization process [10], [24].

Figure 2.2.1-1 (a), is a micro-hardness plot across the transverse direction of the weld. It is noticeable that for each of the three different welding currents, there was decrease in micro-hardness from the fusion line towards the parent material. In general, it was found that there was roughly a 50 % decrease in hardness from the fusion line to the parent material [8]. The increase in micro-hardness across the weld is due the enrichment of carbon in harder regions [12], [25].

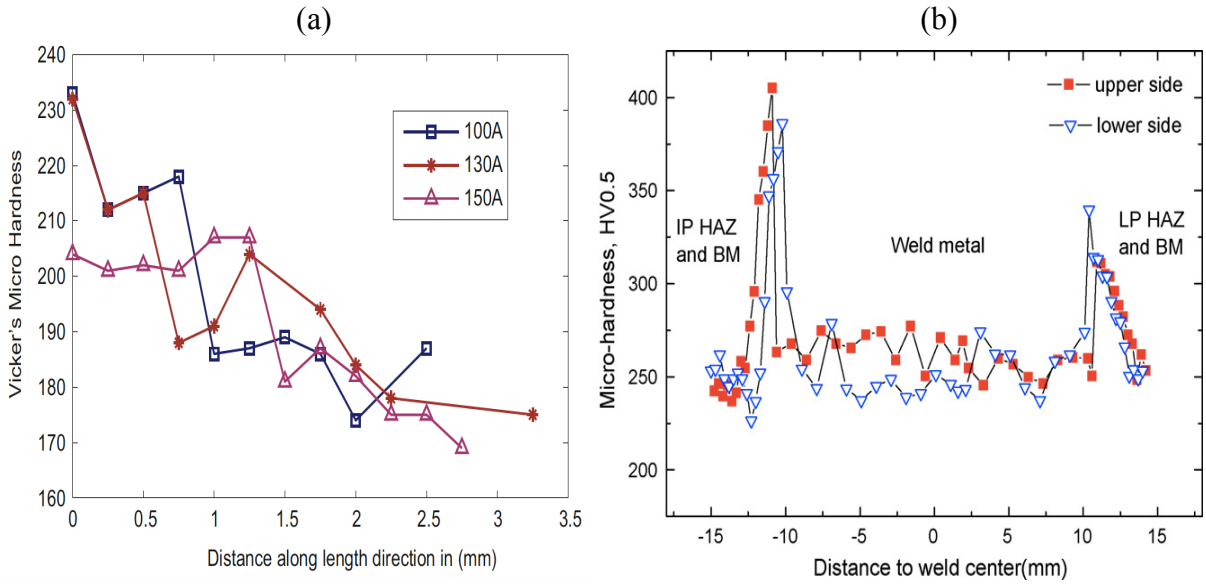

Figure 2.2.1-1: (a) Micro-hardness measurements across weld zones for various welding currents [8] (b) Micro-hardness along the upper and lower sides of a welded joint, moving from the intermediate pressure (IP) HAZ into the low pressure (LP) HAZ [7].

Zhu et al. studied the correlation between hardness and strength of a low carbon rotor steel. In accordance with findings made by Saranath et al, it was also reported that the fusion line had the largest hardness, with a rapid decrease on the weld metal side where delta (δ) ferrite was observed [7]. The peak in hardness was again attributed to brittleness, which is due to the strain hardening process that occurs during plastic deformation [8]. As can be seen by both Figure 2.2.1-1 (a) and (b), hardness values decreased gradually from the fusion line towards the parent material.

Determining material strength estimates from micro-hardness values have been a useful tool that has been developed and refined. It has been found that there is a correlation between yield and ultimate tensile strength of steels based on bulk micro-hardness. This relationship has been formulated and simplified by Cahoon into Equation 2.2.1-1 and Equation 2.2.1-2 [7]. For

ferritic steels at temperatures up to 400 ^{o}C, these two equations have an error of less than 2 % in calculating stress properties from micro-hardness [26].

$$\sigma_{uts} = \frac{H}{2.9}\left(\frac{n}{0.217}\right)^{n} \quad \text{Equation 2.2.1-1}$$

$$\sigma_{ys} = \left(\frac{H}{3}\right)(0.1)^{n} \quad \text{Equation 2.2.1-2}$$

where: σ_{uts} is the ultimate tensile strength (UTS) in MPa, H is the micro-hardness in kg_f/mm^2, n is the strain hardening coefficient and σ_{ys} is the yield strength (YS) in MPa.

Pavlins et al. have found that both UTS and YS have a linear relationship with micro-hardness; for steels with an UTS between 450 and 2350 MPa, and a YS between 325 and 1700 MPa. [26]. This linearity has been observed for a variety of steels over a wide range of micro-hardness values [26].

It must be noted, that both the UTS and YS are not exclusively dependent on the mico-hardness [26]. Material properties such as the strain hardening coefficient also influence the strength of a material. The strain hardening exponent is a measure of the increase in strength of materials due to plastic deformation [24]. From previous studies, it has been found that the strain hardening coefficient, n, is dependent on the microstructure, grain size, temperature and strain rates [24], and will therefore be distributed inhomogenously across the HAZ [7]. Similarly, in a study into the effect of microstructure on strain hardening along a steel joint, Zhu et al. observed that the weld material had a lower strain hardening exponent than the parent material, whereas a strain hardening gradient existed in the HAZ [24]. On the contrary, Chowdhury et al. found that the strain hardening exponent in the WM was nearly twice that of the PM [27], [28]. The variation of strain hardening exponent along the welded joint is strongly dependent on the local microstructural variation [24]. Challenger et al. proposed an empirical equation to determine the strain hardening coefficient in the HAZ, as indicated in Equation 2.2.1-3 [29].

$$n\lambda = \kappa \quad \text{Equation 2.2.1-3}$$

where: λ is the subgrain size in μm and κ is a constant equal to 0.2 μm.

Zhu et al also found that it was acceptable to accurately determine the distribution of the σ_{uts} and σ_{ys} in the HAZ, by replacing the subgrain size with the width of martensite laths instead of the subgrain size [7].

Using Equation 2.2.1-1 to Equation 2.2.1-3, Zhu et al. estimated the strength distribution across the HAZ, as illustrated in Figure 2.2.1-2. From this study, it was found that there was an inverse relationship between σ_{uts} and σ_{ys}, and n; i.e. σ_{uts} and σ_{ys} values decreased as n values increased for the entire weld joint [7]. As is the relationship between microstructure and hardness distribution across the weld, σ_{uts}, σ_{ys} and n are all also influenced by the width and number of lath-like microstructures [7]. Due to martensite having a high hardness and strength, but low ductility, it can be said that as the σ_{uts} and σ_{ys} decreases, n increases with decreasing width of lath-like microstructures in the HAZ [7].

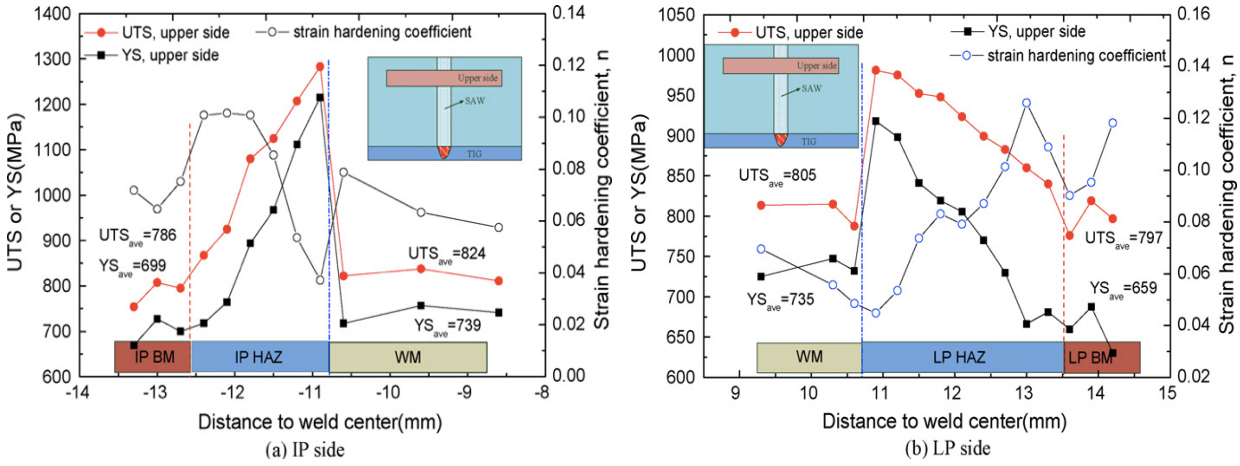

Figure 2.2.1-2: σ_{uts}, σ_s and n distributions in (a) intermediate pressure (IP) rotor (b) and low pressure (LP) rotor of dissimilar welding joint [7].

Zhu et al. also observed that a constant ratio of σ_{ys}: σ_{uts} corresponded to a constant n, and a decreasing σ_{ys}: σ_{uts} corresponded to an increasing n [7]. Thus it was satisfied that Equation 2.2.1-3 can be used to calculate n in the HAZ [7].

2.2.2 CORRELATION BETWEEN HARDNESS & MICROSTRUCTURE

The hardness of a material is directly dependent on its microstructure [7]. Zhu et al. found that there was a direct relationship between the width of martensite laths and micro-hardness. More specifically, as the hardness decreased, the width of the martensite laths decreased [7]; this trend is illustrated in Figure 2.2.2-1. This finding was expected, due to the higher welding temperatures around the fusion line; the width of the laths will decrease from the fusion line towards the base material [7]. The similarity in micro-hardness and microstructure size trend, substantiates that it is suitable to choose martensite lath size as a characteristic microstructure feature [7].

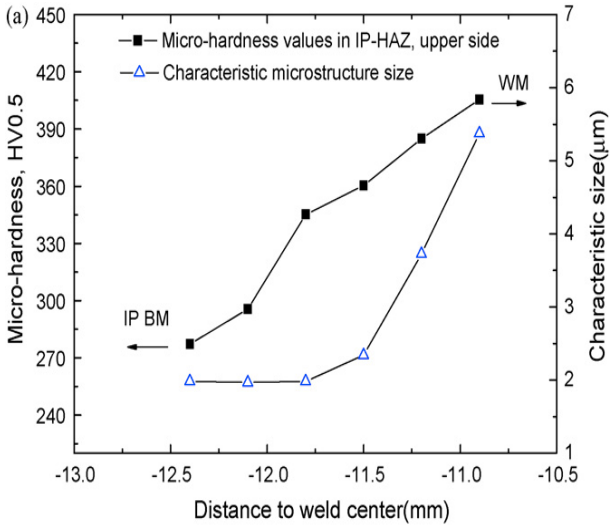

Figure 2.2.2-1: Correlation between micro-hardness and microstructure size in intermediate pressure HAZ [7].

2.2.3 MATERIAL PROPERTY VARIATION ACROSS WELDMENTS MEASURED BY TENSILE TESTING

Tensile testing is a resourceful method used to attain both mechanical and material properties. In order to measure the mechanical and material properties in the different weld zones, LaVan DA suggested the use of micro-tensile samples machined from the different weld zones to measure the material and mechanical property variations across the weld [30].

In a similar study, micro-tensile tests were found to have severe constraints. Difficulties arose due to machining miniature specimens, accurately testing miniature specimens from the localised weld zone, and the spatial resolution and accuracy achieved was limited [8], [23], [24]. In an attempt to rectify these constraints, Zuniga et al. proposed testing of bulk material that was exposed to some sort of mimicked weld thermal experiment[31]. Although this method eliminated the problem of machining small samples, it gave rise to the difficulty of accurately modelling the highly transient thermal gradients experienced across weld zones [8].

Research completed by Saranath et al. employed the standard tensile testing techniques, with the weld zone located in the centre region of the dog bone specimen [8]. It was reported that all welded specimens fractured close to the gripping area, whilst weld free virgin samples fractured in the centre region [8]. This finding indicated that the weld material is significantly stronger than the parent material; which is in accordance with the philosophy of choosing a weld filler material.

Saranath et al. also reported that the fusion line exhibited a considerable change in properties when compared to the other weld zones. The fusion line was found to exhibit the highest yield stress, whilst, the average longitudinal strain of the fusion line was the least strained [8]. This finding is in accordance with literature, where it has been generally accepted that the fusion line of an arc welded butt join experiences high tensile residual stress, which deceases towards the parent material [8].

To illustrate the influence of submerge arc welding on the σ_{uts} and σ_{ys}, Zhu et al. found that for a 25Cr2Ni2MoV steel, the σ_{uts} and σ_{ys} at room temperature prior to welding was 864 and 768 MPa respectively and, decreased to 778 and 726 MPa post welding [24]. A more detailed analysis of the strength distribution across the weld revealed that the CGHAZ (HAZ closest to the FL) had the highest σ_{uts}, and the σ_{ys} decreased moving away from the CGHAZ towards the FGHAZ (HAZ closest to the parent material) [24], as illustrated by the stress-strain profiles in Figure 2.2.3-1 (a). It was also noted that the σ_{uts} and σ_{ys} in the FGHAZ was just slightly higher than those in the parent material [24]. Figure 2.2.3-1 (b) and (c) illustrates the σ_{uts} and σ_{ys} distribution across the welded joint. The average σ_{uts} and σ_{ys} in the WM is much higher than that in the parent material. The σ_{ys} distribution across the welded joint fluctuated more

than the σ_{uts}, indicating that the σ_{ys} is more sensitive to local microstructural changes than the σ_{uts} [24].

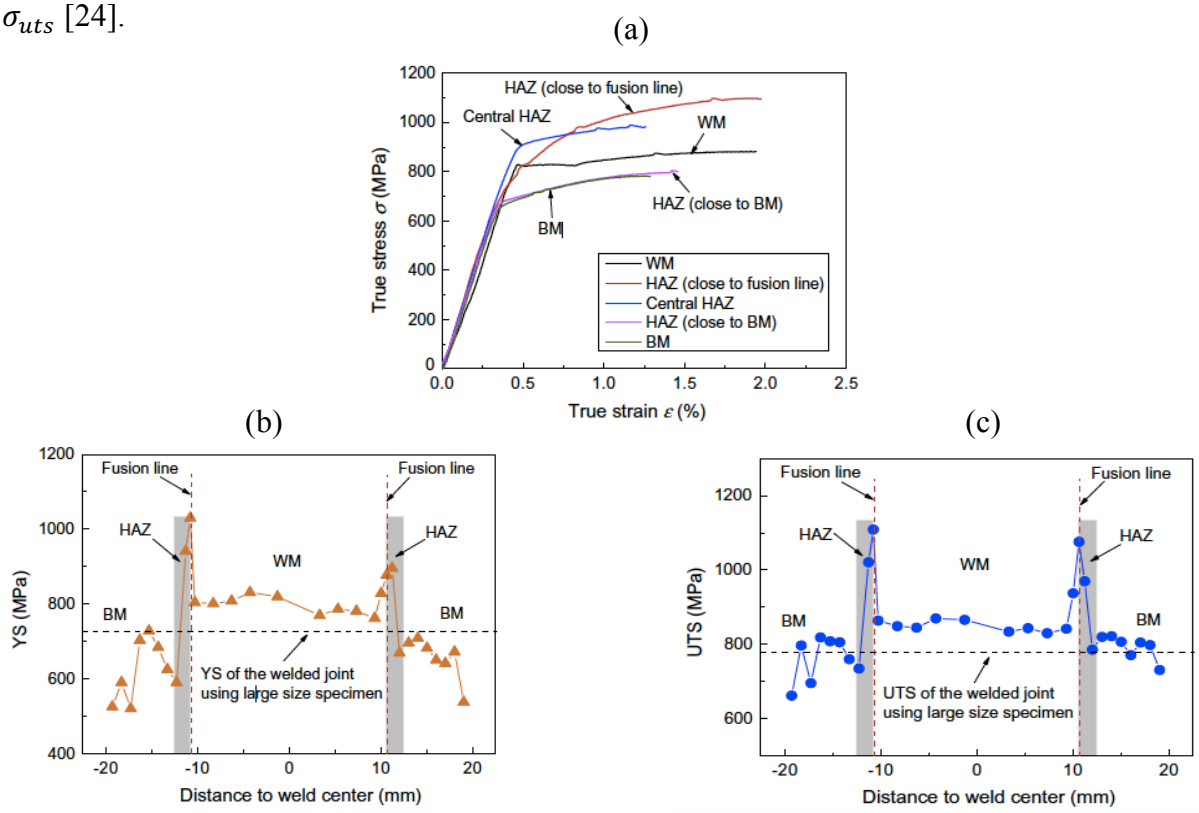

Figure 2.2.3-1: Strength distribution across a weld (a) at room temperature stress-strain curves (b) distribution of σ_{ys} and (c) σ_{uts} along a 25Cr2NiMoV welded joint [24].

By fitting curves of best fit onto stress vs strain plots, material properties such as Young's modulus were extracted. Figure 2.2.3-2 (a), illustrates the Young's modulus variation across the different weld zones. An analysis of Young's modulus values across the entire weld revealed that the fusion zone yielded the lowest Young's modulus; however, the Young's modulus values increased from the fusion line moving towards the parent material [8]. The difference in Young's modulus values between the virgin and welded specimens were believed to have been attributed to the size and cooling rate of the fusion line and the HAZ [8]. The cooling of the molten metal around the fusion line would have resulted in the increase of ductility. The improved ductility caused more deformations during elastic deformation which resulted in a lower Young's modulus [8].

Poisson's ratio, which is the ratio of transverse strain to longitudinal strain, yielded the highest value in the CGHAZ, as illustrated by Figure 2.2.3-2 (b). Overall, there was a mild variation

in Poisson's ratio; however, it was conclusive that the welding process increased Poisson's ratio as the virgin specimen reported the lowest Poisson's ratio value [8].

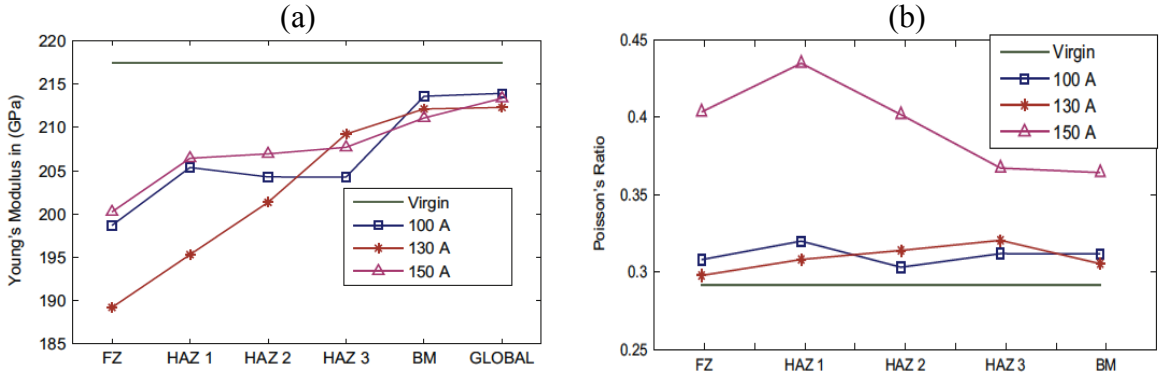

Figure 2.2.3-2: Variation of (a) Young's modulus and (b) Poisson's ratio across weld zones [8].

These finding, were further supported by work done be Ambriz et al. and Song et al, where a similar Young's modulus and Poisson's ratio was reported [32]. Figure 2.2.3-3 illustrates the change in material constants from the base material to weld material for a Titanium (TA15) alloy specimen. Song et al found that Young's modulus values decreased by approximately 10 GPa from the parent material towards the FL, whilst, Poisson's ratio increased by approximately 0.025 from the parent material towards the fusion line [33].

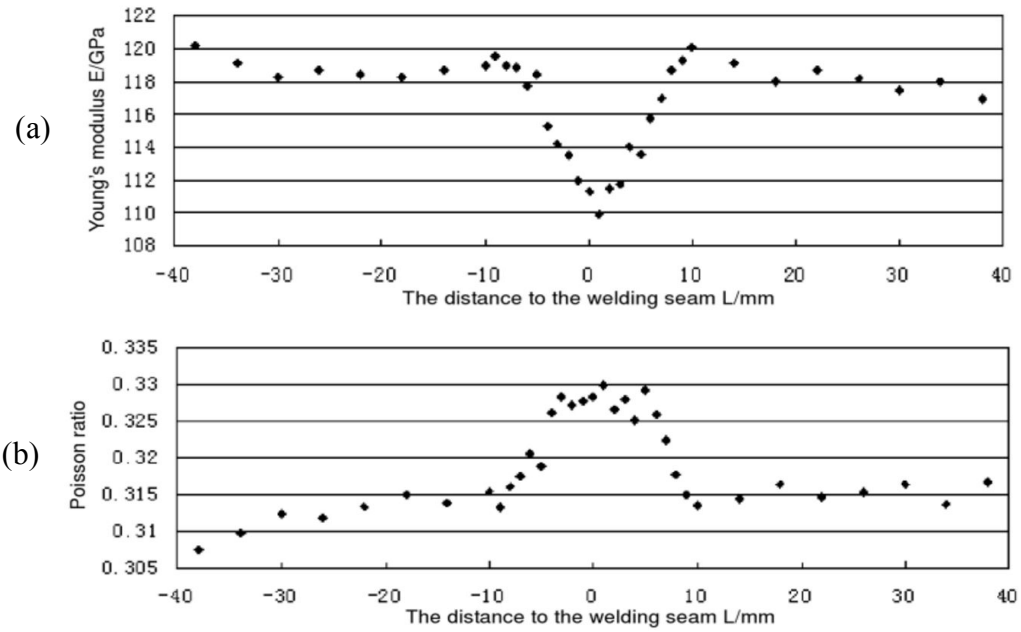

Figure 2.2.3-3: (a) Young's modulus and (b) Poisson's ratio distribution across the weld for a Titanium alloy specimen [33].

2.2.4 STRENGTH VARIATION ACROSS WELDMENTS MEASURED BY DIGITAL IMAGE CORRELATION

Digital image correlation (DIC) is a non-contact optical technique, full field displacement measurement technique with good spatial resolution used to determine the local strain response of weld zones. The backbone of DIC is a correlation algorithm that tracks and records the whole field deformation changes of an image. DIC operates on comparing the deformation in pixels between an undeformed specimen (reference image) with a deformed specimen. By using correlation functions displacements are computed, from which the gradients of the displacements fields are smoothed to produce strain fields. To facilitate quick processes, pixels are grouped together into clusters called facet size. Image correlation is based on obtaining maximum correlation between facets using even spaced grid points called grid spacing to track deformations.

There is no uncertainty that the material tested is representative of the material in the weld. However, the limitations posed by this method are that if the material property gradient across the weld is steep, the accuracy in differentiating between the different weld zones is low, and if there is a breakdown of the high contrast speckle pattern applied to the specimen, the method is unusable [23].

In a study that employed DIC techniques to evaluate the change in material properties across a weld, Saranath et al. reported that there was a distinct change in stiffness in the different weld zones for various welding currents, as illustrated in Figure 2.2.4-1.

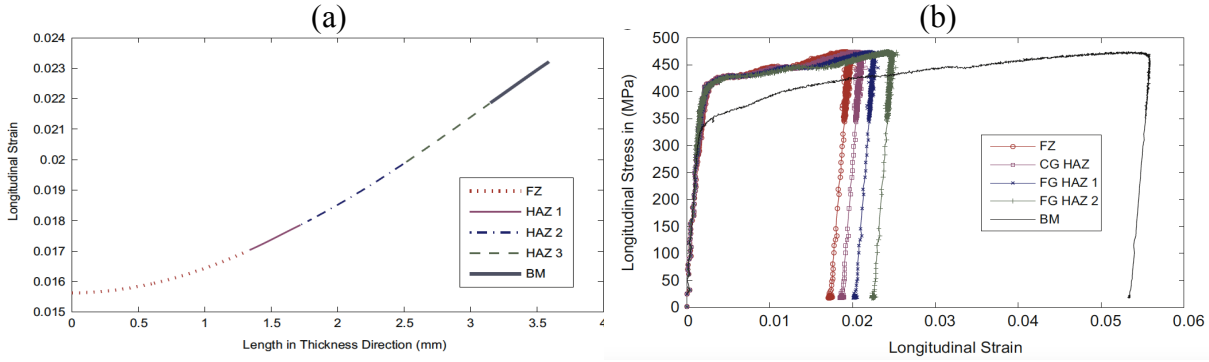

Figure 2.2.4-1: (a) Strain distribution illustrating the division in weld zones (b) Stress strain profile obtained from DIC data for a sample welded with a current of 130 A [8].

Figure 2.2.4-1 (a) illustrates that there is a continuous increase in strain from the FL (detonated as FZ in Figure 2.2.4-1) towards the parent material (denoted as BM in Figure 2.2.4-1). This finding agreed to what was expected, as the heat affected zone (HAZ 3), which corresponds to the fine grained heat affected zone (FGHAZ) is the weakest zone as it was found to have strained the most.

This finding was further validated by comparing stress strain plots for the different weld zones using strain data obtained from DIC, as illustrated in Figure 2.2.4-1 (b). The stress strain profile illustrates that ductility increases from the FL towards the FGHAZ. From both Figure 2.2.4-1 (a) and Figure 2.2.4-1 (b), it was observed that the parent material strained the most when compared to the heat affected zones. This finding is in agreement with work published by Yilbas et al., where it was found that this variation in strain was attributed to two main reasons. Firstly, the grain size and cooling rate of the FL and HAZ in both the elastic and plastic regions [34]. More specifically, the cooling of molten metal in the FL at atmospheric pressure and temperature resulted in the increase in ductility. In the elastic region, this increase in ductility resulted in more deformation and a lower Young's modulus. Whilst, in the plastic region, strain hardening was dominant, and a reduction in ductility was noticed. The second reason for this variation, is due to the inhomogeneous residual stresses induced during welding and inhomogeneous formation of the FL and HAZ [34].

Tso-Liang Teng et al. also found that the FL of an arc welded butt joint experienced high tensile residual stresses, which decreases gradually from the FL towards the parent material [35], [36]. During tensile tests, the applied stress adds to the residual stresses of the FL and HAZ which resulted in a lower Young's modulus [37].

It has also been found that the creep strength of high temperature and pressure components from power plants, is largely governed by the integrity of weldments [38]. In a study to quantify the creep strength of stainless steel power plant weldments, Sakanashi et al. used a three-zone furnace with a porthole side through which images for DIC were captured. Using commercial DIC software, the captured images were post processed and local strain data for the different weld zones were extracted.

Sakanashi et al. conducted two types of strength tests; a tensile test conducted at a strain rate of 0.1 mm/min after a heat treatment of 545 ^{o}C, and a constant load 315 MPa creep test at 545

^{o}C. Figure 2.2.4-2 illustrates the local strain variation along the gauge length for each of these tests.

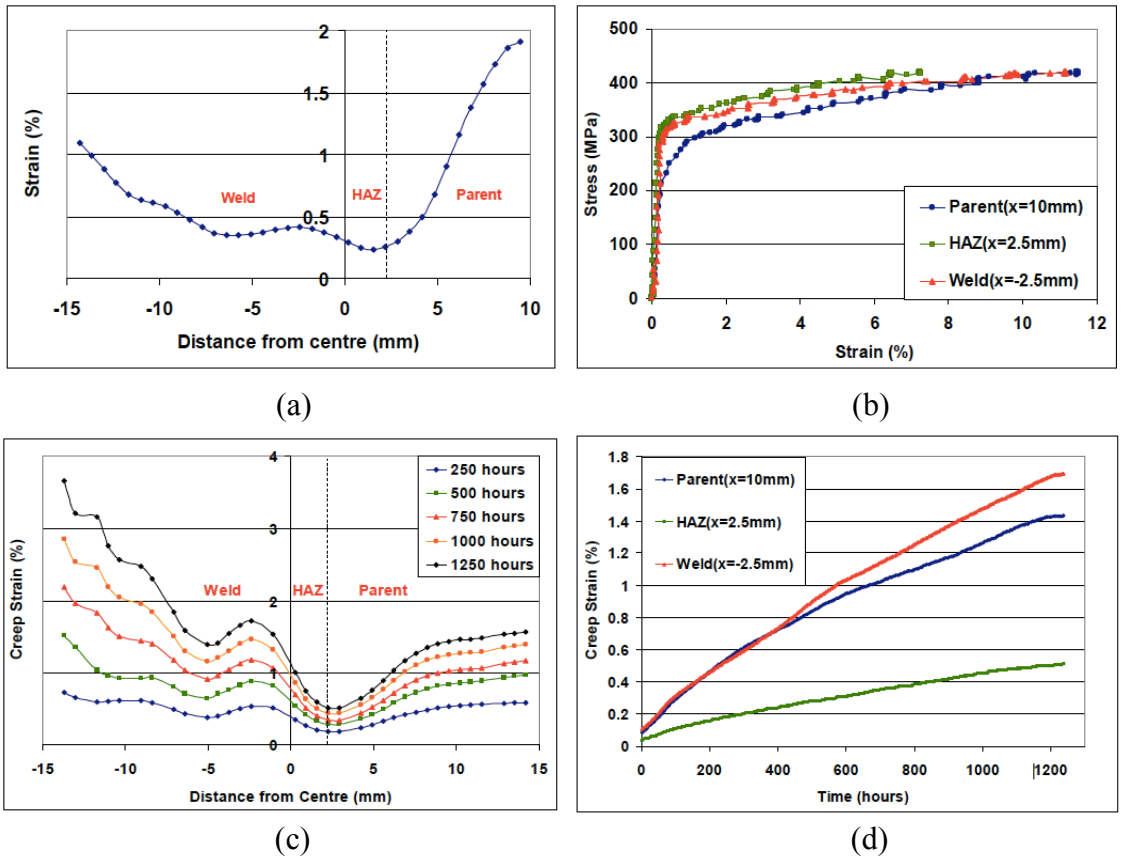

Figure 2.2.4-2: (a) strain distribution across a tensile test weldment (b) local weld tensile test stress-strain curves (c) creep strain variation across a creep weldment specimen (d) local weld creep curves [38].

From the tensile tests, it was found that fracture occurred in the weld material. Figure 2.2.4-2 (a) illustrates that the lowest strain was observed in the HAZ, when compared to the weld and parent material. Furthermore, the strain fluctuation in the HAZ was explained to be due to the weld passes [38]. In addition, a variation in yield stress was also observed, as illustrated by the stress-strain curves in Figure 2.2.4-2 (b). The parent material showed the lowest recorded yield stress, approximately 80 MPa smaller than that of the weld material, whilst the HAZ proved to be the most ductile.

Figure 2.2.4-2 (c) illustrates the creep strain evolution at different times for the creep test along the gauge length. Similar to the tensile test, the HAZ also exhibited the lowest creep strain, when compared to the other regions. The trend of the lowest strain occurring in the HAZ was

further supported by the local creep deformation curves, where the HAZ was seen to be most creep resistant [38], as illustrated in Figure 2.2.4-2 (d).

On the contrary, the weld material was observed to have the largest creep strain, rather than the parent material. To some extent, this finding was due to the yield stress of the parent material being less than the applied stress of 315 MPa, which is approximately the yield stress of the HAZ and weld material [38]. In other words, upon loading the HAZ and weld material would have remained elastic, whilst the parent material would have plastically creep strained; this would have resulted in it work hardening. As the creep test progressed, the material properties and ductility of the parent material would have changed due to it work hardening, and as a result it would have creep strained to a less extent [38].

Furthermore, the variation of creep strain in the weld material was explained to be largest in the middle region of the weld bead, when compared to the weld bead boundary (FL), as well as due to the local thermo-mechanical welding process [38].

In a similar study done on aluminium tensile specimens, Reynolds et al. discovered that the weld is the source of inhomogeneities in material properties. As a result, the majority of the plastic deformation is concentrated in the weld region, where initially strain hardened grains have recrystallized or recovered [23]. Initially strain localises in the soft weld fusion line, and as the fusion line strain hardens, yielding occurs at progressively greater distances from the fusion line [23].

2.3 HIGH TEMPERATURE DEFORMATION MEASUREMENTS USING DIGITAL IMAGE CORRELATION

2.3.1 GLEEBLE THERMO-MECHANICAL SIMULATOR

There are various methods used to heat a specimen during experimental testing, such as: furnaces, laser and infrared radiation, and resistance (ohmic) heating.

The Gleeble 3800, is a thermo-mechanical simulator, which is capable of weld HAZ experiments, heat treatments and multi-hit hot deformations under combined conditions of transient heating and mechanical loading [39]. Using direct resistance heating via a 50 Hz AC current, the Gleeble is able to heat specimens at rates up to 10 000 ^{o}C per second, whilst exerting 200 kN of static force in compression, or, 100 kN in tension [39].

To heat a specimen, energy is supplied in the form of current from the water cooled wedge grips and propagates from either end of the specimen towards the specimen's centre. As in any thermodynamic system, there are always sources of heat loss that need to be accounted for. Heat loss occurs by three main mechanisms, namely; conduction, convection and radiation. Losses due to conduction stem from heat transferred to the water-cooled jaws. The thermal diffusivity of the material as well as the thermal gradient across the specimen are two of the main contributors to heat loss due to conduction [40]. Heat loss due to convection occurs due to heat dissipation to the surrounding atmosphere. Finally, heat loss due to radiation emitted by the specimen arises from electromagnetic waves in the infrared region. Radiation emitted by the specimen is as a consequence of the thermal agitation of the specimen's composing molecules [40] and only becomes significant at high temperatures.

By ignoring heat losses due to convection and radiation, the following conservation of energy relationship is used to describe the one dimensional thermal distribution across a Gleeble tensile specimen [40]:

$$\frac{\partial T}{\partial t} = \frac{\mathrm{K}}{\rho C_p}\frac{\partial^2 T}{\partial x^2} + \frac{I^2}{\rho C_p w^2 \sigma}$$ Equation 2.3.1-1

where, K is the thermal conductivity in W/m.K, T is the temperature in K, ρ is the density in kg/m^3, C_p is the heat capacity in J/K, t is time in s, W is the cross-section area in m^2, σ is the electrical conductivity in S/m, and I is current in A.

Thus, by Equation 2.3.1-1, the temperature distribution across the specimen will be a parabolic one. This is a major challenge for material property measurements, as the specimen will deform the most at its centre where it is the hottest and, the deformation will decrease with a reduction in temperature due to the increase in flow stress [41].

2.3.2 TENSILE SPECIMEN GEOMETRY

To improve the existing temperature gradient, Norris et al. designed and tested a new specimen geometry that has a temperature profile close to the optimum theoretical profile, indicated in Figure 2.3.2-1. In order to attain accurate material property measurements, the length of the hot zone at the centre of the specimen needs to be optimised. By increasing the length of the hot zone, all stress and strain will concentrate at this region, allowing for accurate material property measurements [41].

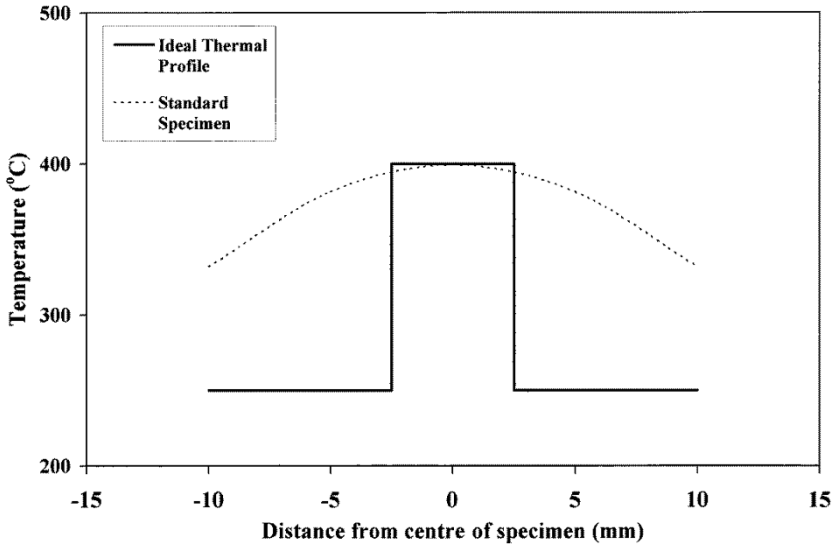

Figure 2.3.2-1: An ideal temperature profile for an optimised temperature profile vs. a standard temperature profile [41].

By comparing the results from an actual Gleeble experiment, with a finite-difference simulation software, Norris et al. were able to optimise a conventional Gleeble tensile specimen by systematically changing geometrical parameters.

To begin, Norris et al investigated the temperature profile of three different specimen shapes: a 10 millimetre diameter round, a 10 x 10 millimetre square, and a 10 x 2 millimetre flat, all with a standard gauge length of 120 millimetres. There was no difference between the temperature profiles of the round and square specimens; however, due to its high surface area to volume ratio, the flat specimen had a temperature profile closest to the ideal profile [41]. By introducing a reduced cross-section gauge length specimen, as illustrated in Figure 2.3.2-2, it was further found that the flat specimen showed the greatest tendency towards the ideal profile [41], thus the flat specimen was used for subsequent optimization experiments.

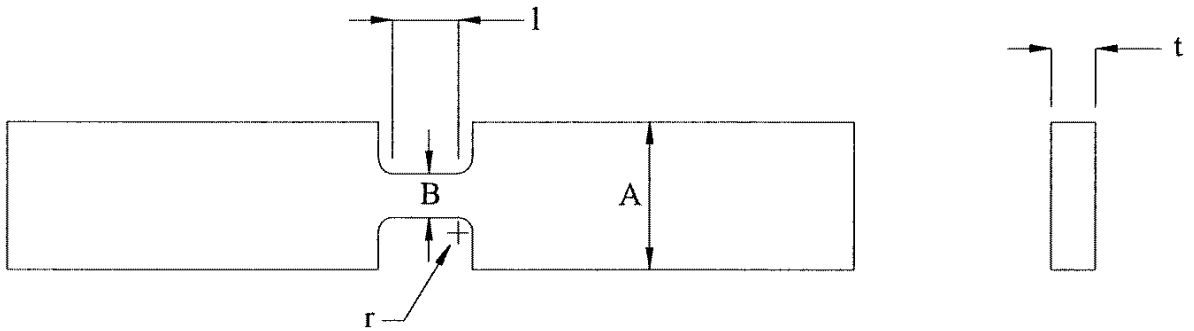

Figure 2.3.2-2: Schematic diagram of a Gleeble tensile specimen, defining the dimensional parameters that are optimised [41].

Other modifications to the specimen geometry included changing the: gauge length, specimen thickness, and gauge length radii. The following findings were found [41]:

1. Changes to the gauge length: A series of experiments were conducted by progressively reducing the gauge length (l) from 10 millimetres to 3 millimetres, in increments of 1 millimetre. A gauge length of 10 millimetres produced the largest hot zone; however, the temperate profile within the hot zone was non-uniform, and the temperature reduction rate outside of the hot zone was the steepest.
2. Changes to the specimen thickness: The thickness (t) was varied from 7 millimetres to 4 millimetres, and there was no effect of a change in thickness to the thermal profile.
3. Changes to the gauge length radii: The radii (r) was varied from 3 millimetres to 1 millimetre in increments of 1 millimetre, and it was found that as the radii decreased, the thermal profile resembled closer to the theoretical profile.

Following the geometrical optimisation strategies mentioned above, Norris et al. concluded that a flat (rectangular) specimen, with a reduced central cross-section along its gauge length, produced a thermal profile closest to the ideal thermal profile, illustrated in Figure 2.3.2-2.

2.3.3 DIGITAL IMAGE CORRELATION (DIC)

The principal of DIC is to measure strain by comparing digital photographs of a component at different loading states [42] as illustrated by Figure 2.3.3-1. In general, the images surface is covered with a random speckle pattern [43]. This pattern provides the random grey scale distribution that allows for displacement data to be measure [44].

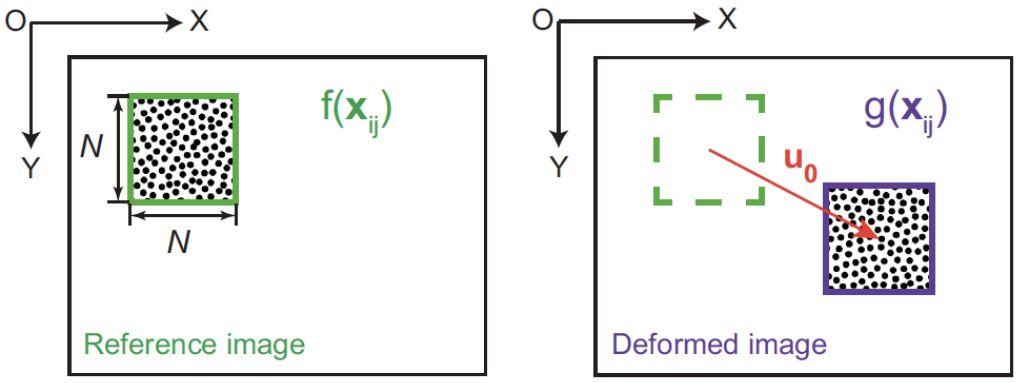

Figure 2.3.3-1: Illustration of facet tracking between reference image and deformed image [42].

The deformation from the reference state to the deformed state is measured by individually tracking a group of speckles (pixels) termed facet size (N x N). Assuming only rigid body translation, the displacement U_o is measured by:

$$U = \arg min \sum_{i=1}^{N}\sum_{j=1}^{N}\left[f\left(X_{ij} - g(X_{ij} + U)\right)\right]^2 \qquad \text{Equation 2.3.3-1}$$

where U is the rigid body translation, N is the facet size, $f(x_{ij})$ are the coordinates of the reference image and $g(x_{ij})$ are the coordinates of the deformed image.

DIC techniques are versatile, in that they can be applied to a variety of materials in different experimental fields, such as fracture mechanics, material characterisation and micro mechanics

[8]. DIC techniques can be applied both in two and three dimensions. The use of one camera to measure strain in two axes has the advantage of providing qualitative assessment of material behaviour; however, it is restricted to deformation measurements specifically from in-plane fields [45]. Out of plane deformation is achievable by using a two camera or stereo DIC system. The advantages of this type of system is that it allows for material properties such as Poisson's ratio to be determined and it caters for curved specimen geometries. In addition, it also acts as a tool to assess the quality of the testing rig by measuring deformation due to misalignments and bending in the grips [45].

Sources of error in DIC strain readings include: under-matched shape functions [46], image noise [47], lens distortion, out of plane displacements [48], DIC parameter selection, and speckle pattern distribution [6]. Shape functions are used to describe the movement of a facet. For example, a zero order shape function is applied to facets that experience strains due to purely rigid translations, whilst a first order shape function is applied to facets that have strains due to both translation and rotational deformations [46]. The incorrect selection of shape function for a specific displacement field can attribute to strain errors in the order of 10^{-4} strain [46]. The inaccuracies due to image noise have been found to be minimised by the application of Gaussian and Savitzky-Golay low pass filters [47]. Depending on the type of camera lenses used, out of plane displacement errors can be reduced by ensuring that the correct focal length between the camera and specimen is maintained; an approximate distance of 1.5 meters is recommended [48]. Furthermore, out of plane displacements can also be minimised by ensuring perpendicularity between the camera and specimen [48]. Facet size and grid spacing selection plays an intricate role in ensuring accurate results.

From the 1980's, extensive research has been done to improve DIC techniques such that they now can be successfully used to accurately characterise inhomogeneous material and mechanical properties across weld zones [8]. In the past, extensometers and strain gauges were used to record strain deformation. The major disadvantage of these methods is that they average strain across the specimen, whereas DIC is capable of mapping localised strain that extends into the plastic region. Wang et al. investigated the capabilities of these two techniques and substituted extensometers with DIC due to its superior resolution [49].

Two of the primary challenges faced when incorporating DIC with tensile tests at elevated temperatures, were the thermal radiation emanating from the specimen [50], and the quality of the speckle pattern.

At elevated temperatures, the light radiated by the specimen falls within the sensitive wavelength range of the camera detectors. Lyons et al. conducted tensile tests at 750 ^{o}C on nickel super alloys, and found that the surface glow radiated by the specimen was brighter than the white light provided for illumination [50].

Chen et al. found that they were able to overcome this problem by using blue band pass filters with blue monochromatic light [51]. They found that the blue filter was able to reject long wavelengths, whilst, only transmitting shorter blue waves. By combining both filters with lighting, testing at elevated temperatures (up to 1 100 ^{o}C) was possible without saturation occurring [51]. In order to attain an estimation as to what temperature level the saturation becomes problematic, it was found that successful tensile tests on stainless steel samples were conducted at temperatures of 545 and 550 ^{o}C without the use any filters [38], [52]. Pan et al. suggested that in the absence of filters or specialised lighting, the maximum temperature that successful DIC analysis could occur was in the range of 600 ^{o}C [53].

There are two DIC parameters that are critical to ensuring accurate DIC measurements, namely speckle pattern quality and facet size.

Speckle pattern

In order for the DIC system to measure deformation, a contrast enhanced speckle pattern is required to track subsets of pixels during deformation [51]. By assessing the mean intensity gradient of the speckle pattern Pan et al. reported that the quality of the speckle pattern correlated strongly with the DIC displacement measurement error [54]. In a study conducted by van Rooyen et al., the mean intensity factor of a four different speckle patterns was assessed as illustrated by .It was reported that a white speckles on a black background attained a higher gradient values which indicated a higher quality pattern [43]. In addition, the variation in the mean intensity gradient between patterns was attributed to the difference in consistency between the two paint types. One of the draw backs of the mean intensity gradient assessment

is that it does not consider the influences of pattern quality variation and therefore is biased towards areas with unusual intensity gradients [43].

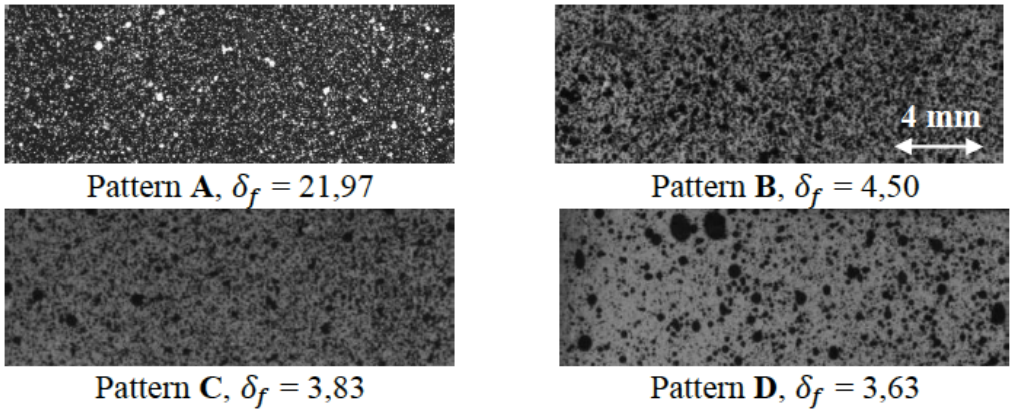

Figure 2.3.3-2: Four different speckle patterns with mean intensity gradient values [43].

Due to the bias of the mean intensity gradient assessment, van Rooyen et al. employed a morphological approach to assess the quality of the speckle pattern. In this approach, the impact of the distribution of the size of speckles in the patterns is assessed [43]. An even distribution of smaller and larger speckles is recommended as smaller speckles permit a higher variation of intensity whilst a larger speckles allow for more unique shape permutations which aid the correlation process [43]. By assessing the speckle pattern quality using the morphology approach van Rooyen et al. suggested a minimum speckle area of 9 pixels^2 in order to avoid intensity interpolation errors and as a result, found that 70 % of black speckles on a white background were larger than the minimum suggested area whilst only 45 % of white speckles on a black background met this criterion. In addition, Crammond et al. reported that the intensity variation between speckles on a white background was higher which subsequently assisted the correlation process and displacement accuracy [55].

At elevated temperatures, the speckle pattern is expected to retain its colour and contrast, and needs to remain bonded to the specimen without burning off. Pan et al. observed that generic paints used to generate a speckle pattern deteriorated at temperatures higher than 250 ^{o}C [56]. Thus, in order to extend the testing temperature above 250 ^{o}C, a more durable speckle pattern was needed. Chen et al. used both a white and black heat resistant ceramic paint to create a speckle pattern, and were able to extend the testing temperature to 1 100 ^{o}C [51]. To ensure maximum bonding of the speckle pattern paint, Swaminathan et al. abraded the specimen surface with a fine grit sandpaper before applying the speckle pattern [57]. By doing this they were able to increase their testing strain rates without the paint debonding [57].

Facet size selection

Facet size selection is the other parameter that is critical in ensuring accurate DIC measurements as it defines the size of the group of pixels that will be used by the correlation algorithm to track the displacements. Wittevrongel et al. reported that the facet size selection should be a trade-off between background noise and spatial resolution [58]. Due to inherent experimental variability deformation due to background influences result in artificial displacement measurements, it is critical to counter the influences of background noise with spatial resolution which refers to the distance/overlap in facets in order to ensure accurate displacement data. The advantage of a larger facet size is that it will contain a more unique and distinctive speckle pattern in comparison to other facet, which will result in low background noise. On the other hand, the smaller facet sizes allow for more accurate displacement measurements with improved spatial resolutions [59].

van Rooyen et al. applied a quantified assessment of displacement error in order to determine facet size. By applying an artificial sinusoidal displacement in the axial direction to a reface image with a good quality speckle pattern, the facet size was determined based on its ability to detect high gradient deformations by applying square facets sizes ranging from 21 pixels to 121 pixels with a constant grid spacing of 50 % [43]. By quantifying the root mean square (RMS) error, it was also reported that smaller facet seizes resulted in lower displacements, whilst larger facet sizes (121 pixels) approached the RMS error which indicated the upper limit of displacement uncertainty [43]. With a measured background noise of 0.37 μm, Van Rooyen et al. recommended a facet size of 61 pixels with a grid spacing of 30 pixels as this provided a good trade-off between displacement uncertainty and spatial resolution.

3 DEVELOPMENT OF EXPERIMENTAL STRATEGY

This chapter discusses the challenges encountered with the experimental approach used to achieve the objectives of this study, and their proposed solutions. An experimental strategy was developed to evaluate strain localisation across a weld zone. This incorporated the design of a tensile specimen, as well as a technique to measure localised deformation as reflected by surface deformation at elevated temperatures.

3.1 EXPERIMENTAL OVERVIEW

Material from a power station's main steam pipe line containing two different weldments (one weldment was exposed to more elevated temperature and load compared to the other) were used for experimental investigation. In addition, dummy trial experiments were performed on readily available EN8 material.

As a means to induce mechanical loading at a constant temperature, a Gleeble 3800 thermo-mechanical simulator with a tensile module was used. The Gleeble is capable of physical simulation in either load or displacement control, and is able to perform thermo-mechanical testing at elevated temperatures. To ensure accurate execution and reliability, specimens were tested under vacuum to minimize the effects of oxidation, and thermocouples were spot welded onto the specimen to provide signal feedback of the temperature profile across the specimen's gauge length. In addition, an infrared radiometric camera was used to gain a full field thermal profile of the tensile specimen.

Measurement of strain localisation during thermo-mechanical testing was performed with two dimensional digital image correlation (DIC). DIC is a noncontact photomechanical technique, capable of capturing highly localised strain fields. The noncontact nature of DIC allowed for the tensile specimen to be exposed to elevated temperatures whilst under load. The DIC system comprised of an in plane area scan camera, lens filters, LED powered lighting, image capturing software, and post processing imaging software. Figure 3.1-1 illustrates an overview of the experimental setup.

Subsidiary experimental investigations included Vickers hardness and light microscopy. Vickers hardness tests and light microscopy analysis were conducted to locate and verify the location of the weld heat affected zones (HAZ).

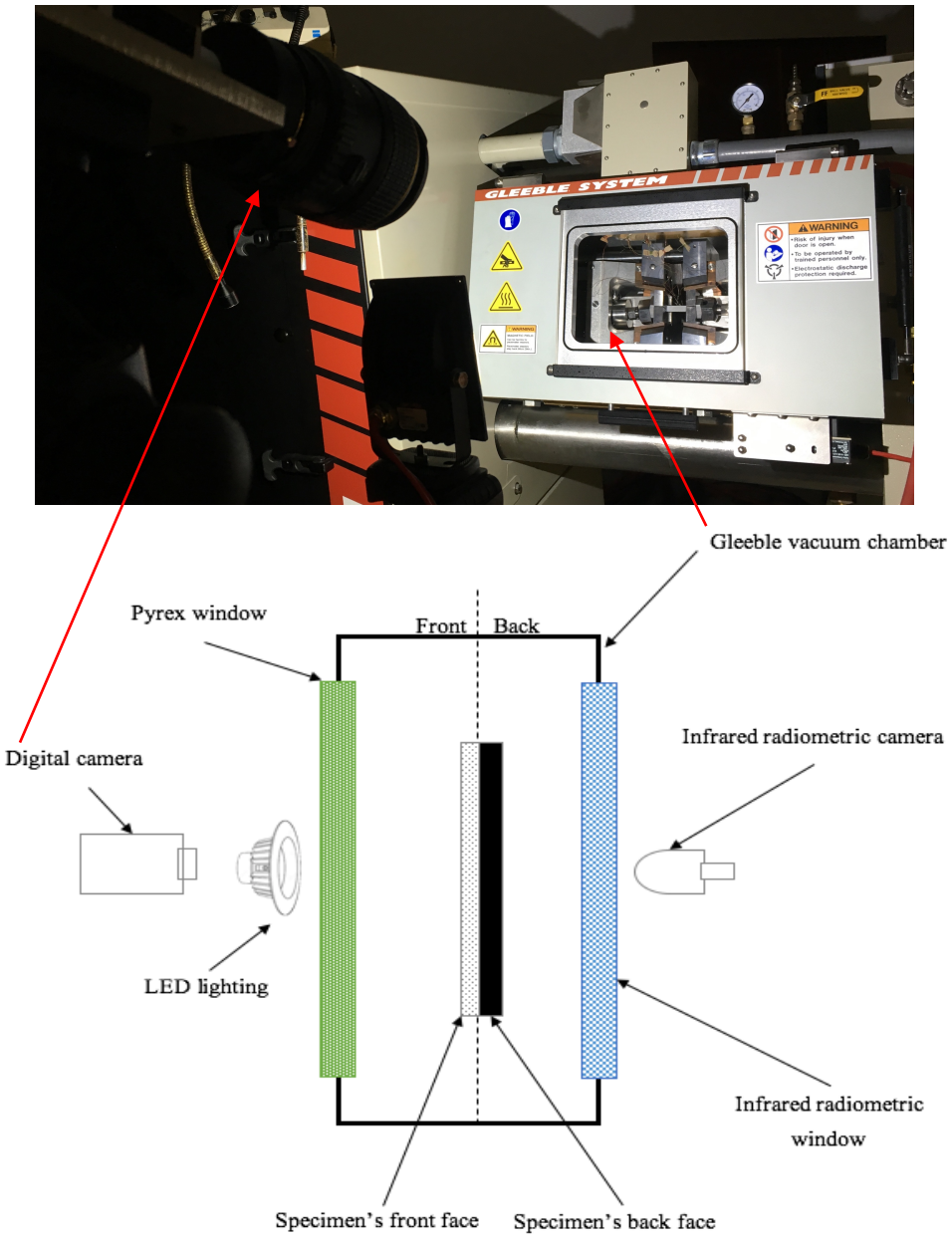

Figure 3.1-1: Illustration of the experimental equipment and setup.

3.2 SPECIMEN DESIGN AND IDENTIFICATION OF THE WELD ZONES

Specimen design involved adapting the conventional tensile specimen geometry to improve the irregular thermal loading across the specimen's gauge length. The location of the weld zones was revealed by conducting both light microscopy as well as Vickers hardness analysis. Identification of the weld zone was critical for spatial calibration.

3.2.1 SPECIMEN DESIGN AND EXTRACTION

The Gleeble uses direct resistance heating to heat the specimen. Energy in the form of electric current passes from either end of the specimen and produces a hot zone towards the specimen's centre. The large thermal gradient present at the centre of the specimen is undesirable for mechanical testing of strain localisation, as each section of the material when loaded will deform by different amounts due the variation of the temperature dependent flow properties [41]. In order to reduce the effects of the irregular thermal loading, the length of the hot zone was optimised by following the geometry optimisation approach recommended by Norris et al [41].

The regular rectangular Gleeble tensile specimen was modified by reducing the cross-section along the centre of the gauge length. Figure 3.2.1-1 illustrates the modifications made to the standard Gleeble specimen.

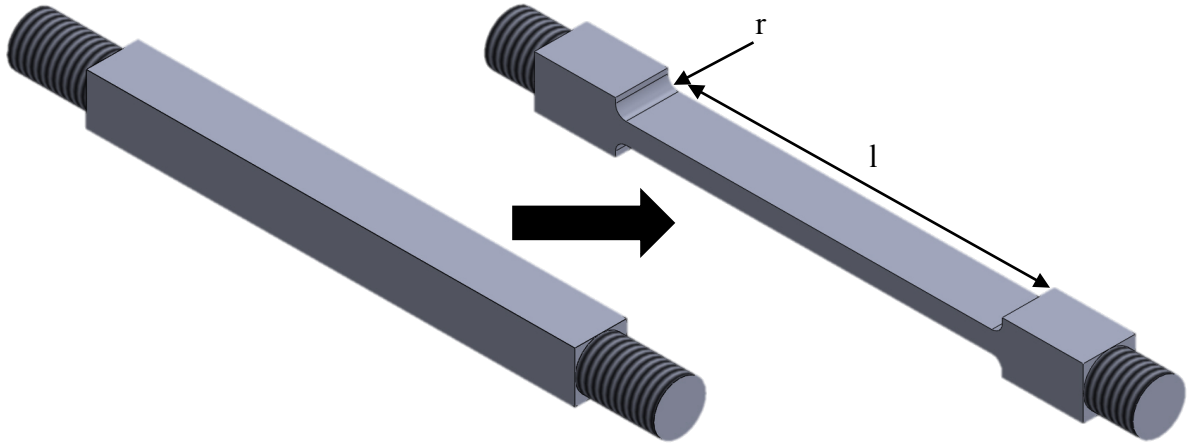

Figure 3.2.1-1: Schematic illustrating the modifications to the standard Gleeble tensile specimen.

In order to establish the largest possible hot zone, the following geometrical parameters were optimised:

- The gauge length (l) was made as long as possible.
- The gauge length radii (r) was made as small as possible.

Tensile test specimens from both weld zones were machined with its axis in the longitudinal direction of the steam penetration, as illustrated in Figure 3.2.1-2. In order to ensure accurate strain localisation measurements across the weld zone, tensile test specimens were designed such that the fusion lines were roughly at the centre of the specimen's gauge length.

One of the major constraints encountered in the design of the tensile specimen was the position of the weld zones relative to the edge of the steam pipe where it was cut off. After grinding, polishing, and etching two segments of the steam pipe, it was determined that the fusion lines for both weldments under investigation were approximately 40 millimetres away from the edge of the steam pipe, as illustrated in Figure 3.2.1-2.

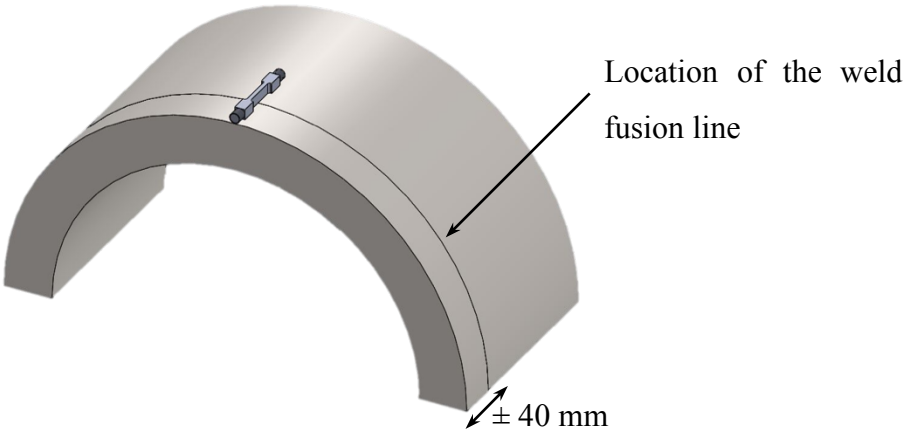

Figure 3.2.1-2: Schematic illustration of the tensile specimen location relative to the orientation on the steam penetration.

In order to ensure that the fusion line was positioned at the centre of the specimen's gauge length, tensile specimens were designed to have an overall length of approximately 80 millimetres. To accommodate for any inconsistency during welding and/or specimen machining process, the overall length (l) of the tensile specimen was adjusted to 84 millimetres long, as illustrated in Figure 3.2.1-3. In addition, an exposed gauge length of at least 30

millimetres was maintained in order to allow for sufficient area for calibration of the DIC system.

A specimen length of approximately 84 millimetres was much shorter than a conventional Gleeble tensile specimen, which is stipulated to be 124 millimetres long as illustrated in Figure 3.2.1-3. A comprehensive drawing of the specimen geometries can be found in Appendix 8.1.

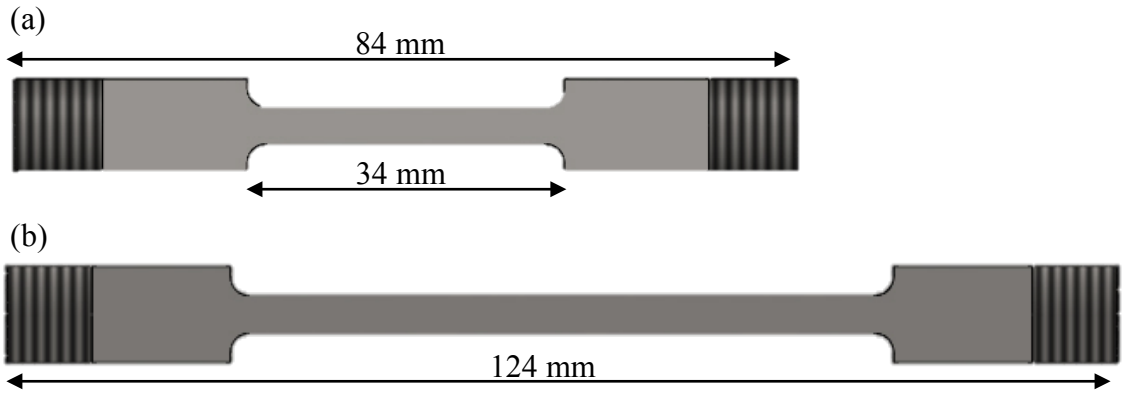

Figure 3.2.1-3: Schematic representation of the (a) modified Gleeble specimen with respect to (b) the standard tensile specimen.

3.2.2 LIGHT MICROSCOPY ANALYSIS

Metallography is the analysis of a metal's microstructure by light optical and/or electron microscopes. Useful information pertaining to the material's mechanical properties as well thermal gradient induced during welding were gained from microstructural analysis. Microstructural analysis preparation involved three key steps, namely grinding, polishing and etching.

Samples for microstructural analysis were machined from both weldments, with approximate dimensions of 28 mm x 10 mm x 10 mm. To facilitate easier handling during grinding and polishing, samples were hot mounted in an acrylic ClaroFast SEM acrylic resin. The grinding process involved the use of three different grades of Struers waterproof silicon carbide paper, namely the 500, 800 and 1 200 grit. Samples were carefully inspected under a light microscope at regular intervals during the grinding process. The inspection process consisted of rinsing the sample with ethanol and drying it with a hairdryer; this was done to remove any impurities such as silicon carbide which might have embedded into the sample during the grinding process. Thereafter, the samples were inspected under a Leica MZ 8 light microscope. Before

a finer grit grinding paper could be used, the sample was ensured to be scratch free and all striations were in the same direction. The polishing process entailed the use of a Struers Tegramin-25 automatic polisher. Both Struers DAC and NAP polishing pads, each with a different micron polishing grain were used. Each pad, with a corresponding water based diamond suspension, was used in a specific sequence for a specified period of time, as detailed in Table 3.2.2-1.

Table 3.2.2-1: Specifications of the polishing process.

Polishing Pad	Lubricant	Duration (minutes)
DAC	DiaDuo-2 (3 µm)	5
NAP	DiaDuo-2 (1 µm)	5
NAP	Water	5

After grinding and polishing processes were completed, each sample was thoroughly cleaned in an ultrasonic ethanol bath. A 4 % Nital solution was used for chemical etching. Initially the Nital solution consisted of 96 % methanol and 4 % nitric acid, but after trying this solution it was found to be ineffective. A more effective solution was found by replacing the methanol with ethanol whilst keeping the same volume ratio. Samples were placed on a flat, dry surface, and a pipette deposited Nital over the sample's surface. Once the sample's surface turned cloudy, the etching process was deemed complete and the excess Nital was flushed away with ethanol. Samples were dried once more before a Zeiss Primotech light microscope was used to analyse the microstructure. Micrographs were captured at objective magnifications of 5, 10 and 20 times.

The two welds used for experimental investigation in this study were the turbine housing weld (THW) and the loop pipe weld (LPW). In order to reveal the chemical composition of the steam penetration parent material (PM), and the two different weld filler materials, spectrographic analysis was conducted. Table 3.2.2-2 lists the chemical composition by weigh percentage (wt %).

Table 3.2.2-2: Weld zone a chemical composition by wt % [71]–[73].

	C	Cr	Si	Mn	P	Mo	Ni	Cu	Al	V	Fe
PM	0.236	1.33	0.262	0.655	0.018	0.691	0.093	0.129	0.033	0.27	96.03
LPW	0.085	0.464	0.322	0.919	0.013	0.947	0.026	0.027	0.004	0.48	96.58
THW	0.060	0.656	0.460	0.685	0.006	0.500	0.081	0.114	0.002	0.25	97.05

The carbon wt % for all three materials was less than the 0.76 wt % carbon eutectoid point, which made all three materials hypo-eutectoid steels. In general, during welding, temperatures are in excess of 1 000 ^{o}C; this results in the microstructure transforming into the fully austenitic region. As the weldment is allowed to cool and stress relaxes post welding, a variation in grain size in the parent material develops due to varying times at peak temperatures and uneven cooling rate. The variation in grain sizes are collectively known as the heat affected zone. Material closest to the fusion line will experience the highest peak temperature and the fastest cooling rate, and will allow for the formation of coarser grains. Material further away from the fusion line will experience a lower peak temperature and a slower cooling rate, which drives the formation of smaller and finer grains. Figure 3.2.2-1 illustrates the heat affected zone for each of the two welds. The CGHAZ and the FGHAZ are much more influenced by the peak temperature during the welding cycle. The higher the peak temperature, the greater the chance of grain growth in the austenitic condition.

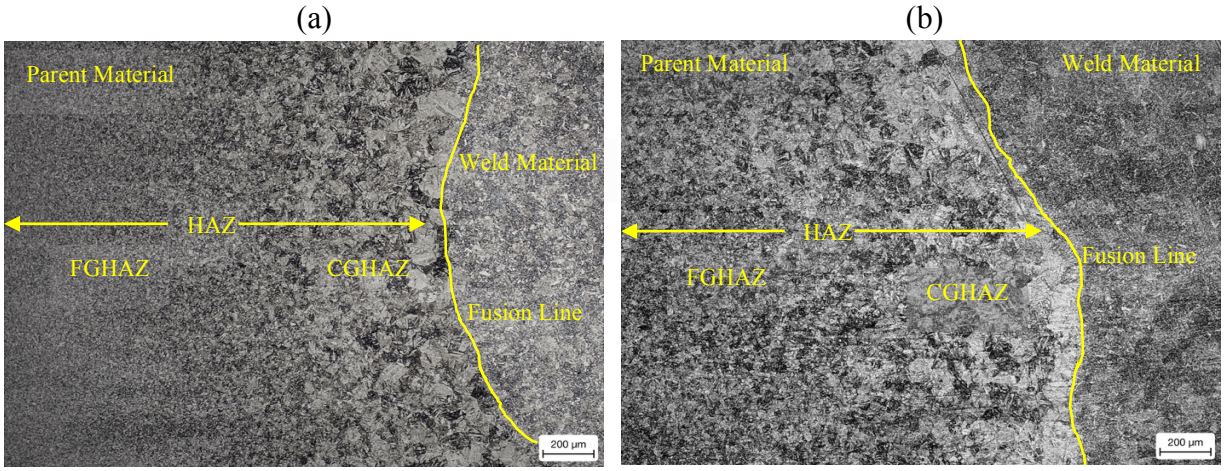

Figure 3.2.2-1: Micrographs of the (a) THW and (b) LPW weld joints at the interface between the weld material and the parent material.

Both the THW and the LPW have been exposed to operating conditions in the range of 300 - 535 ^{o}C and 4 - 16 MPa for approximately 24 years (± 212 000 hours). This operating temperature is below the 727 ^{o}C phase transformation temperature and therefore the parent

material will comprise mostly of ferrite and cementite ($\alpha + Fe_3C$). Figure 3.2.2-2 illustrates a more detailed micrograph of the HAZs from each of the two weld zones.

The HAZ will exhibit a combination of different microstructural phases as a result of the post weld heat treatment (PWHT). The grain size is dependent on the cooling rate experienced by that portion of the HAZ during the PWHT. From the fully austenitic region, a fast cooling rate will motivate the formation of martensite; whist a moderate or slow cooling rate will cause the formation of either bainite or pearlite. The microstructural alterations in the HAZ are characterised in detail in Figure 3.2.2-2.

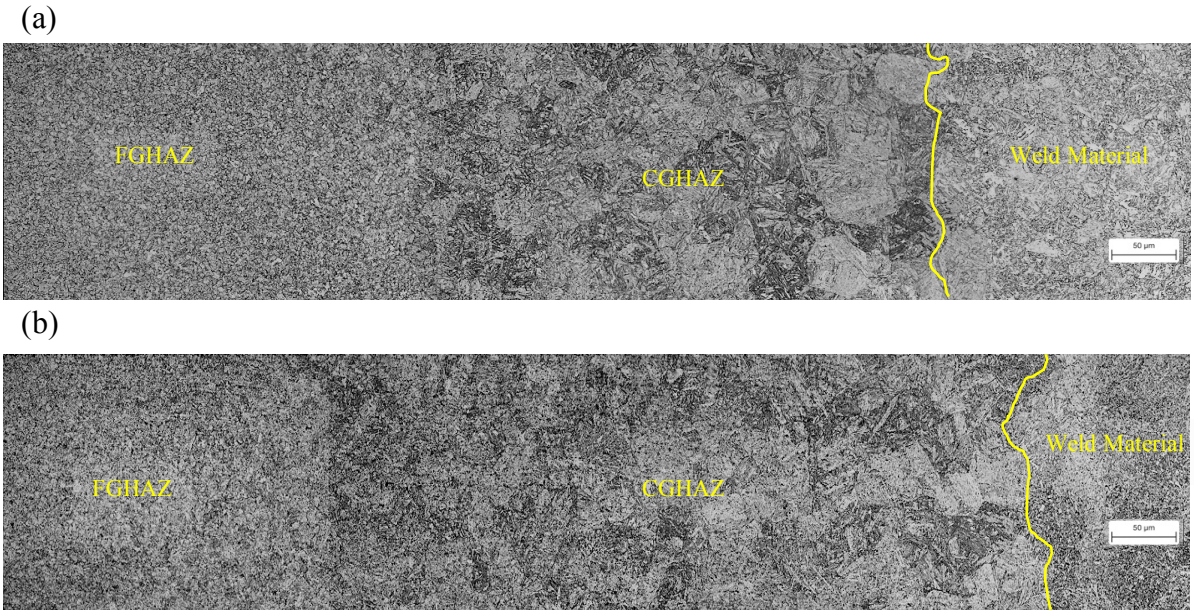

Figure 3.2.2-2: Micrographs of the (a) THW and (b) LPW HAZ at a magnification of x20.

3.2.3 VICKERS HARDNESS PROFILE

In order to examine the variation of hardness across the weld zones, Vickers micro-hardness tests were conducted along samples machined from each of the two weld zones. Hardness tests served to further validate the location and length of the heat affected zone in each of the two welds. Hardness values can be used as a check for the formation of microstructures having low ductility and toughness which are prone to cracking.

Vickers micro-hardness tests were performed using a Dura Scan EMCO tester along the transverse direction of the welds. All tests were performed on small rectangular specimens of

dimensions 28 mm x 10 mm x 10 mm. In order to produce a smooth surface, all specimens were ground and polished using a one-micron water based diamond suspension prior to hardness testing. All tests were conducted at intervals of 0.3 millimetres, using a constant load of 300 g ($HV_{0.3}$). Figure 3.2.2-1 and Figure 3.2.3-2 illustrate the micro-hardness distribution across each of the weld zones.

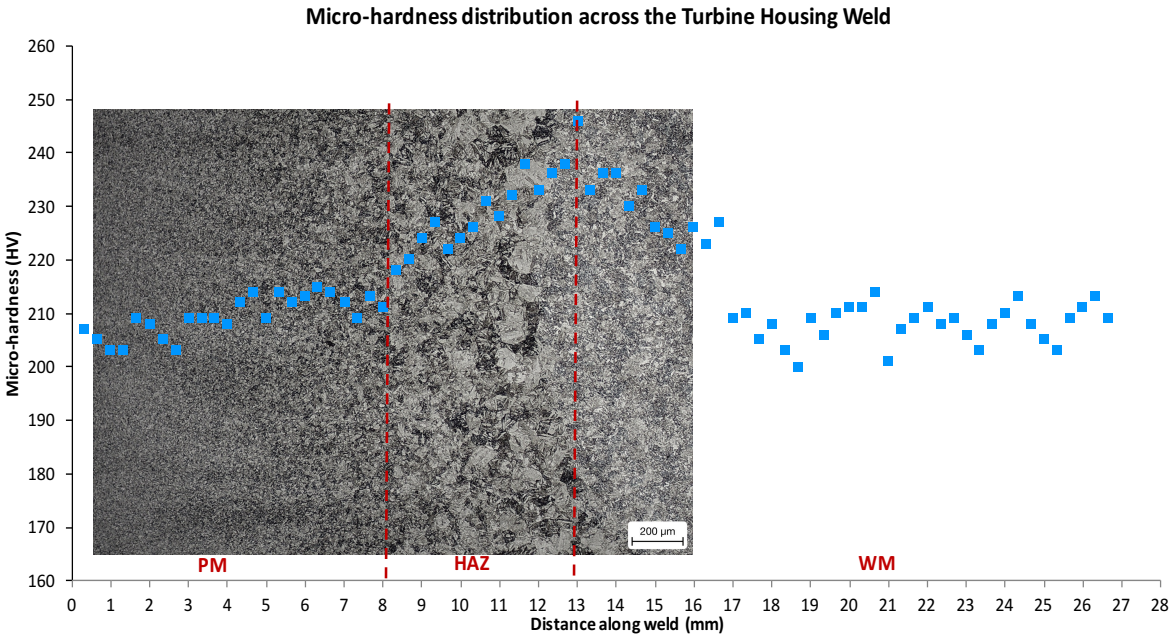

Figure 3.2.3-1: Micro-hardness distribution along the transverse direction of the turbine housing weld.

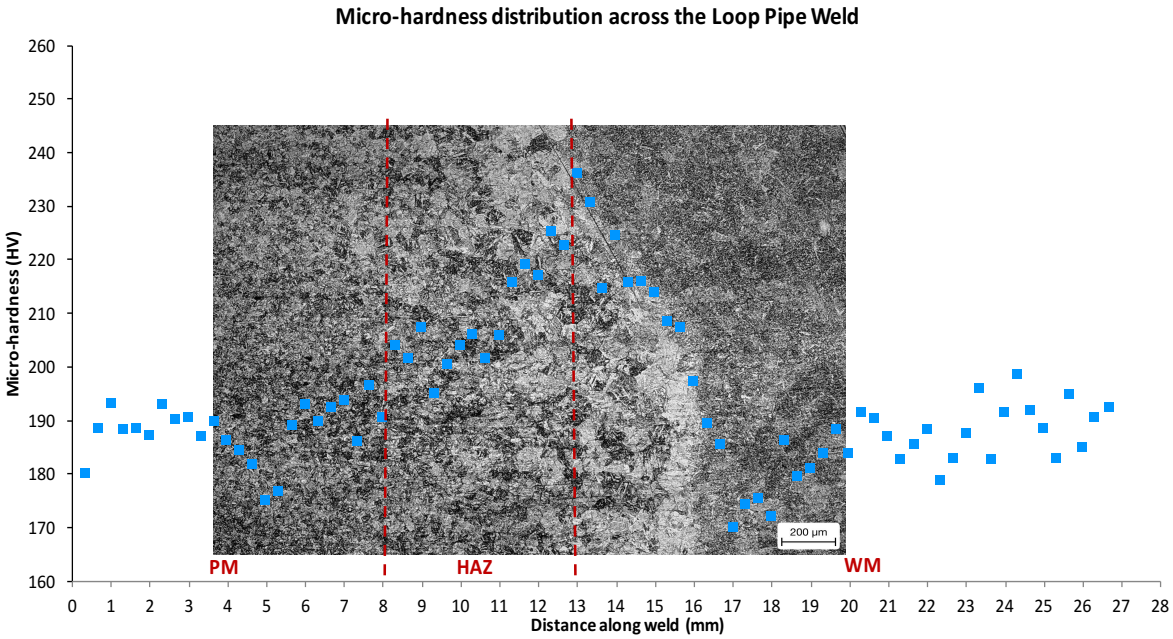

Figure 3.2.3-2: Micro-hardness distribution along the transverse direction of the loop pipe weld.

From the hardness distributions there are three distinct regions, namely the PM, HAZ and WM. Moving from the WM and into the HAZ, the hardness increases linearly to a peak in the region of the FL, which also indicates the start of the HAZ; 245 HV in the THW, and 235 HV in the LPW. Thereafter, the hardness gradually decreases to the level of the parent material; 210 HV in the THW, and 190 HV in the LPW. A study conducted by Schäfer found that the abrupt decrease of hardness value near the FL was related to the existence of delta ferrite in the parent material [60]. Delta ferrite is soft and increases both ductility and toughness.

The hardness values across the LPW were not as high as that of the THW. This finding suggested that due to the higher temperature and pressure experienced by the LPW, the LPW would have undergone a larger degree of thermal softening, and would therefore have a weaker hardness profile. From both hardness profiles, it was established that the length of the HAZ in each of the welds was approximately four millimetres wide.

3.2.4 ETCHING OF TENSILE SPECIMENS AND SPATIAL CALIBRATION

After the Gleeble tensile specimens were machined following the geometry modifications outlined in section 3.2, each specimen was hand ground using Struers waterproof silicon carbide paper, namely the 500, 800 and 1 200 grit. Thereafter the gauge length was chemically etched by applying a 4 % Nital solution swab over the gauge length. Once the position of the fusion line was exposed, the remaining Nital was flushed off with ethanol. The specimen was then dried using a hand held drier and the location of the fusion line was engraved onto the adjacent face of the specimen. Establishing the location of the fusion line was critical for spatial calibration of the microstructure and hardness data. In addition, the location of the fusion line was used for the placement of thermocouples across the gauge length; this was used to monitor the thermal profile of the specimen which in turn acted as a physical feature for spatial calibration of thermal data with strain displacement data.. Figure 3.2.4-1 illustrates the location of the fusion line after being chemically etched.

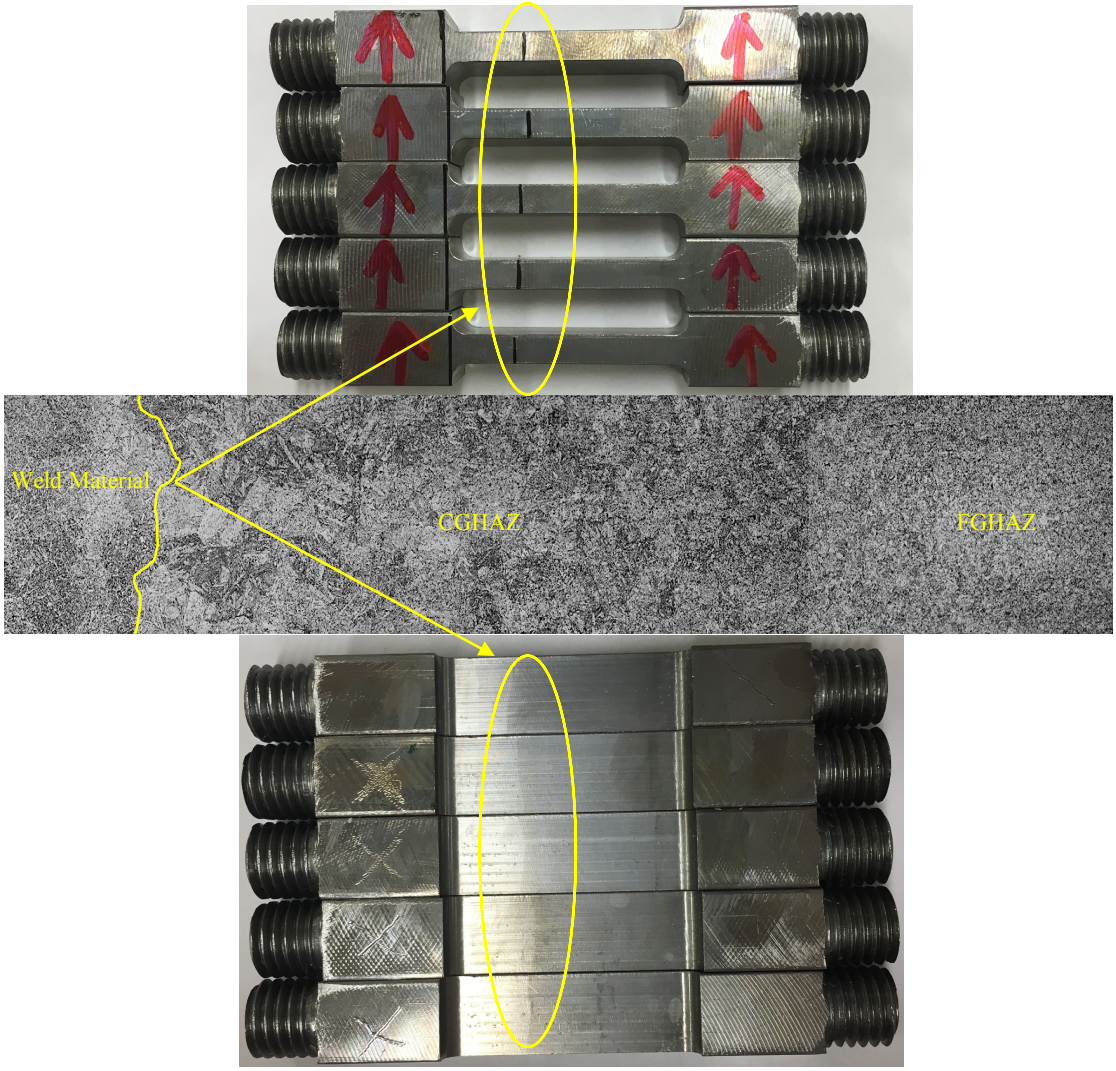

Figure 3.2.4-1: Photograph of an etched specimen revealing the location of the fusion line.

3.3 GLEEBLE THERMOMECHANICAL SETUP

In order to meet the objective of measuring strain localisation at elevated temperatures, a Gleeble 3 800 thermomechanical simulator was used to apply a tensile load to the specimen at a constant prescribed temperature. The Gleeble system employs direct resistance joule heating, and by maintaining a constant current density allows for uniform heating of the specimen. The copper wedge grips serve as electrical conductors for direct resistive heating between the aluminium pocket jaws and specimen.

To accommodate a shorter Gleeble specimen with an exposed gauge length of 30 millimetres, modifications to the existing Gleeble stiff load train had to be made. The purpose of the stiff load train was primarily to ensure adequate contact during initial heating of the specimen, and secondly to prevent the Gleeble wedge grips from buckling during mechanical loading. Figure 3.3-1 (a) illustrates the existing Gleeble tensile load train set up; components labelled B, C, D, E and F together make up the stiff load train.

The copper wedge grips (labelled as component B) serve as electrical conductors for direct resistive heating between the aluminium pocket jaws and specimen. To accommodate for a shorter tensile specimen whilst maintaining the same exposed gauge length, it was decided that the width of these copper wedges had to be reduced to approximately half of their original width. As a result of this reduction in width, a compensation elsewhere in the stiff load train in turn had to be made. The end spacers (component D) were identified as the simplest component to modify in order to compensate for this adjustment. Therefore, by decreasing the width of the copper wedge grips, and by subsequently increasing the width of the end spacers, the exposed specimen's gauge length was retained. An exposed gauge length of at least 30 millimetres was require for two reasons; firstly, for calibrating the DIC system, and secondly, to allow for full field deformation monitoring across the entire weld zone. The alignment adapters (component C), locknuts (component E), and tightening nuts (component F) dimensions remained unchanged Figure 3.3-1 (b) illustrates the new Gleeble tensile load train after all modifications were made. The drawings for the copper wedge grips and end spacers can be found in Appendix 8.2.

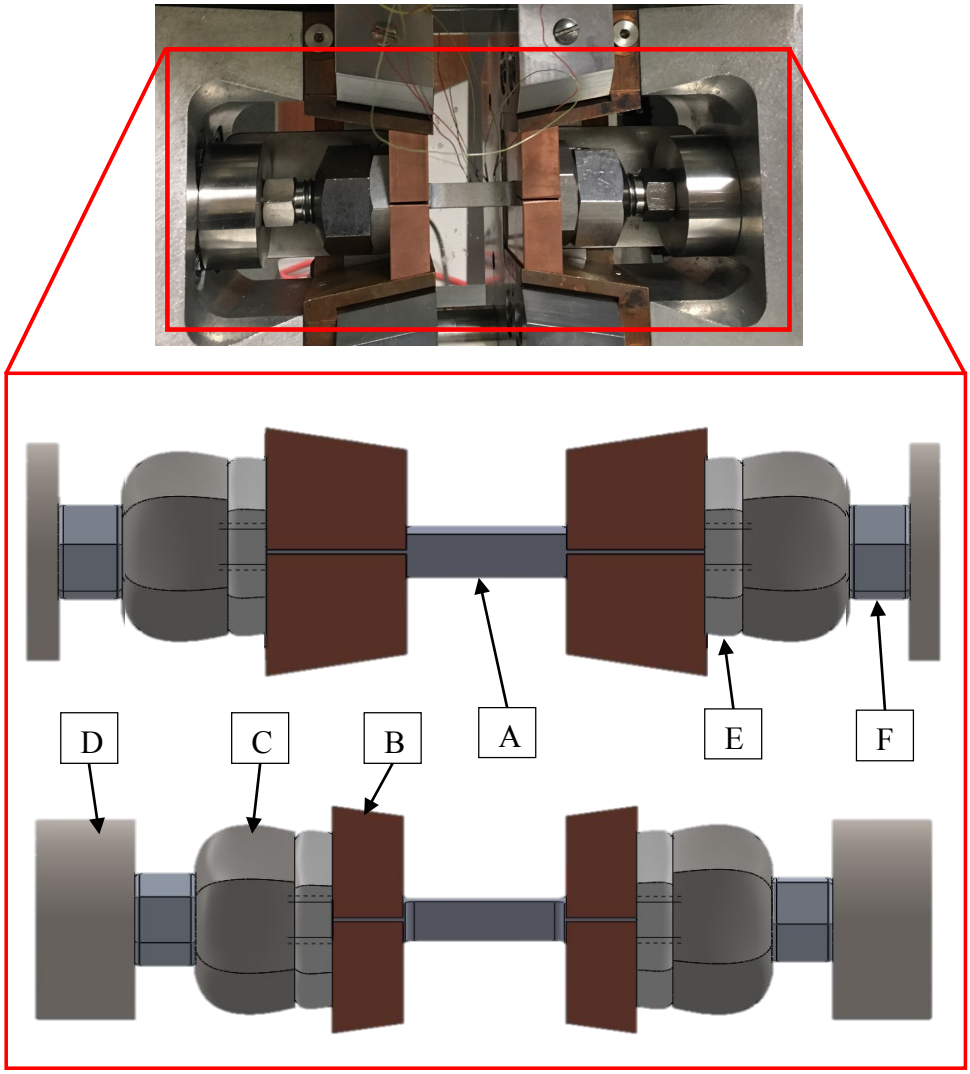

Figure 3.3-1: Schematic illustration of the (a) existing Gleeble stiff load train setup and the (b) modified Gleeble stiff load train setup.

To ensure that there was sufficient contact between the pocket jaws and specimen for direct resistance joule heating, the Gleeble was first programmed into force control to apply a preload. Thereafter, the specimen was heated at a constant heating rate. Once the target temperature was reached and had stabilized, the Gleeble was then automatically switched into displacement control, where the specimen was extended at a constant predetermined strain rate. Figure 3.3-2 illustrates the Gleeble programmed mechanical and thermal profiles.

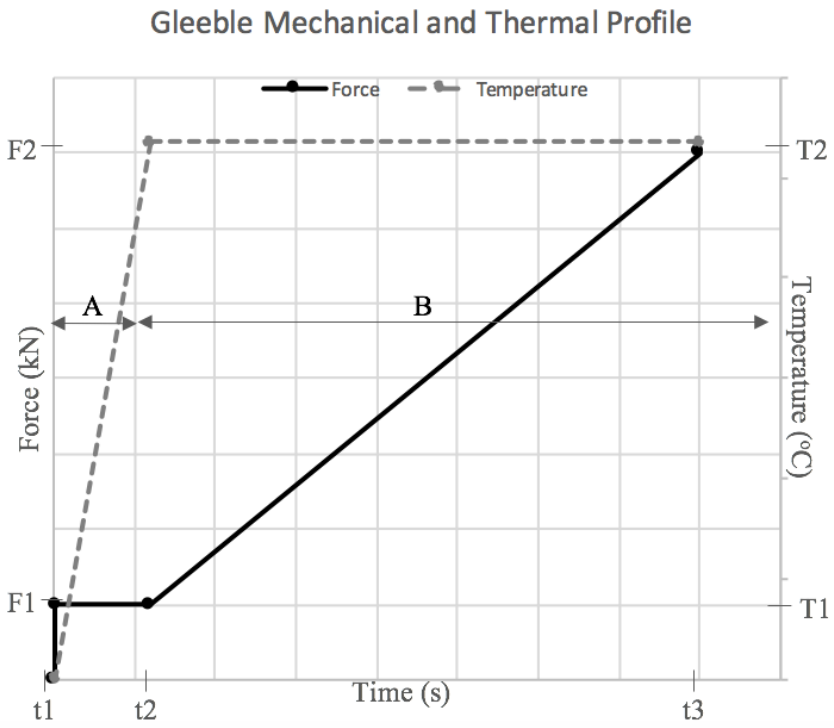

Figure 3.3-2: Gleeble mechanical and thermal loading profiles.

The first segment marked A, illustrated in Figure 3.3-2, was the preload phase of the simulation. In this phase the Gleeble was programmed in force control, and a preload tensile force of 2 kN was reached within a period of 2 seconds (t1). This preload force was induced to allow for sufficient contact for heating of the specimen to occur, and was maintained up until the target temperature was reached (t2). For the room temperature simulation, the preload was maintained for a short 10 seconds, whilst for the 300 ^{o}C experiment the 2 kN preload was applied for 90 seconds, and for the 535 ^{o}C experiment the preload was applied for 120 seconds. Once the target temperature was reached for each of the three different types of experiments, the Gleeble was automatically switched into stroke control. In this segment of the simulation, marked as B in Figure 3.3-2, the crosshead speed of the stroke was the controlling element, and extended the specimen at a strain rate of 50 $\mu\varepsilon.s^{-1}$. Force, time, temperature, strain, and stroke position were recorded by the Gleeble QuickSim software at a frequency of 10 Hz.

3.4 MONITORING & MODIFICATION OF THE SPECIMEN'S THERMAL PROFILE

The large thermal gradient present at the centre of the specimen as a result of direct resistant heating is undesirable for mechanical testing of strain localisation, as each section of the material when loaded will deform by different amounts due the variation of the temperature dependent flow properties. Thermocouples and radiometric images were used to monitor and assess the thermal gradient across the specimen's gauge length at elevated temperatures. With the aim of achieving a uniform thermal gradient further modifications to the specimen's geometry was made.

3.4.1 MONITORING THE THEMRAL PROFILE ACROSS THE SPECIMENS GAUGE LENGTH

In order to measure and monitor the temperature profile, four K-type thermocouples were spot welded, using a DSI thermocouple welder; this was done after the speckle pattern was applied. In general, thermocouples are used to evaluate the temperature of a surface by measuring the potential difference between two metals joined to form a junction. The K-type thermocouples used were nickel based, consisting of Chromel (nickel-chromium) and Alumel (nickel-aluminium). Assuming a symmetrical heat distribution, thermocouples were welded along one half of the specimen's gauge length.

The first thermocouple (TC 1) was welded at the centre of the gauge length, the control thermocouple (TC 3) was welded on the fusion line, approximately five millimetres away from the TC 1. The remaining two thermocouples (TC 2 & TC 4) were each welded on either side of TC 3, 3 millimetres away, as illustrated in Figure 3.4.1-1. This is in accordance with Gleeble standards, which stipulated a minimum spacing between successive thermocouple weld beads to 2.5 millimetres. A more complete thermal distribution across the specimen's gauge length would have been possible by welding on more thermocouples; however, the number of thermocouples was limited by the Gleeble system to four. To ensure that the thermocouples remained isolated from each other and the surroundings, ceramic tubing were placed over the thermocouples.

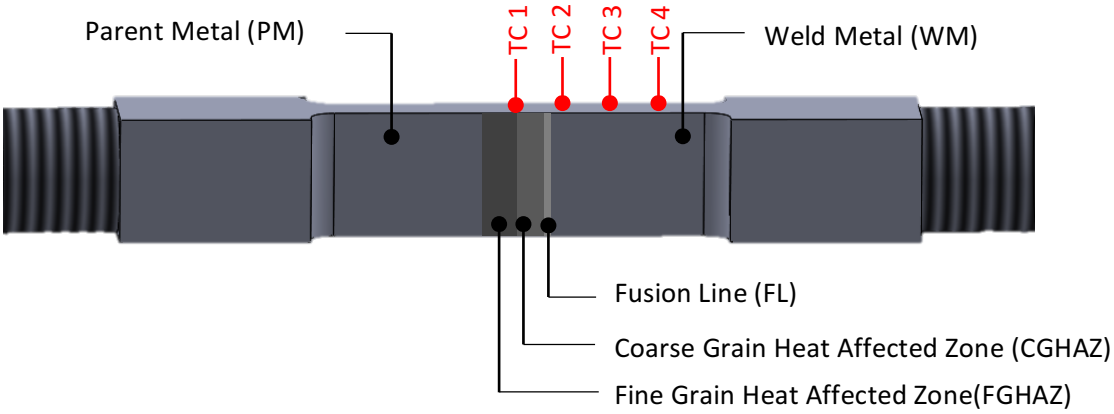

Figure 3.4.1-1: Schematic of a tensile specimen illustrating the placement of thermocouples.

In addition, infrared (IR) imager was employed to attain a full thermal profile across the entire specimen. Radiometric images were captured by a 5-megapixel Fluke Ti400 Thermal infrared imager (IR). The IR imager was rated to detect temperatures from -20 ^{o}C to 1 200 ^{o}C. The IR imager was mounted onto a separate tripod and positioned at the back of the Gleeble vacuum chamber, approximately 250 millimetres away from the specimen. Radiometric images were capture through a Fluke ClirVu CV200 IR viewing window which was as installed with a viewing aperture of 43 mm and a window thickness of 2 mm.

Through the visible-IR window the imager was focused onto the specimen and was able to capture thermal radiation across the specimen's gauge length. Figure 3.1-1 illustrates the positioning of the IR camera in relation to the DIC system and the Gleeble. After radiometric images were recorded, they were post processed using SmartView 3.11 imaging software. In order to accurately measure the temperature of the specimen, the surface emissivity and transmission correction of the IR window were adjusted until the maximum temperature corresponded to the Gleeble control thermocouple (TC3). An approximate transmission correction factor of 53 ± 2 % was used.

3.4.2 MODIFICATION OF THE SPECIMENS THERMAL PROFILE

The modified specimen geometry and tensile testing arrangements outlined in sections 3.2 was used to evaluate the temperature profile across the specimen's gauge length. In this study, tensile tests were conducted at three different temperatures; namely at room temperature (RT

± 24 ^{o}C), at an intermediate temperature (300 ^{o}C), and at the steam penetration operating temperature (535 ^{o}C). An initial experiment was conducted at 535 ^{o}C at a strain rate of 50 $\mu\varepsilon.s^{-1}$. The 535 ^{o}C experiment was selected to evaluate the thermal profile across the specimen as it was believed to exhibit the largest thermal distribution across the specimen when compared to the experiments at 300 ^{o}C and 24 ^{o}C.

The thermal profile of the specimen was evaluated by both measurements received from the Gleeble thermocouples, as well as from the IR camera. A dummy specimen was loaded into the Gleeble and before the thermal profile script could proceed, the IR camera was focused and initiated.

Figure 3.4.2-1 illustrates the comparison between the temperature data recorded by the IR camera and the thermocouples for a thermal experiment conducted at 535 ^{o}C. The temperature profile is plotted along the longitudinal direction with the centre of the specimen taken as the zero position. The temperature per pixel data recorded by the IR imager was converted to an equivalent temperature per millimetre value before being plotted in Figure 3.4.2-1. A least squares regression quadratic fit, with a coefficient of determination of 0.99, was applied to the temperature data recorded by the IR imager. A symmetrical parabolic thermal profile about the centre of the specimen was found. This finding was in accordance with steady state heat flow along the longitudinal direction, as reported by Walsh et. al who suggested that this form of a parabolic thermal profile was dependent on the specimen's material properties, specimen geometry and the testing temperature [40].

From Figure 3.4.2-1, it can be seen that the highest temperature was recorded at the centre of the specimen; this was due to the direct resistive heating of the specimen which occurred from either end of the specimen. Identical wedge grips were used on either end of the specimen, and therefore a symmetrical parabolic shape about the centre of the specimen was expected. The sharp decrease in temperature about the centre point was as a result of heat loss to the surroundings due to convection and radiation, as well as due to conduction along the specimen and into the wedge grips. These findings are in agreement with work done by Walsh et. al and Farup et al. [40], [61].

The four K-type thermocouples were welded along one half of the specimen's gauge length at offsets of 4 millimetres, 7 millimetres and 10 millimetres from the centre of the specimen. Due to the parabolic shape of the thermal profile, the thermocouple data was mirrored about the gauge length's centre point; this was done to achieve a larger thermal field of view. The average thermocouple data was taken from the instant the control thermocouple had reached 535 ^{o}C, until the test had concluded, these values are plotted in Figure 3.4.2-1 by the blue circular indicators.

The thermal profile readings between the IR imager and the thermocouples were in good agreement, with a maximum difference of approximately 7 ^{o}C at TC 1 (at the centre of the gauge length). The temperature difference between the centre of the specimen and the fusion line (between TC1 and TC3) was 115 ^{o}C. The marked thermal gradient decrease about the centre point was inherent of isothermal temperature planes. This thermal profile was undesirable for accurate mechanical property measurements as the variation of temperature dependent properties along the specimen gauge length would have caused each section of the specimen when loaded to deform by different amounts [62], [63].

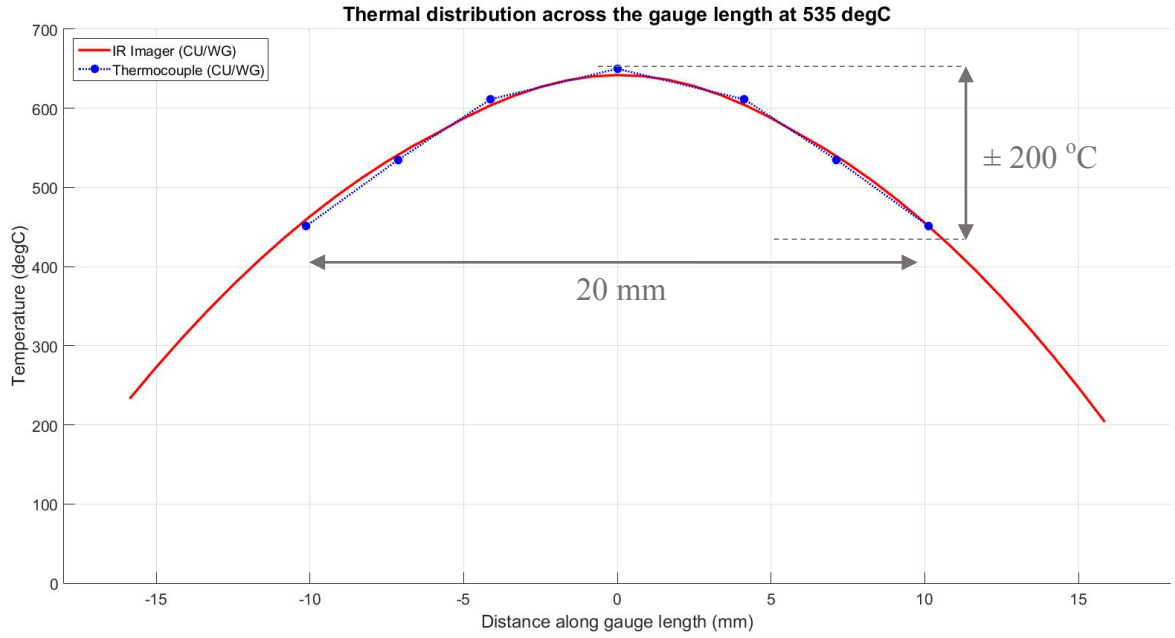

Figure 3.4.2-1: Scatter plot comparing temperature readings between the thermocouples and IR thermography at 535 ^{o}C.

In order to improve accuracy, the specimen geometry was further refined. After careful analysis of the 84 millimetre long specimen geometry, it was understood that the ends of the tensile specimen were favourable heat sink locations. In an effort to reduce these heat sinks, a 4

millimetre diameter hole was drilled in the ends of the specimen to a depth of 20 millimetres to effectively provide hollow ends. The removal of material from the ends of the specimen would increase the overall resistance and would consequently allow for a more uniform thermal heating profile.

The thermal profile experiment at 535 ^{o}C was repeated with the refined specimen geometry; however, the thermal gradient remained significant, but the temperature difference between TC1 and TC3 had now decreased to 107 ^{o}C, as illustrated in Figure 3.4.2-2 by the green circular indicators. The experiment was repeated once more; this time the four millimetre hole was extended to a six millimetre hole, and the temperature difference between TC1 and TC3 had now decreased to 68 ^{o}C, as illustrated by the cyan circular indicators in Figure 3.4.2-2.

Although the removal of material improved the thermal profile, the magnitude of the thermal gradient was also found to be influenced by the wedge grip's material. S Norris et al reported that the current copper wedge grips (CU/WG) produced the largest thermal gradient and could be replaced by suitable stainless steel wedge grips (SS/WG) [41]. The exchange from copper to stainless steel wedge grips would decrease the thermal gradient however; the Gleeble heating rate would have to be considerably reduced. Since the heating rate was not of major concern in this study, this modification to stainless steel wedge grips was accommodated.

In a further attempt to improve the thermal profile, the copper wedge grips were exchanged for stainless steel grips, and six millimetre diameter holes were drilled into either end of the specimen. As a result, the thermal gradient had improved considerably with these adjustments. The overall temperature difference between TC1 and TC3 had now reduced from 115 ^{o}C to 40 ^{o}C, illustrated by the magenta circular indicators in Figure 3.4.2-2. Although this is a considerable improvement, a temperature difference of 40 ^{o}C between the centre of the specimen and the fusion line would have still caused each section of the specimen when loaded to deform by different amounts, and will therefore exhibit different material properties.

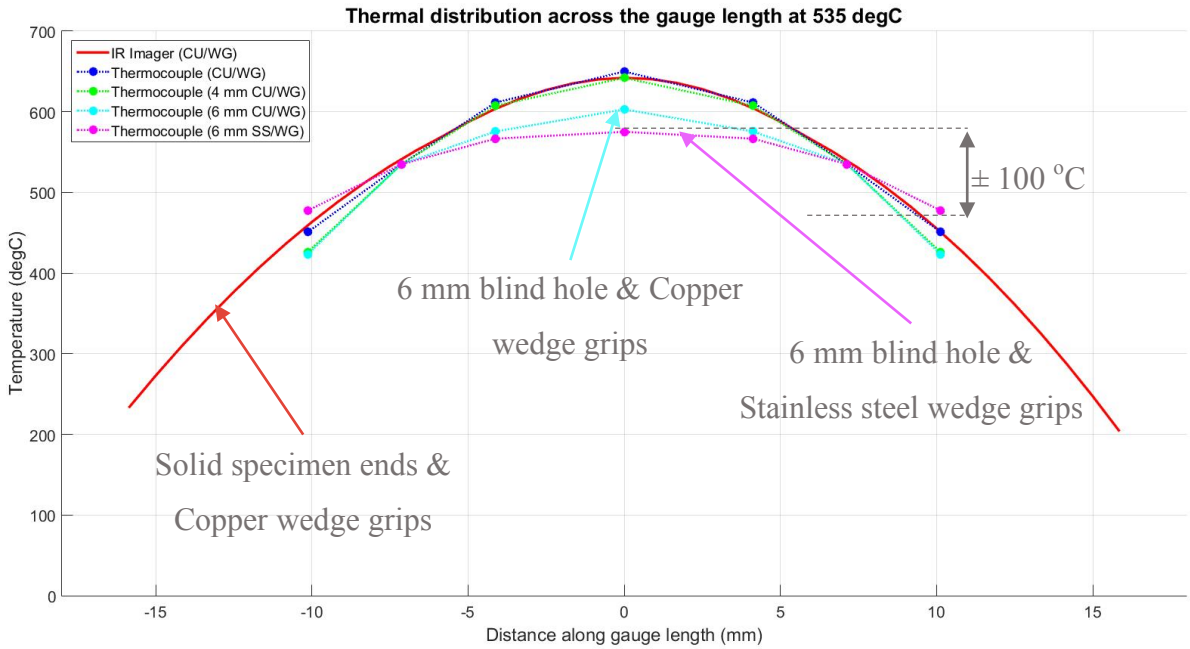

Figure 3.4.2-2: Scatter plot comparing temperature readings between the thermocouples and IR thermography at 535 °C incorporating various specimen modifications.

These findings suggested that there was a need to further improve the specimen thermal profile. In order to expand the length of the hot zone, it was decided that the length of the reduced cross-section gauge length would need to be increased. The aim of this modification was to increase the length of the tensile specimen towards that of a conventional Gleeble tensile specimen. By doing so there would be a more uniform thermal profile across a longer gauge length. Due to the specimen machining constraints mentioned in section 3.2 the only feasible approach to increase the gauge length of the specimen was to weld a piece of mild steel onto the end of the existing specimen. The modified specimen geometry is illustrated in Figure 3.4.2-3.

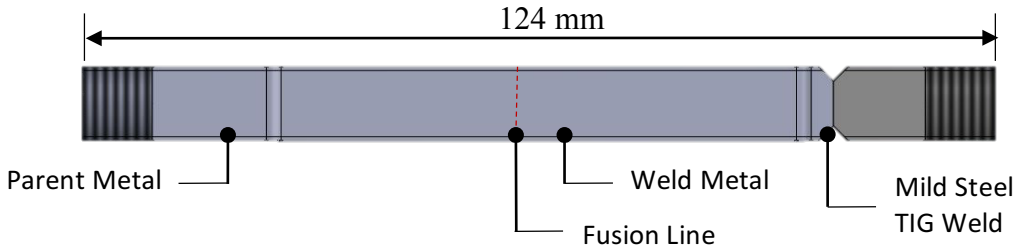

Figure 3.4.2-3: Schematic illustration of the proposed modifications of Gleeble tensile specimen.

Welding of another material onto the specimen inevitably introduced another variable into the experimental matrix which would influence the performance of the specimen. Therefore, in order to invalidate the influence of this modification, the welded material was designed to be welded away from the fusion line, and into the thicker region where the Gleeble wedge grips attach, as illustrated in Figure 3.4.2-3. The add-on weld was sufficiently far away from the test fusion zone, thus it had no effect on the weld zone in any way. Figure 3.4.2-4 illustrates the longer modified tensile specimen in relation to the short specimen.

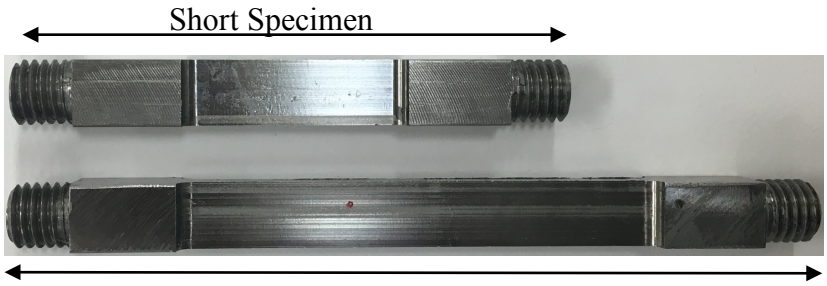

Figure 3.4.2-4: Gleeble tensile specimens.

The thermal profile experiment was repeated with the new longer modified Gleeble specimen. The blue and red plot in Figure 3.4.2-5 illustrates the thermal profile across the longer modified Gleeble specimen at 535 ^{o}C. The longer specimen had a remarkable improvement on the thermal profile. The temperature difference between TC1 and TC3, which was approximately six millimetres, had now reduced from 40 ^{o}C to 9 ^{o}C. A temperature difference of 9 ^{o}C between the centre of the specimen and the fusion line was a more adequate condition for accurate material and mechanical property assessment.

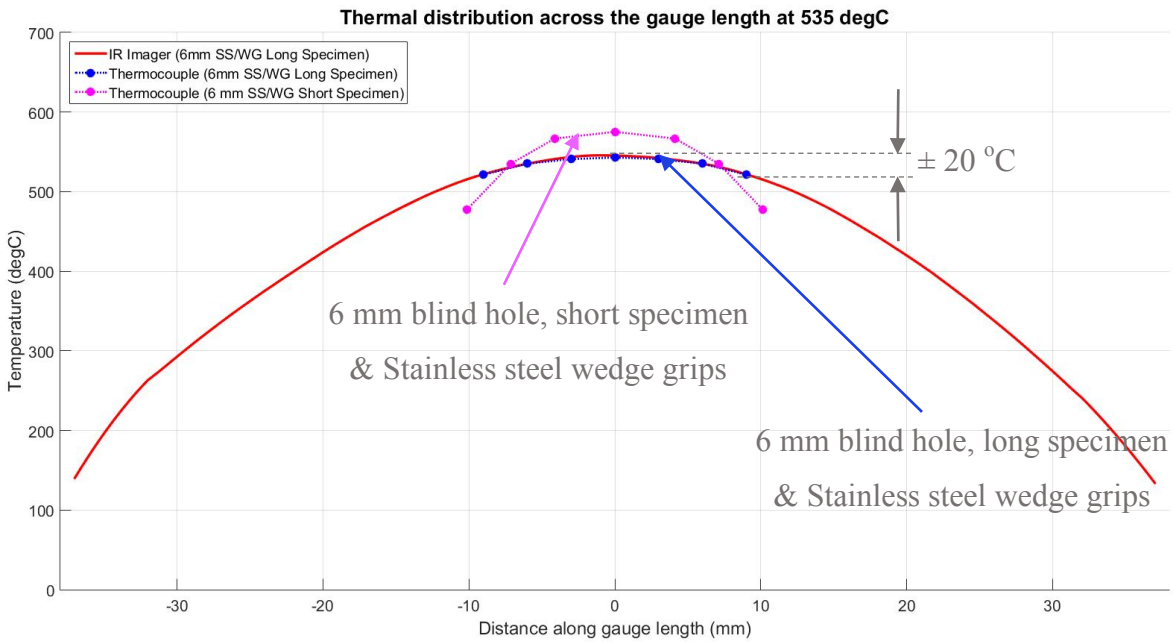

Figure 3.4.2-5: Scatter plot comparing temperature readings between the thermocouples and IR thermography at 535 °C using specimens of different lengths.

For the sake of completeness, the identical thermal profile experiments were repeated at a temperature of 300 °C. The thermal gradient was not as severe as the experiment at 535 °C. However, a similar trend of improving the thermal gradient with the above mentioned modifications was also found. By replacing the copper wedge grips with stainless steel ones, and by drilling in six millimetre diameter holes through the ends of the specimen, the temperature reading between TC1 and TC3 was improved from being 22 °C to 7 °C, as illustrated in Figure 3.4.2-6. This thermal profile was adequate for accurate material property evaluation across the gauge length and it was found not necessary to also increase the length of the specimen as was the case for the 535 °C tests as explained below.

The 300 °C thermal profile experiment was repeated on a full length tensile specimen. As with the 535 °C, the application of a longer specimen did continue to improve the thermal profile across the gauge length. The thermal profile between TC1 and TC3 had improved to 4 °C, as illustrated in Figure 3.4.2-7. Due to the additional machining time required to TIG weld a mild steel piece to manufacture a longer specimen, it was deemed acceptable to use the short specimen for the 300 °C experiments.

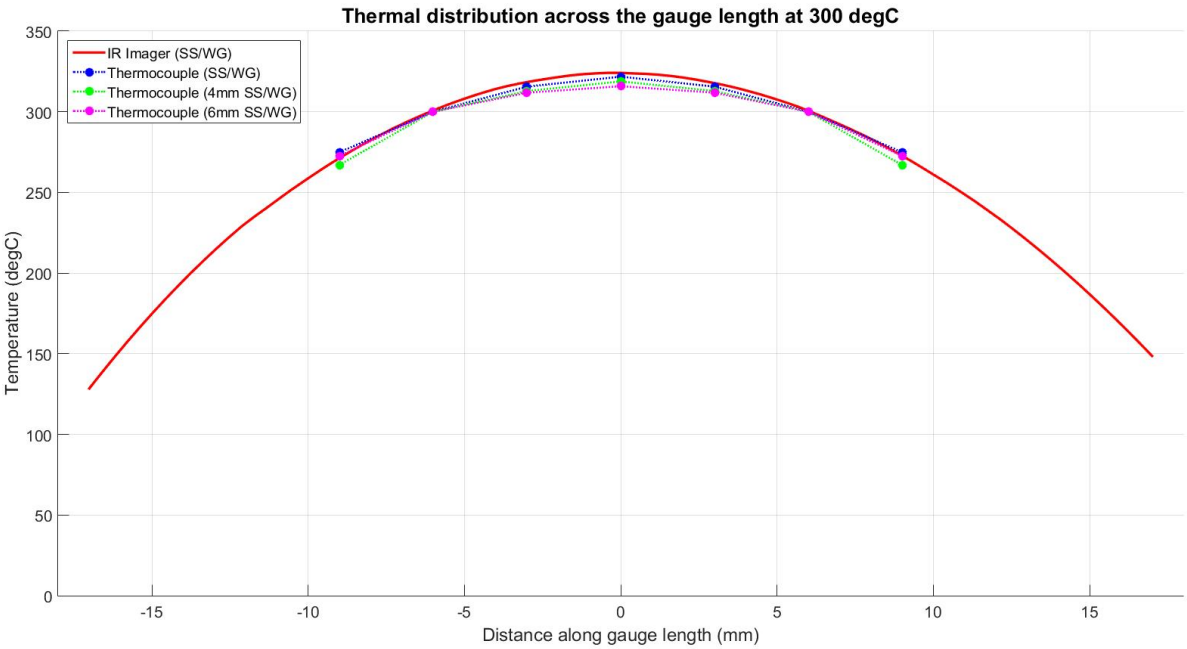

Figure 3.4.2-6: Scatter plot comparing temperature readings between the thermocouples and IR thermography at 300 ^{o}C incorporating various specimen modifications.

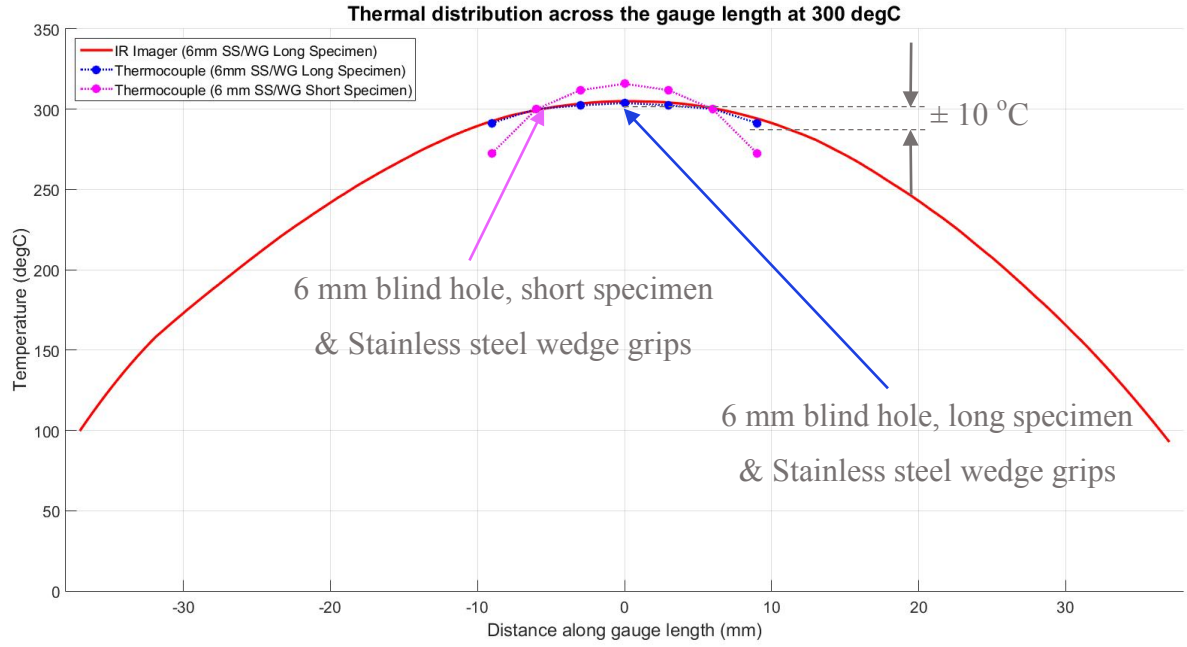

Figure 3.4.2-7: Scatter plot comparing temperature readings between the thermocouples and IR thermography at 300 ^{o}C using specimens of different lengths.

3.5 DIC SETUP AND PARAMETER CONFIGURATION

Application of a speckle pattern to the specimen's gauge length allowed for the DIC system to measure localised strain across the weld zones during mechanical tensile loading at elevated temperatures. The DIC system was positioned at the front of the Gleeble as detailed in section 3.1, and comprised of a single high resolution digital camera (used to record full field in-plane deformation), LED lighting (used to reduce the effects of surface radiation), a calibration plate, image grabbing software (used to record images at a set frequency), and DIC software (used to post process the deformation into localised strain fields).

3.5.1 APPLICATION OF THE SPECKLE PATTERN

To perform DIC, a high contrast image is required. In this study, this requirement was satisfied by applying a random high contrast black and white speckle patterned paint to the specimen's gauge length.

To ensure that the paint adhered to the tensile specimen, a dummy specimen's gauge length was abraded by hand sanding it with Struers 80 grit waterproof silicon carbide paper. Thereafter, a white high temperature (704 – 1 093 ^{o}C) VHT ® FlameProof paint was sprayed over the gauge length with an aerosol can held approximately 30 cm above the gauge length. Once the white paint had cured for approximately 1 hour, a similar high temperature black VHT ® FlameProof paint mist was lightly sprayed over the white base coat, creating a high contrast speckle pattern. Thereafter the specimen was placed in a furnace and the heat treatment curing process suggested by the paint manufacture was followed. Once the paint was completely dry, the three phase curing process followed entailed heating the specimen to 120 ^{o}C for 30 minutes, cooling for 30 minutes, heating to 205 ^{o}C for 30 minutes, cooling for 30 minutes and heating to 345 ^{o}C for 30 minutes.

After the heat treatment curing process had completed, the dummy specimen's speckle pattern was assessed by loading it into the Gleeble chamber and simulating the mechanical loading and thermal heating profiles. Subsequently it was found that the speckle patterned paint was too brittle and had flaked off during the Gleeble simulation. This finding was not adequate for

measuring of strain localisation using DIC, as the correlation algorithm would not be able to measure the pixel deformations after the speckle pattern had flaked off.

In view of the brittleness of the paint, the speckle pattern application procedure was reviewed and possible sources of error were hypothesised as being due to the gauge length not being abraded adequately enough for adhesion of the paint and/or the speckled patterned paint layer was too thick. The type of high temperature paint was deemed adequate for this purpose as the temperature range rating of the paint was significantly higher than the maximum experimental temperature.

A second dummy specimen was prepared but this time the abrasion of the gauge length was increased. A sand blaster was used to roughen the specimen's gauge length; this was done to ensure maximum adhesion of the paint. Before the speckle pattern could be applied, the specimen was flushed with acetone to remove any foreign particles. Thereafter the white high temperature base coat was light sprayed across the gauge length; subsequently a mist of black paint was lightly sprayed over the white base coat. The heat treatment process recommended by the paint manufacturer was ignored as the maximum testing temperature was 535 ^{o}C and the high temperature paint was rated for application in the range of 704 – 1 093 ^{o}C. In substitution the speckle pattern was allowed to air cure for approximately 30 minutes before being loaded into the Gleeble for mechanical and thermal experiments. This time it was clearly evident that the quality of the speckle pattern adhesion had improved as it had not flaked off.

By following this application of the speckle pattern, it was found that maximum paint ductility was achieved when the gauge length was adequately roughened, when the paint coating was as thin as possible (a single layer), and when the speckle pattern was applied approximately 30 minutes before the tensile test. Figure 3.5.1-1 illustrates a specimen with the speckle pattern applied across it's gauge length, as well as a scaled image of a speckle pattern. On analysis of the speckle pattern it was found that the average speckle diameter was 0.09 millimetres (assuming circular speckles). Once the speckle pattern was applied, a reference point was lightly scribed onto the front face of the specimen along the centre line. This reference point was used during DIC post processing.

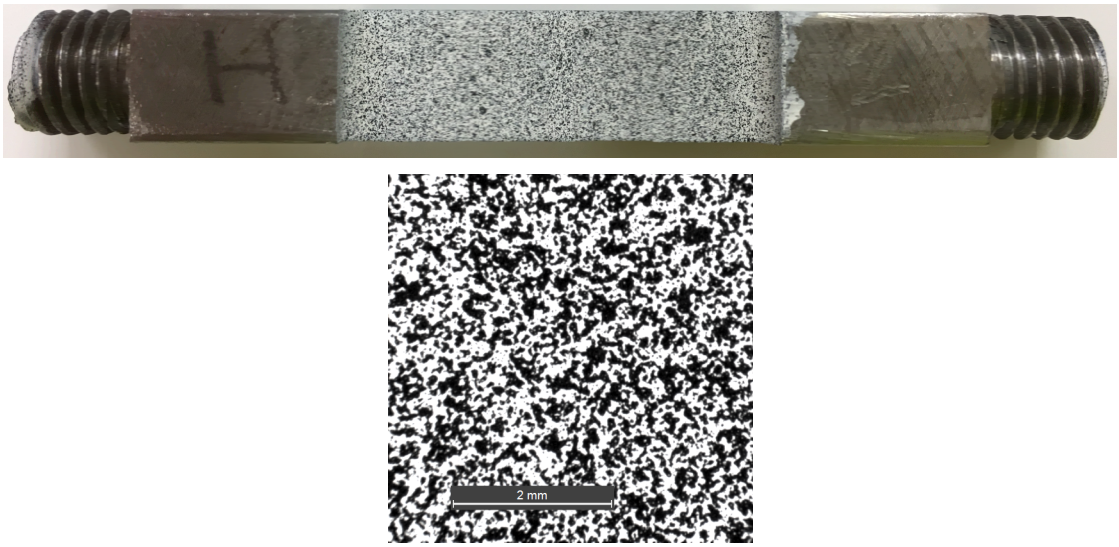

Figure 3.5.1-1: Photograph of speckle pattern applied across the gauge length.

In addition to applying a speckle pattern to the front face of the tensile specimen, the back face of the specimen was coated with a black coat of the high temperature paint. This was done to increase the emissivity of the specimen to ensure that accurate radiometric images were recorded by IR camera. By coating the back face of the specimen with black high temperature paint, the theoretical emissivity of the specimen increased to 94 %.

3.5.2 EQUIPMENT SPECIFICATIONS

A Basler 5-megapixel camera with a resolution of 2 592 x 1 944 pixels, equipped with an adjustable macro lens, was secured onto a stable tripod and positioned approximately 1.5 m away from the Gleeble chamber. This spacing allowed for adequate room for the Gleeble chamber door to be opened and closed without having to move the DIC system. Digital images of the speckle pattern were recorded through the Gleeble's front Pyrex window as the specimen was deformed. Image grabbing software, Pylon, was used to capture and store images at a set frequency of 2 Hz.

To maximise the signal to noise ratio, and to eliminate interruptions from surrounding light, a 10 W LED light was secured onto a separate tripod, and was used to illuminate the specimen placed within the Gleeble chamber. Due to experiments being conducted at a peak temperature of 535 ^{o}C, it was of concern that radiation emanating from the specimen would be significant and will introduce noise to the images captured by the DIC system. Therefore, to reduce the

effects of surface radiation, and to further maximise the signal to noise ratio at elevated temperatures, a blue Hoya B-440 lens filter with a wavelength range of 395 - 480 nm was fitted onto the camera lens during the initial dummy testing. Subsequently, it was found that the radiation emitted from the specimen at this temperature was minimal, and the use of the blue filters was in fact decreasing the signal to noise ratio. Therefore, for subsequent experiments the use of the lens filter was discontinued. Figure 3.5.2-1 illustrates the setup of the DIC equipment in relation to the Gleeble system.

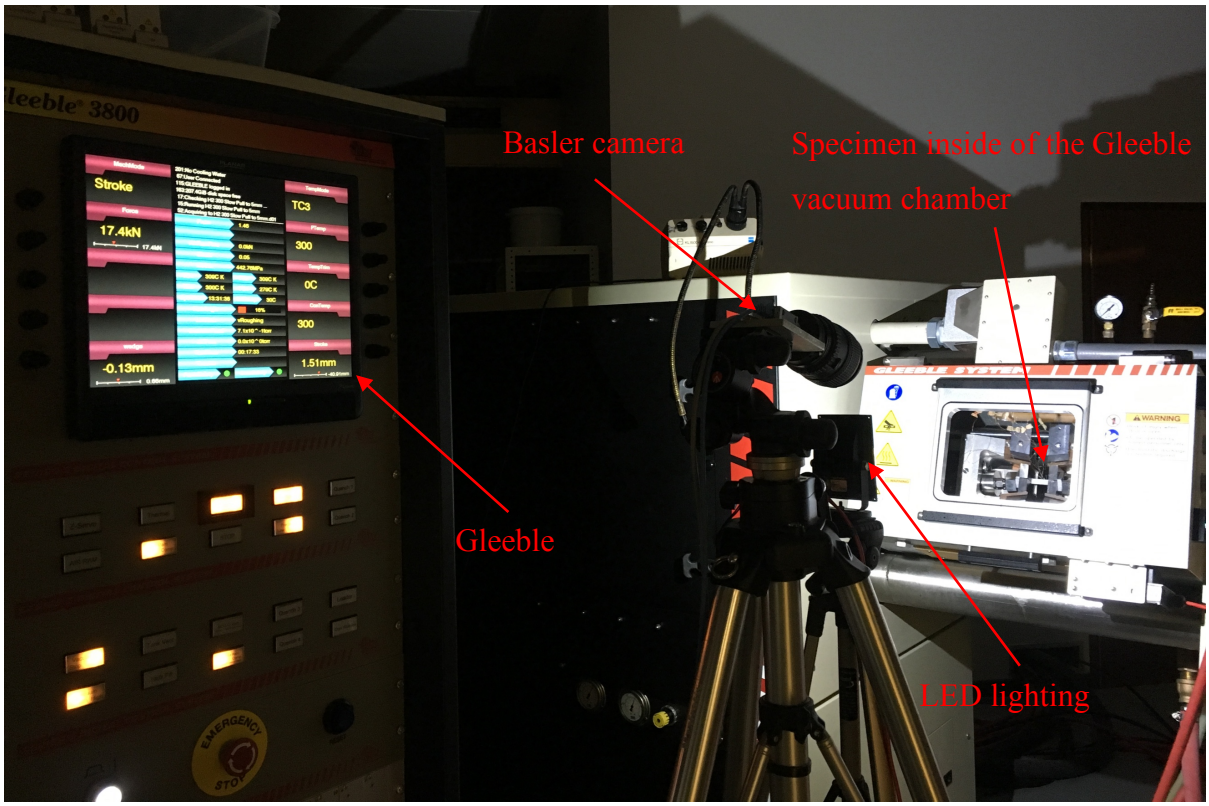

Figure 3.5.2-1: Set-up of the DIC equipment in relation to the Gleeble system.

3.5.3 CALIBRATION OF THE DIC SYSTEM

To provide confidence in the deformation results from the DIC system, an in-plane strain calibration process was conducted. The pixel dimensions need to be translated to Cartesian coordinates in order to obtain displacement data. The calibration process allowed the camera's imaging parameters to be determined and processed by the DIC software. In theory, the calibration process should aim to determine two parameters: intrinsic parameter – such as focal length and principal point of the lens; and extrinsic parameters – such as translation vectors and rotational matrix [49], [64].

In order to determine these calibration parameters, a Dantec Dynamics 9 x 9, 40 millimetre ceramic target was used. Due to the orientation of the specimen inside the Gleeble chamber, a Perspex block was machined to the exact angle to coincide with the tensile specimen orientation. The calibration target was secured onto the Perspex block and was then placed inside of the Gleeble vacuum chamber. Image calibration was conducted with the Gleeble viewing window closed and prior to any experiments. Before calibration, the cameras' position, aperture, focus and light settings were adjusted in order to maximise the clarity of the calibration target. A sequence of seven to ten images of the calibration target was then acquired each time the position of the calibration target was changed by tilting it to different angles, and by translating it in different directions. The adequate spacing between the DIC system and the Gleeble chamber door allowed for the chamber door to be opened and closed to move the position of the calibration target without having to disturb the DIC system. Figure 3.5.3-1 illustrates a series of images of the calibration target at different orientations.

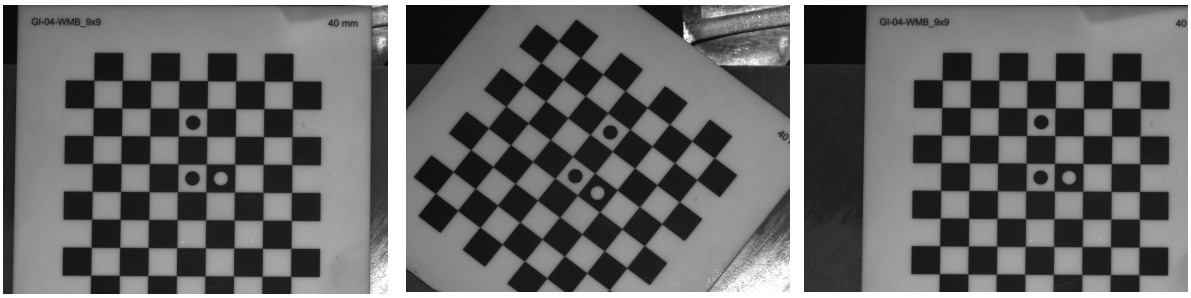

Figure 3.5.3-1: Photographs of the calibration target at different orientations within the Gleeble chamber.

Following calibration, the DIC Dantec Dynamics software was initiated and the calibration images were loaded and processed to detect and correlate the calibration target pattern, a calibration constant of 80 % was used as a threshold. Figure 3.5.3-2 illustrates a tesnsile specimen within the Gleeble vacuum chamber.

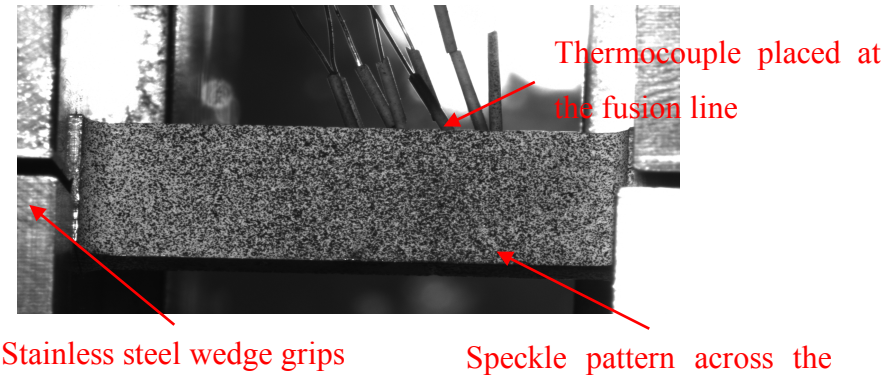

Figure 3.5.3-2: Image of the tensile specimen post image calibration.

3.5.4 POST PROCESSING OF DIC IMAGES

DIC operates by processing a correlation algorithm to track the position of the same physical points shown in a reference image and a deformed image. The DIC software used in this study was ISTRA 4D from Dantec Dynamics.

Once an experiment was complete, the subsequent captured images which were captured in grey scale were uploaded onto the DIC software. The post processing process began with masking of the region of interest (ROI) and choosing a seeding point; the seeding point was chosen around a well-defined speckle. The DIC software was then run and the seeding point defined in the reference image was then located in all subsequent deformed images. Figure 3.5.4-1 illustrates the masked ROI and the seeding point.

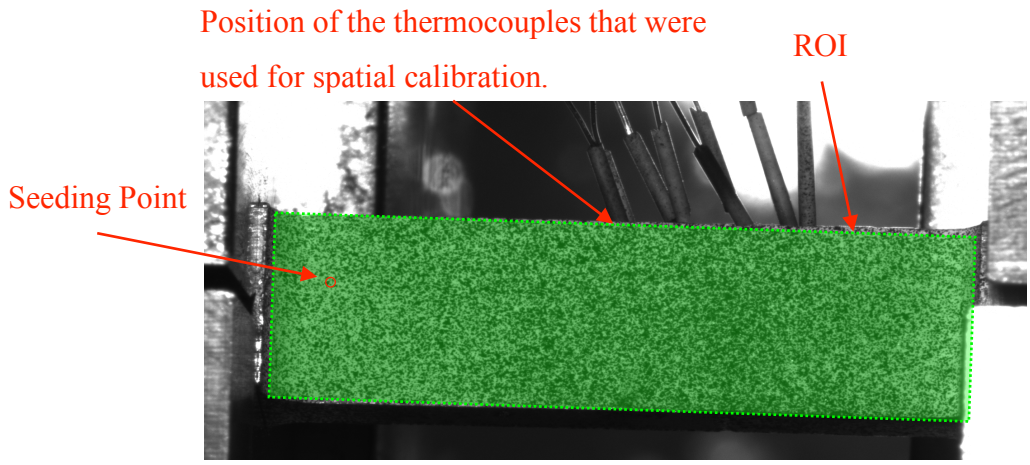

Figure 3.5.4-1: Illustration of the DIC post processing process.

In order to track the movement of pixels from the reference image and their subsequent location determined on the deformed image, a square subset of pixels on the speckle pattern was defined. This subset of pixels was termed a facet, and the overlap between subsets was termed grid spacing. Determination of the facet size and grid spacing size was based on the strain resolution required to detect pixel displacements. Initially a facet and grid spacing size of 29 (~ 0.6 millimetres) and 19 (~ 0.3 millimetres) pixels was respectively used. This was subsequently evaluated and refined to 19 (~0.3 millimetres) and 9 (~0.2 millimetres) pixels respectively.

3.6 SYNCHRONISATION OF THE DIC TO GLEEBLE OUTPUTS

By combining displacement data from the DIC system with temperature, strain and force data from the Gleeble, insight of mechanical and material properties across a weld zone can be gained. However, in order to achieve this, synchronisation of the two independent data sets was needed. This section outlines the procedures followed to align both the DIC and Gleeble results before mapping the incremental strain localisation across a weld zone. Finally, the strain hardening coefficient for each of the weld zones is approximated.

3.6.1 COMPARISON OF THE DIC AND GLEEBLE STRAIN

Global strain measurements across the full gauge length were determined by extracting data from both the Gleeble as well as from the DIC system.

The Gleeble strain measurements were determined by the relative movement of the stroke, whilst the global strain from the DIC system was found by tracking the movement of defined points positioned on either end of the gauge length. Figure 3.6-1 illustrates the global machine strain across the specimen from both the Gleeble and DIC systems.

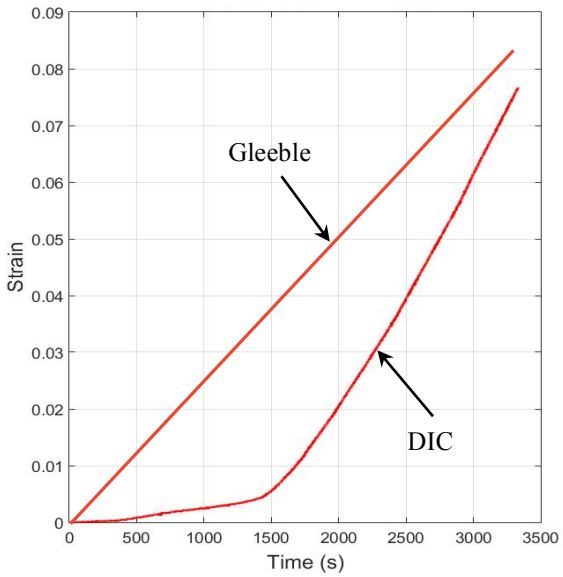

Figure 3.6-1: Global strain comparisons determined by extracting data from both the Gleeble and the DIC system.

The Gleeble was programmed to extend the specimen at a constant strain rate of 50 $\mu\varepsilon.s^{-1}$; this was recorded by measuring the cross head speed of the stroke. The Gleeble strain was found to be a diagonal straight strain-time graph passing through the origin, as illustrated in Figure 3.6-1. Strain from the DIC system was measured by evaluating the relative displacement of pixels. Strain from the DIC system did not follow same the straight line trend as the strain recorded by the Gleeble; an almost bilinear strain-time relationship was noticed. The strain data from the DIC was a true reflection of gauge strain for two primary reasons. Firstly, it captured the actual trilinear material behaviour as the specimen was. And secondly, the artificial strain due to the influences of non-specimen's displacement was not experienced.

The fundamental difference between the strain-time graphs for both the Gleeble and DIC is due to machine compliance. The phenomenon of machine compliance is defined as the nonlinear displacement within the loading system which arises from the nonlinearity associated with the many connections and/or linkages present within the loading system [65]. The area bound in between the two graphs in Figure 3.6-1 was the machine compliance of the Gleeble. Within the Gleeble, machine compliance would have arisen from a number of sources such as due to lubricant squeezing out of junctions, self-alignment of the pocket jaws and wedge grips, and inherent stretching of the individual components. The inaccuracies due to machine compliance illustrated the noncontact strain measurement benefits of DIC.

3.6.2 ALIGNMENT OF THE GLEEBLE AND DIC DATA

In this study the synchronising of the Gleeble and DIC data was done manually. After the DIC system was calibrated and the Gleeble chamber was placed under vacuum, the DIC program script and the DIC image recording software were manually started. As previously discussed, the Gleeble was first programmed to heat the specimen to the desired target temperature before extending the specimen. During the heating period a preload was applied to the specimen. The preload served two primary functions; firstly, to ensure that there was sufficient contact between the pocket jaws and specimen for direct resistance joule heating, and secondly to introduce a strain artefact that could be used to synchronise the DIC and Gleeble data.

The outputs from these two systems were synchronised by generating strain-time plots for each of the two systems. The Gleeble crosshead displacement was compared to the linear

displacement recorded by the DIC system. Using the strain artefact as a reference, an adjusted time stamp was determined by comparing the delay between the points. Using this time stamp, DIC obtained displacements were adjusted to match the Gleeble times. Figure 3.6.2-1 illustrates the DIC adjusted time stamp.

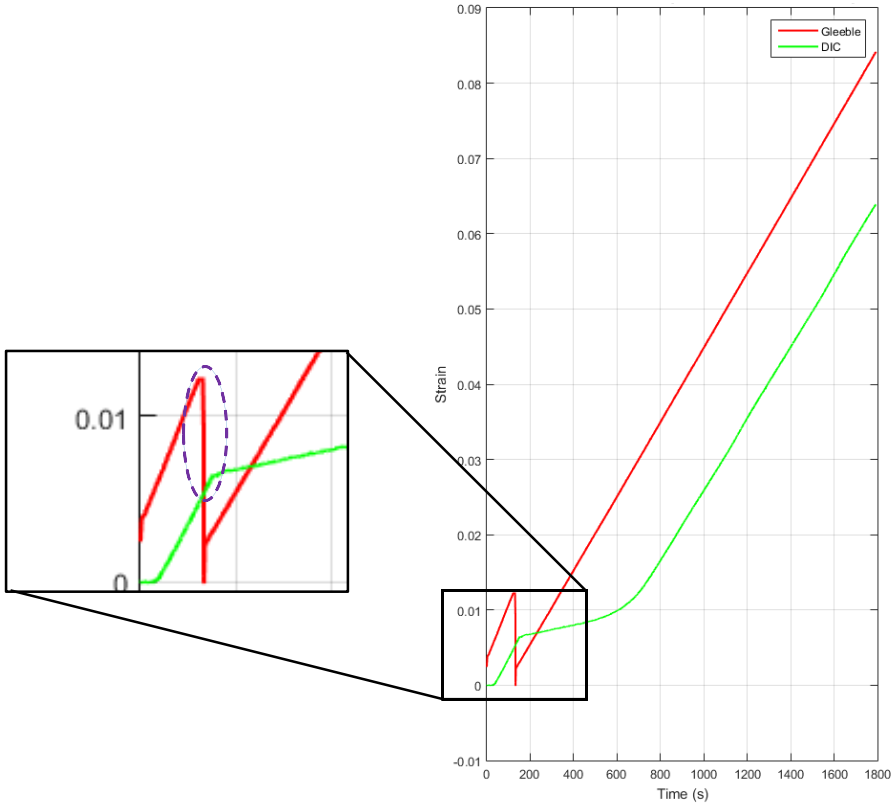

Figure 3.6.2-1: Synchronising the DIC and Gleeble data using a displacement time stamp.

3.6.3 GAUGE LENGTH STRAIN DISTRIBUTION

In order to validate if the Gleeble and DIC system setups, as well as the post processing techniques were adequate to detect strain localisation across a weld zone, a tensile specimen with a weld located along its gauge length was tested at three different temperatures (RT, 300 ^{o}C and 535 ^{o}C) at a constant strain rate of 50 $\mu\varepsilon.s^{-1}$.

By combining displacement, time, temperature and force data, strain localisation curves spanning across the specimen's gauge length were mapped. Pixel displacements were converted to the first Lagrangian principle gauge strain data by the DIC post processing software. The gauge strain, which is analogous to an extensometer positioned on the centre line across the specimen, was simulated across the entire gauge length.

In particular, strain was extracted at three different points during the tensile test. These points were just after yielding (YS), at the ultimate tensile stress (UTS), and at the end of the experiment. These three points were selected in order to gain a more holistic view of the influence of temperature on the material and mechanical properties of the weld. The YS and UTS were determined from the stress-strain curves at each of the testing temperature; illustrated in Figure 4.2-1. The YS was determined by the conventional 0.2 % strain off-set method and the UTS was determined by the maximum stress before necking occurred. A Matlab script was used to automatically determine the strain at which the YS the UTS occurred, using the strain the time at which the YS and UTS occurred was determined from the stress-strain curves (Figure 4.3.1-1 and Figure 4.4.1-1). The end of the test observation point was defined as the time at which the test for each of the testing temperatures was concluded. The strain distributions across the specimen's gauge length are illustrated in Figure 3.6.3-1.

The gauge strain just after the yield point, illustrated by the magenta strain curve, for each of the three temperatures illustrated that the entire weldment strained uniformly at a very low value of strain. At yielding, the variation in strain across the different weld zones was not noticeable. In contrast, at UTS, indicated by the green strain curve, it was distinctly noticeable that the strain distribution was not uniform due to the presence of the heterogeneous weld. The variation in strain across the different weld zones at UTS were more apparent. Subsequently the strain distribution at the end of the experiment, illustrated by the red strain curve, had a

similar strain profile as that of the strain distribution at UTS; with the only difference being that at the end of the experiment there was an overall larger accumulation of strain. According to the strain DIC gauge strain distributions, necking which resulted due to an accumulation of strain, was observed to have occurred at different regions of the weld. The necked location was confirmed by visually inspecting the specimen after each test. The thermal distribution at each of the experimental temperatures is illustrated by the blue circular indicators in Figure 3.6.3-1 (a) – (c).

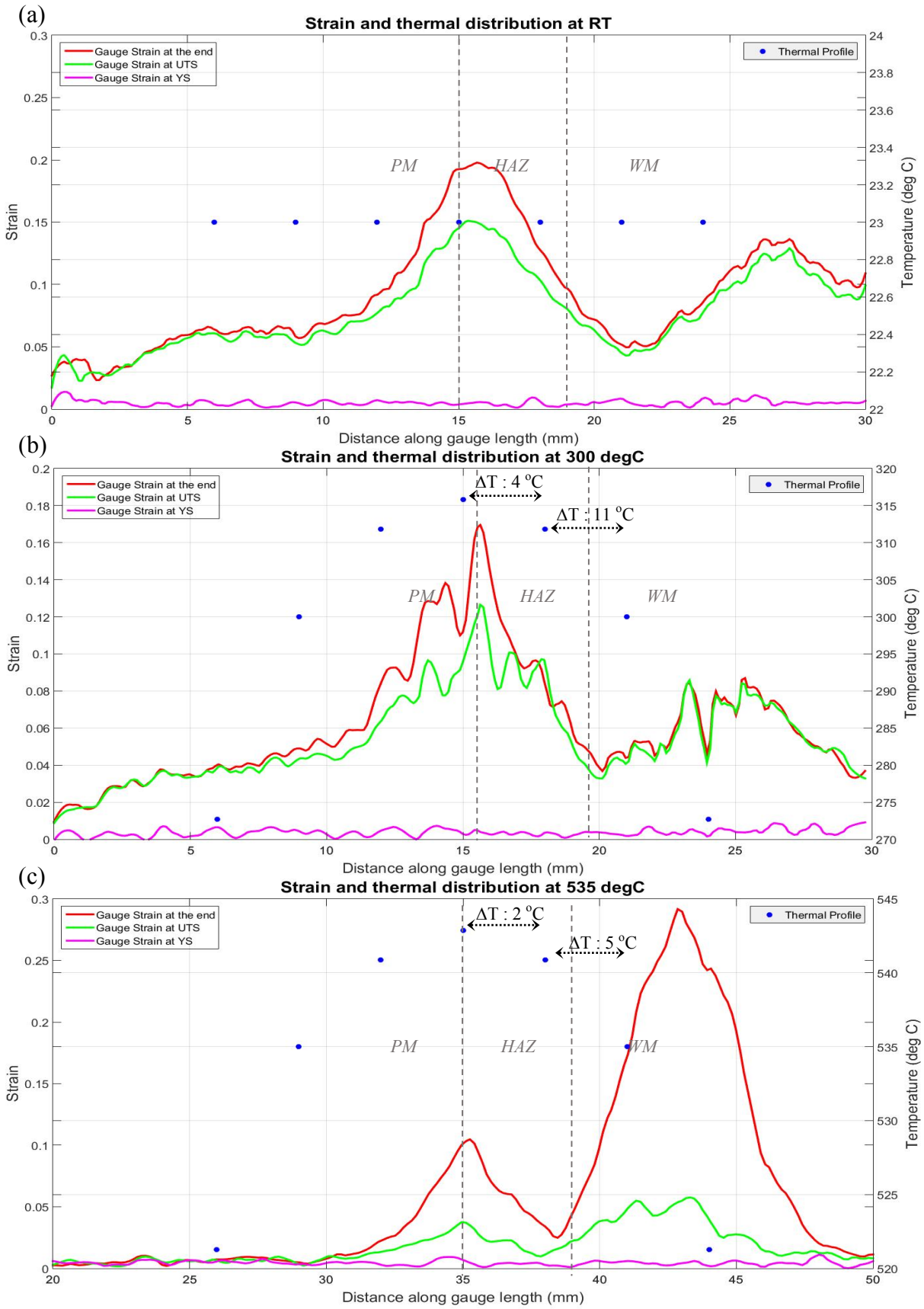

Figure 3.6.3-1: The strain distributions and thermal profiles across a weld zone at (a) RT, (b) 300 °C and (c) 535 °C.

3.6.4 INCREMENTAL TEMPORAL STRAIN

In order to attain a more detailed understanding of the strain distribution across the HAZ, a microscale strain analysis of the HAZ was conducted. This was done by simulating virtual strain gauges of one millimetre in length at intervals of one millimetre, covering a total distance of six millimetres. The first one millimetre increment commenced at the FL and progressively moved through the CGHAZ, FGHAZ, and into the parent material. The virtual strain gauges were spatially calibrated using the position of the thermocouples that were captured by the DIC system. Figure 3.6.4-1 illustrates the location of each virtual strain gauge with their respective colour indicators.

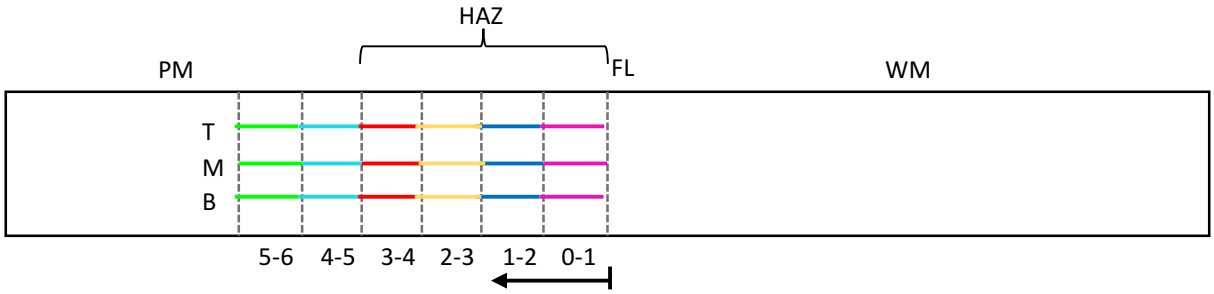

Figure 3.6.4-1: Schematic illustration the location of the localised virtual strain gauges.

Initially virtual strain gauges were simulated at three different positions across the gauge length; from the top (T), middle (M) and (B) bottom of the specimen. However, after analysing the DIC strain distribution between these three positions it was found that there was very little strain variation. The differences in strains taken from these three positions suggested that there was some degree of axial rotation and/or bending of the specimen during the test. These effects could be negated by exercising extra precaution when aligning the specimen within the wedge grips, and by ensuring that the Gleeble locknuts were adequately tightened. With this in mind, the middle (M) of the specimen was chosen as the ideal location, as it was considered that the influences of axial misalignment and/or bending would be least significant at this location. In order to ensure that all experiments were analysed at the same location, a reference point was lightly scribed onto the front face of the specimen along the centre line and was used as a reference feature for spatial calibration for subsequent tests. Figure 3.6.4-2 illustrates the incremental temporal strain across the weld zone at each of the three experimental temperatures.

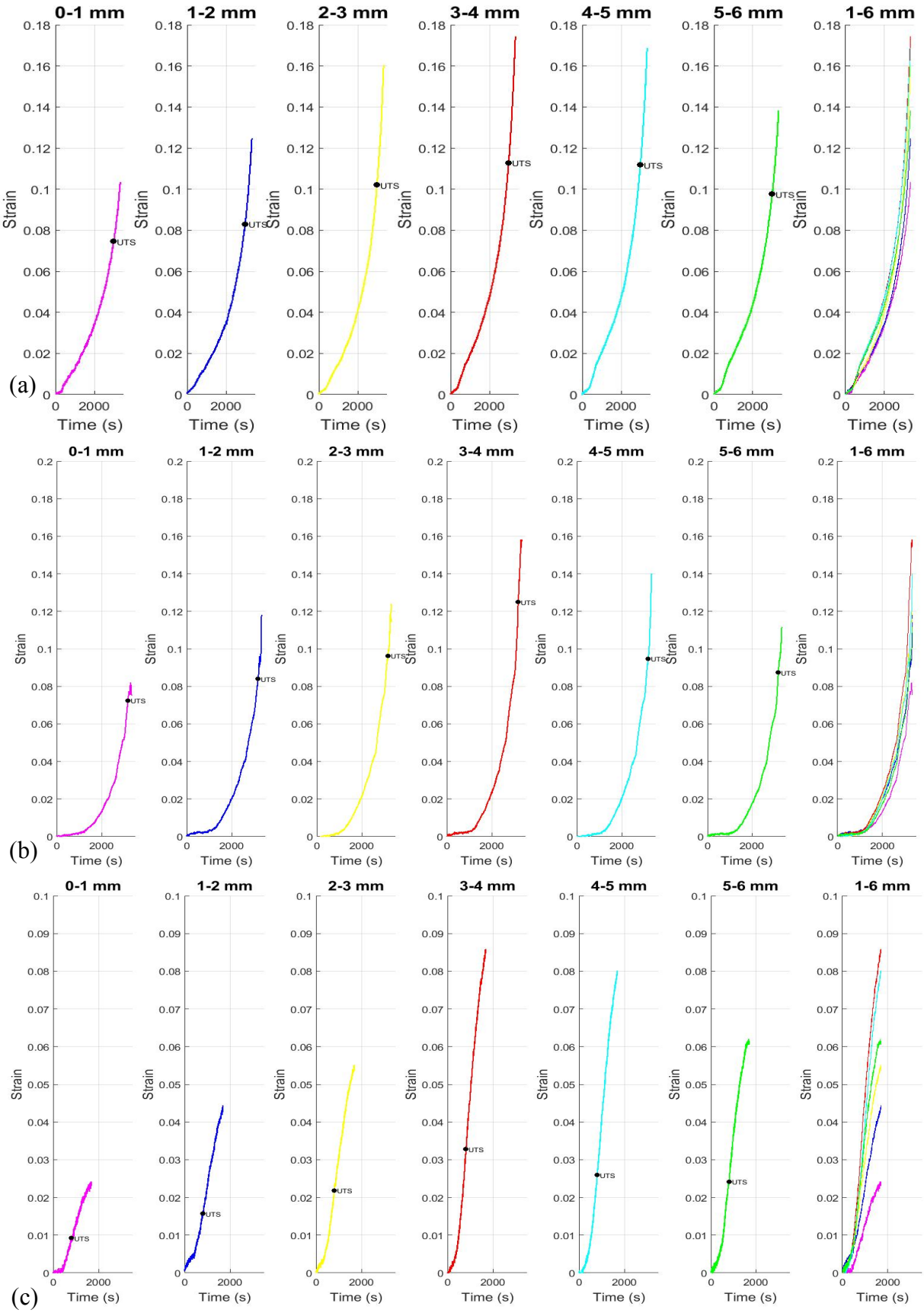

Figure 3.6.4-2: Incremental temporal strain across the weld zone at (a) RT, (b) 300 ^{o}C and (c) 535 ^{o}C

At RT, illustrated by Figure 3.6.4-2 (a), the FL (first incremental gauge line) experienced the lowest strain, and values of strain accumulation increased from the weld material towards the parent material. The fourth incremental gauge line illustrated the largest accumulation of strain and suggested that the HAZ closest to the parent material, which was the FHGAZ was the weakest zone as it had strained the most relative to the other weld zones. Similarly the experiment at 300 ^{o}C, illustrated by Figure 3.6.4-2 (b), showed a similar trend with the exception that there was a lower accumulation of strain. For the experiment at 535 ^{o}C, illustrated by Figure 3.6.4-2 (c), there was a much lower peak strain compared to the experiments at RT and 300 ^{o}C; this was primarily due to the location at which necking occurred.

3.6.5 INCREMENTAL STRESS-STRAIN AND WORK HARDENING EXPONENT

By combining load data from the Gleeble system with displacement data from the DIC system, incremental stress-strain curves were generated.

The force data from the Gleeble's load cell was divided by the original cross sectional area of the gauge length and subsequently the incremental engineering stress was determined. This was coupled with the incremental engineering strain outlined in section 0. The engineering stress-strain curves for each of the experimental temperatures are illustrated in Figure 3.6.5-1. The strain accumulation from the FL (first incremental gauge line) towards the FGHAZ (fourth incremental gauge line) was once again observed.

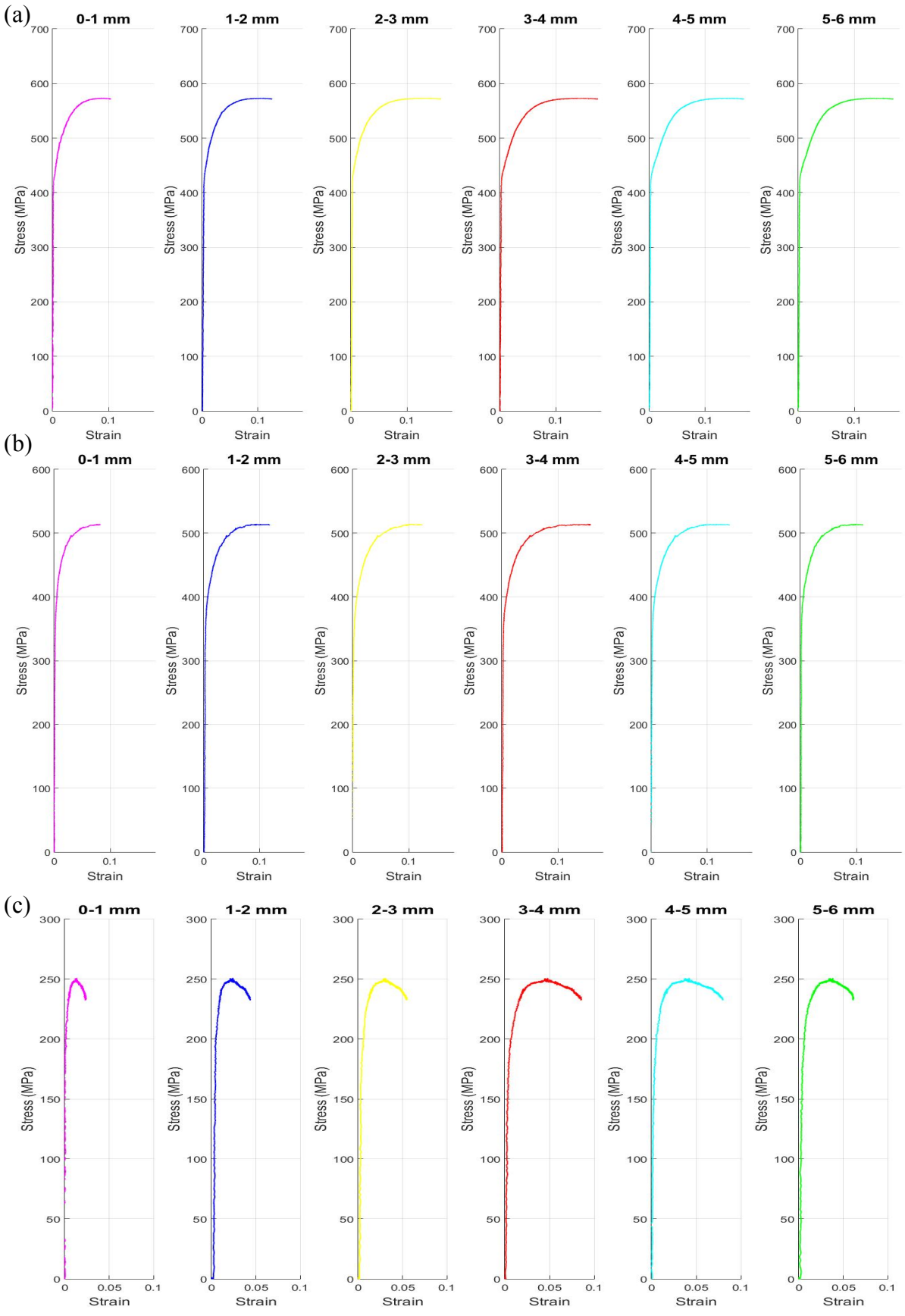

Figure 3.6.5-1: Incremental stress-strain curves at (a) RT, (b) 300 ^{o}C and (c) 535 ^{o}C

A useful material property that can be determined from these incremental stress-strain curves is the strain hardening coefficient. Strain hardening is the strengthening of a material by plastic deformation which occurs due to the nucleation and motion of dislocations [66]. The strain hardening coefficient can be determined using the Hollomon strain hardening equation [67]:

$$\sigma_t = K \cdot {\varepsilon_t}^n \qquad \text{Equation 3.6.5-1}$$

where: σ_t is the true stress in MPa, K is a material constant, ε_t is the true strain and n is the strain hardening coefficient.

The strain hardening coefficient 'n' gives quantitative measurement of the strain hardening characteristic of a material. The strain hardening coefficient is approximated using the true stress versus true strain relationship during plastic deformation [66], [68].

The strain hardening exponent can be approximated across each of the weld zones by converting the incremental stress-strain curves in Figure 3.6.5-1 into incremental true stress – true strain curves. This was achieved using the following formulae to convert engineering stress and strain to true stress and true strain.

$$\sigma_t = \sigma_e \cdot (1 + \varepsilon_e) \qquad \text{Equation 3.6.5-2}$$

$$\varepsilon_t = ln(1 + \varepsilon_e) \qquad \text{Equation 3.6.5-3}$$

where: σ_t is the true stress in MPa, σ_e is the engineering stress in MPa, ε_e is the engineering strain, and ε_t is the true strain.

Figure 3.6.5-2 (a) illustrates the true stress – true strain for a RT experiment. As strain hardening is the strengthening of a material by plastic deformation, the strain hardening exponent can only be determined from the plastic region of the true stress – true strain curves. In addition, flow stress equations (3.7.5-2 and 3.7.5-3) are also only valid before UTS, and thus the strain hardening coefficient can only be determined from the point of yielding to the point of necking/UTS. Figure 3.6.5-2 (b) illustrates the region of the true stress – true strain curves that were used to approximate the strain hardening coefficient.

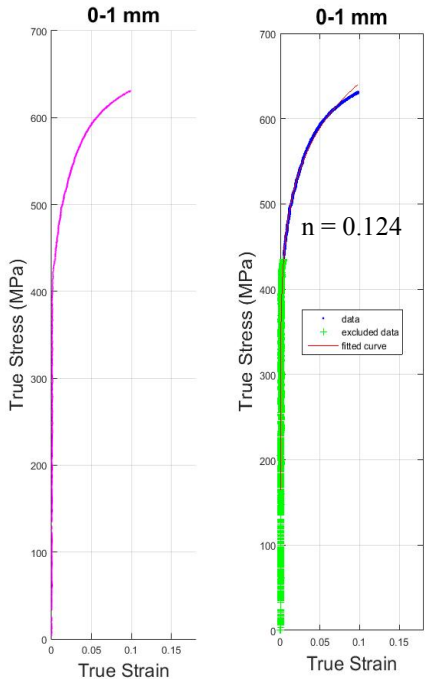

Figure 3.6.5-2: (a) True stress - true strain curve for a RT tensile test (b) True stress - true strain curve illustrating the region used to approximate the strain hardening coefficient.

The strain hardening coefficient was determined by first curve fitting the plastic region of the true stress versus true strain curve, and then approximating the curve fit using a power equation of the from $y = a \cdot x^b$. The strain hardening coefficient was automated by generating a Matlab script, and is illustrated in Figure 3.6.5-2 (b).

Due to the varying temperature field varying material attributes are present in the sample. Material property extraction across the gauge length is largely dependent on the sample geometry and the assumed stress state. The width of the specimen brings into question the comparison of plane stress and uniaxial stress. In an attempt to measure the stress state of a reduced section tensile specimen, Melody et al. quantified the triaxiality factor across the specimen's gauge length. Figure 3.6.5-3 illustrates the stress triaxlity ratio distribution along one half of the gauge length [69].

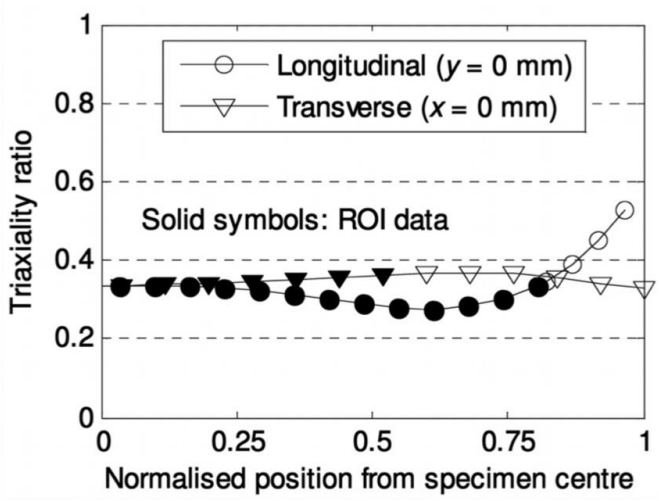

Figure 3.6.5-3: Triaxiality ratio along half of the gauge length [69].

The stress traixiality ratio varied from the centre of the specimen toward the edges. This implied that the reduced geometry gauge length is not suitable for material property extraction across the entire gauge length [69]. However, the stress traixiality ratio was approximately 0.33 (posions ratio) towards the centre of the specimen which implied that the due to the HAZ being positioned at the centre of the gauge length, a uniaxial stress state could be assumed when extracting material properties from the region of the HAZ.

4 APPLICATION OF THE EXPERIMENTAL TECHNIQUE

In order to validate if the developed experimental technique was capable of detecting localised strain across a weld zone at elevated temperatures, two welds which were exposed to different operating conditions were used for validation. The experimental outcomes of the high temperature tensile tests conducted on the steam penetration, turbine housing weld (THW) and, loop pipe weld (LPW) are presented in this chapter.

4.1 MATERIAL BACKGROUND AND EXPERIMENTAL MATRIX

High temperature tensile tests were conducted at RT, 300 ^{o}C and 535 ^{o}C. In addition, the weld parent material was also used for experimental investigation, and served as a material reference. Table 4.1-2 outlines the experimental matrix followed. Tensile specimens were machined from each of the welds using the specimen geometry detailed in sections 3.2.

Table 4.1-1: Validation experimental matrix.

Material	Specimen Type	Strain Rate	Temperature (^{o}C)
Loop Pipe Weld (LPW)	Short Specimen, with 6 mm holes	50 $\mu\varepsilon.s^{-1}$	RT (± 24)
	Short Specimen, with 6 mm holes		300
	Long Specimen, with 6 mm holes		535
Turbine Housing Weld (THW)	Short Specimen, with 6 mm holes	50 $\mu\varepsilon.s^{-1}$	RT (± 24)
	Short Specimen, with 6 mm holes		300
	Long Specimen, with 6 mm holes		535
Steam penetration material (SP)	Short Specimen, with 6 mm holes	50 $\mu\varepsilon.s^{-1}$	RT (± 24)
	Short Specimen, with 6 mm holes		300
	Long Specimen, with 6 mm holes		535

The component that was of interest to validate the application of the experimental technique was a turbine steam penetration. Steam penetrations are found in coal fired power stations and its primary function was to transport steam from the superheater (steam generation subsystem)

into the high pressure turbine casing (turbine subsystem). The steam from the superheater is transported at a super critical temperature and pressure of 535 ^{o}C and 16.1 MPa respectively [70].

The steam penetration was connected to the loop pipe and turbine housing by means of butt welds, as illustrated in Figure 4.1-1. Upstream, the steam penetration (SP) was welded to the loop pipe via the loop pipe weld (LPW) and downstream, the steam penetration (SP) was welded to the turbine housing case via the turbine housing weld (THW). Both the LPW and the THW were in service for the same amount of time (approximately 24 years).

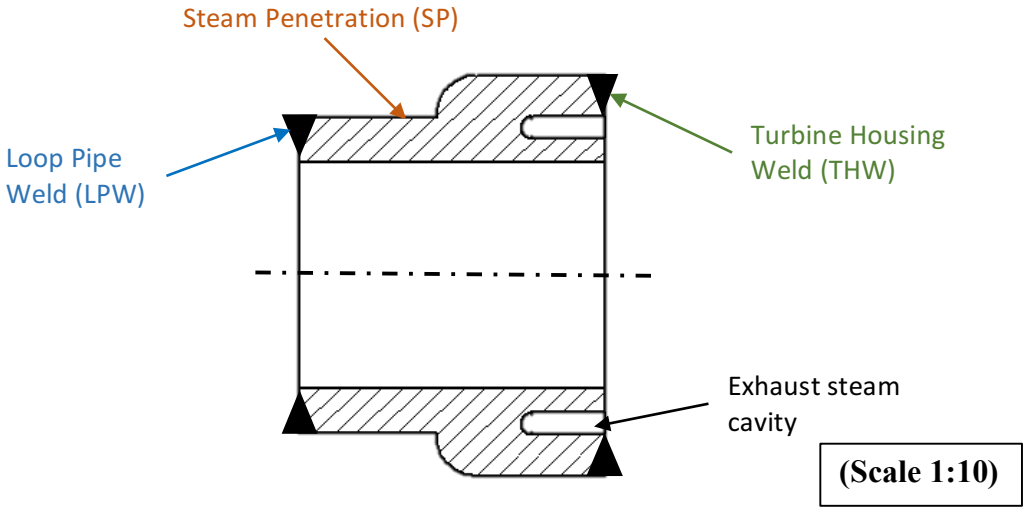

Figure 4.1-1: Cross-section of a steam penetration illustrating the location of the two

Due to the geometry of the steam penetration, the exhaust steam cavity located in the region of the THW would have resulted in the THW being less susceptible to extreme operating conditions when compared to the LPW. It is for this reason that the THW is believed to have undergone less material degradation, when compared to the LPW. The LPW had nominal operating conditions of 535 ^{o}C and 16.1 MPa, whilst the THW had nominal operating conditions of 332 ^{o}C and 4.1 MPa. The steam penetration was cast out of a creep resistant 21CrMoV57V alloyed steel. Table 4.1-2 tabulates the chemical composition of each weld filler material and for the steam penetration.

Table 4.1-2: Steam penetration's chemical composition by wt % [71]–[73].

	C	Si	Mn	P	S	Cr	Mo	Ni	Cu	Al	V	Fe
SP	0.236	0.262	0.655	0.018	0.008	1.330	0.691	0.093	0.129	0.033	0.265	96.038
THW	0.060	0.460	0.685	0.006	0.008	0.656	0.500	0.081	0.114	0.002	0.248	97.05
LPW	0.085	0.322	0.919	0.013	0.01	0.464	0.947	0.026	0.027	0.004	0.477	96.58

4.2 STRESS-STRAIN BEHAVIOUR OF THE WELD MATERIALS AT VARIOUS TEMPERATURES

In general, a welded joint is in nature a composite material, comprising of different materials making up the different weld segments. Both the THW, and LPW are considered as dissimilar welds, as both the parent material and the weld filler material are different.

One of the first experiments that were conducted, were tensile tests at various temperatures of the parent and weld materials; which is the steam penetration (SP), the turbine housing weld, and the loop pipe weld. Figure 4.2-1 illustrates the material behaviour of the SP, THW and the LPW at RT, 300 ^{o}C and 535 ^{o}C. The engineering stress-strain curves in Figure 4.2-1 were derived by dividing the Gleeble load cell value by the original cross-sectional area. The strain values were obtained from the DIC analysis, by simulating a gauge strain line across the gauge length (in other words the strain value is the accumulative strain along the gauge length).

From Figure 4.2-1 it was observed that the material behaviour of these three materials at RT was very similar. The SP displayed to have a higher yield (YS) and ultimate tensile strength (UTS) than both the THW and the LPW, whilst the THW and the LPW had almost identical YS and UTS. The dissimilar gradients observed in the elastic region was most likely due to the variable machine compliance. At the 300 ^{o}C, the LPW proved to have higher strength and elongation properties than the THW. This behaviour at 300 ^{o}C was peculiar, as it was expected that the LPW would be weaker than the THW due to the increase in temperature. It must also be noted that at 535 ^{o}C the SP specimen strained to a maximum of 0.064, whilst both the THW and the LPW specimens fractured at approximately halfway into the experiment at strains of 0.03 and 0.028 respectively.

(a)

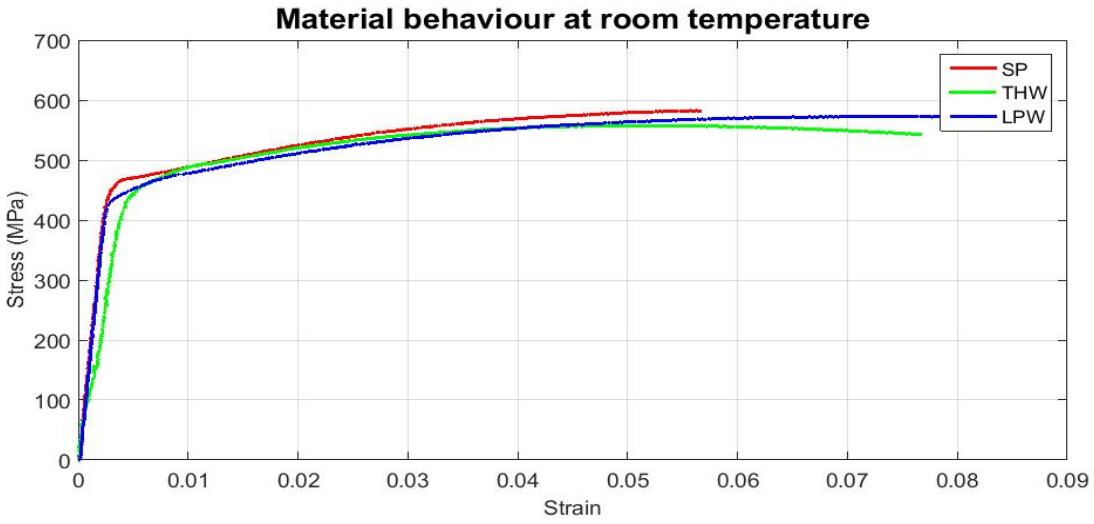

(b)

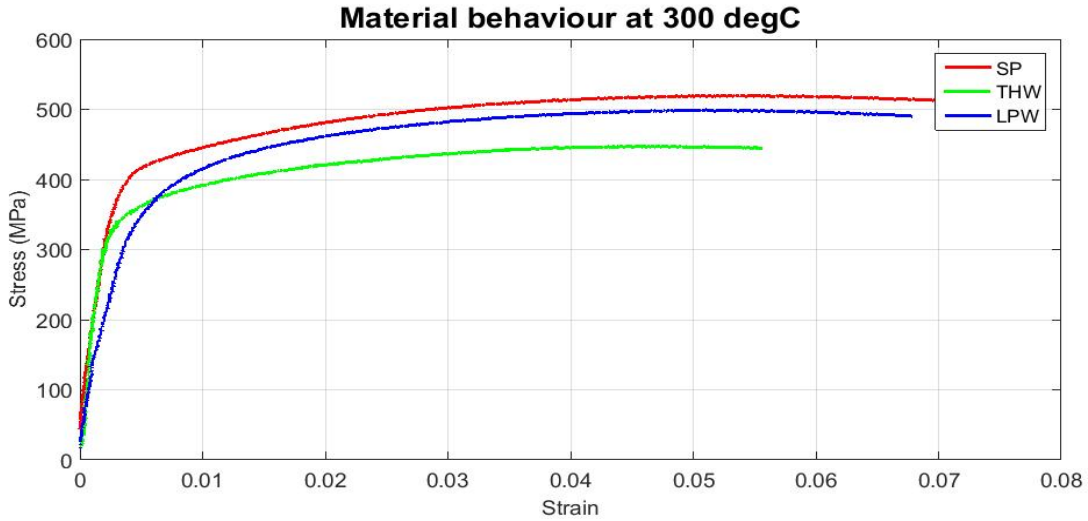

(c)

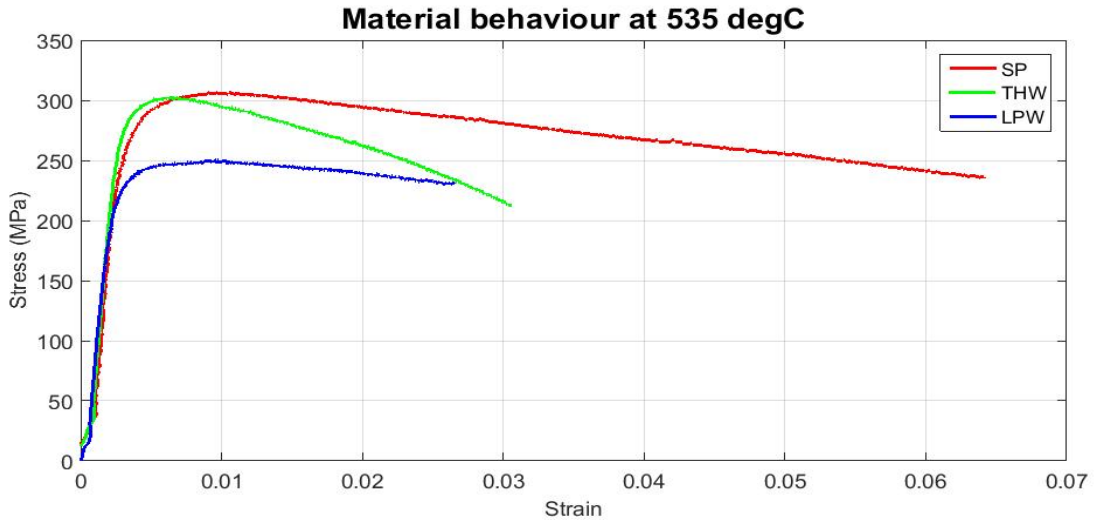

Figure 4.2-1: Stress strain curves of the parent and different weld materials at (a) RT, (b) 300 ^{o}C and (c) 535 ^{o}C.

4.3 LOOP PIPE WELD

As was outlined in section 4.2, there were three different temperatures (RT, 300 ^{o}C, and 535 ^{o}C) of interest that experiments were conducted at. In this section the experimental results will be presented for the loop pipe weld, first on a macro scale, and then on a micro scale where the latter examines the strain localisation across the weld.

Tensile tests were conducted at room temperature and at elevated temperatures at a strain rate of 50 $\mu\varepsilon.s^{-1}$.To gain experimental confidence each type of experiment was repeated once; the repeat experiments can be found in Appendix 8.4.

4.3.1 MACRO SCALE STRAIN DISTRIBUTION

The total (accumulative) gauge strain was measured across the gauge length for each of the three experiment temperatures, and is illustrated in Figure 4.3.1-1. The preload and heating (thermal expansion) segments of the experiments were removed, and only the segments from when the specimen started to be extended at temperature are illustrated in these graphs.

In view of the fact that the Gleeble was programmed to extended the specimen at a constant strain rate, it was expected that the strain-time graph would be a straight diagonal line passing through the origin. However, taking into account machine compliance and the actual material behaviour, an almost bilinear strain-time plot was seen. This bilinear trend was most prominent for the experiments at RT and 300 ^{o}C. It was also observed that the strain rate at the end of the experiment was the highest at RT, and gradually decreased as the temperature was increased.

The global (or total) strain-time graph was analysed in two separate segments. In the first segment, A-B, initially the strain remained at zero for approximately five minutes into the experiment, thereafter the specimen strained at a constant rate up until the yield strength (YS). Subsequently in segment B-C the specimen was found to have strained at a much faster strain rate. The trilinear strain rates observed in segments A-B and B-C are as a result of machine compliance which was a result of slippage or take up within the Gleeble system, and was found to be most significant in segment A-B which was the elastic region.

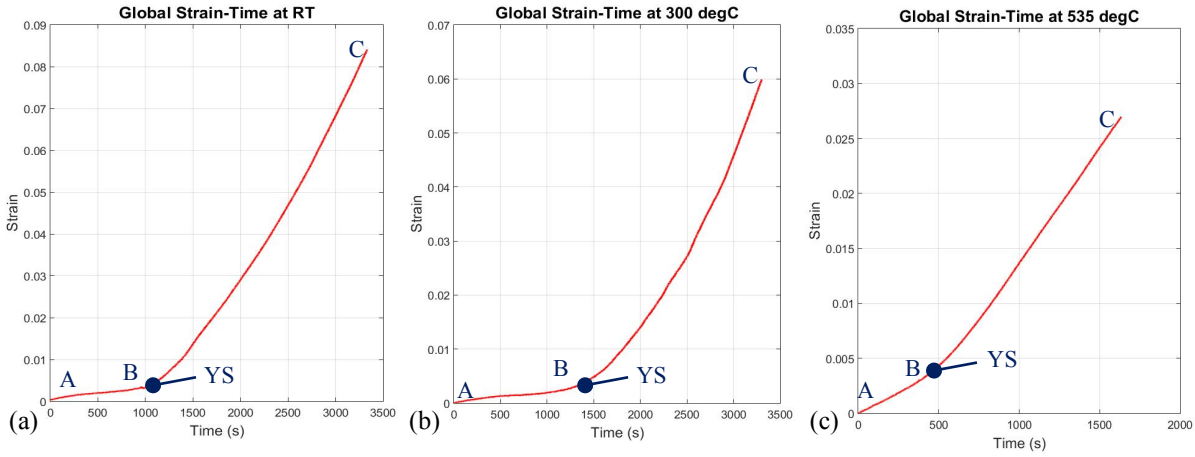

Figure 4.3.1-1: Global strain-time curves of the LPW at (a) RT, (b) 300 ^{o}C and (c) 535 ^{o}C

In order to attain more informative strain behaviour, the first Lagrangian principle strain was extracted at three different points during the tensile experiment. These points were just after yielding (YS), at the ultimate tensile stress (UTS), and at the end of the experiment. The YS and UTS were defined by referring to the stress-strain curves (Figure 4.2-1) and extrapolating the time at which the YS and UTS occurred.

Figure 4.3.1-2 illustrates the strain distribution across the gauge length for each of the three experimental temperatures. The blue circular indicators illustrate the temperature distribution across the specimen's gauge length.

On analysis of the strain distribution across the gauge length at each of the three points of interest, the largest accumulation of strain for the RT and 300 ^{o}C experiments was found to have occurred in the region of the HAZ, whilst for the 535 ^{o}C experiment the largest accumulation of strain was found to be in the weld material. It was also distinctly noticeable was that there was a rise and fall in strain moving from the weld material and across the HAZ.

For each of these experiments the largest accumulation of strain recorded by the DIC software corresponded to the physical location at which necking occurred. In each of the three experiments, the strain distributions just after yielding (magenta curve) remained minimal, whilst the strain distribution at UTS (green curve) mimicked the strain distribution at the end of the experiment but to a less extent. This is expected behaviour as would be observed in a conventional tensile test.

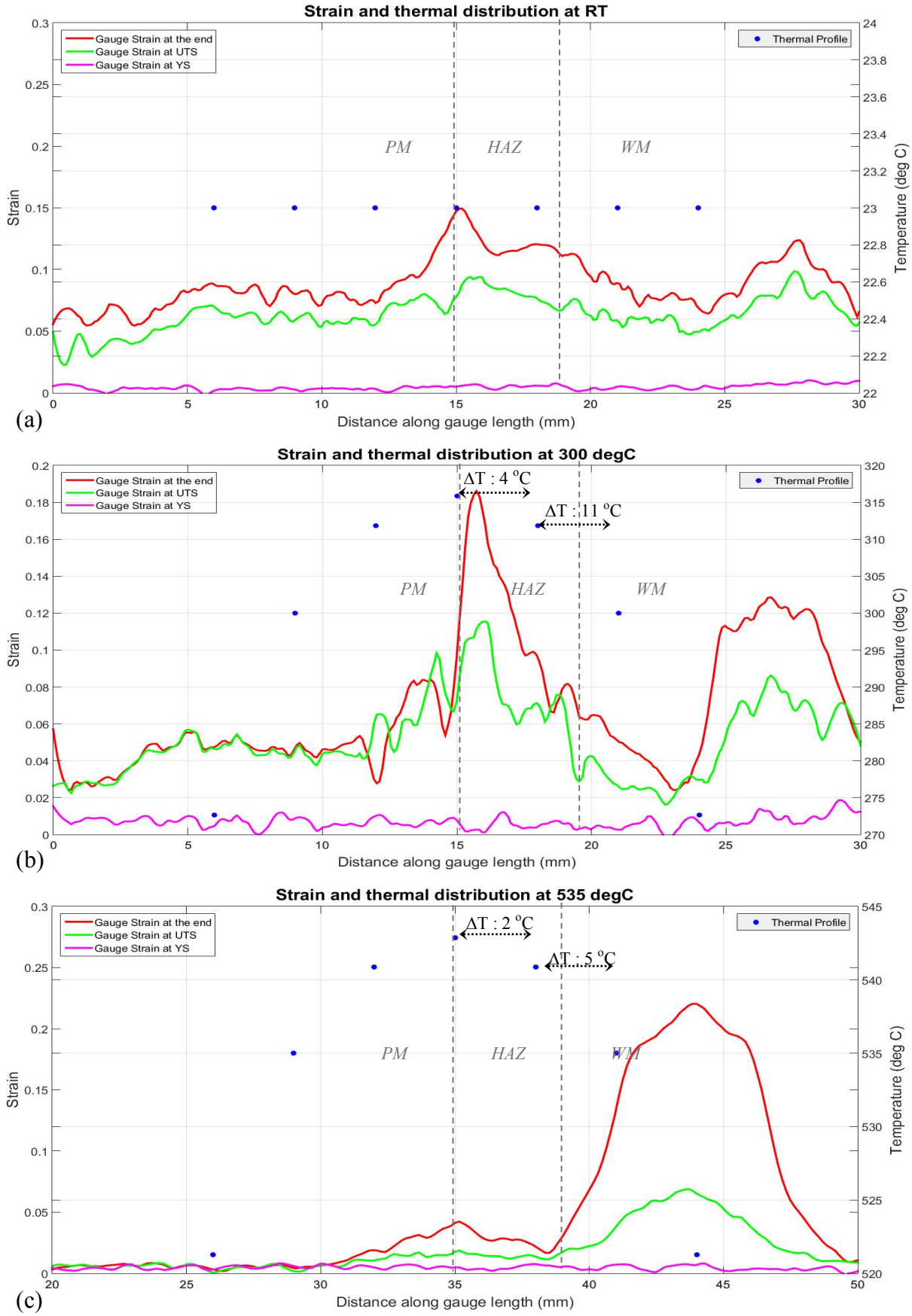

Figure 4.3.1-2: Strain and thermal distribution across the LPW gauge length at (a) RT, (b) 300 °C and (c) 535 °C.

4.3.2 LOCALISED STRAIN DISTRIBUTION

The localised strain distribution across the HAZ at the end of each experiment are illustrated in Figure 4.3.2-1.

For each of the experimental temperatures the incremental strain distribution was found to be trilinear. The initial segment saw the gradual linear-elastic increase in strain. In this segment the specimen was most resistant to elastic deformation which subsequently resulted in elastic deformation in the form of slack occurring thought the Gleeble's load train. Given that the Gleeble's crosshead speed was more or less constant the strain rate in this region was the lowest. The second segment which commenced once yielding had occurred saw a gradual increase in the strain rate. This observation was due to the reduction in specimen's cross sectional area which saw plastic deformation occurring only in the specimen's gauge; thus the strain rate between yielding and UTS was more or less constant. The third segment saw a further increase in the strain rate. Post UTS necking occurred, this saw a further reduction in the specimen's cross sectional area, and as a result the strain rate increased again.

At end of the 535 ^{o}C test a short plateau of strain that can be observed. In this segment strain across the HAZ remained constant, indicating that a larger accumulation of strain occurred in another part of the weld. This finding was supported by Figure 4.3.1-2 (c), where it was observed that between UTS and the end of the experiment, there was a gross accumulation of strain in the weld material. The ability to detect the change in strain behaviour for each of the experimental temperatures due to the material behaviour at evaluated temperatures is testament to experimental technique and post evaluation procedure followed.

Observing the strain distribution on a micro scale across the HAZ illustrated in more detail the rise and fall of strain across the HAZ. In each of the three experimental temperatures illustrated in Figure 4.3.2-1, it was observed that there was a gradual increase and then decrease in strain moving from the fusion line into the parent material. In each of the experiments, the maximum accumulation of strain was observed at the end of the HAZ (fourth incremental gauge line). This finding further confirmed that the HAZ nearest to the parent material; which was the FGHAZ was the weakest zone as it had strained the most relative to the other zones. The trend of increasing strain till the FGHAZ was also observed at UTS.

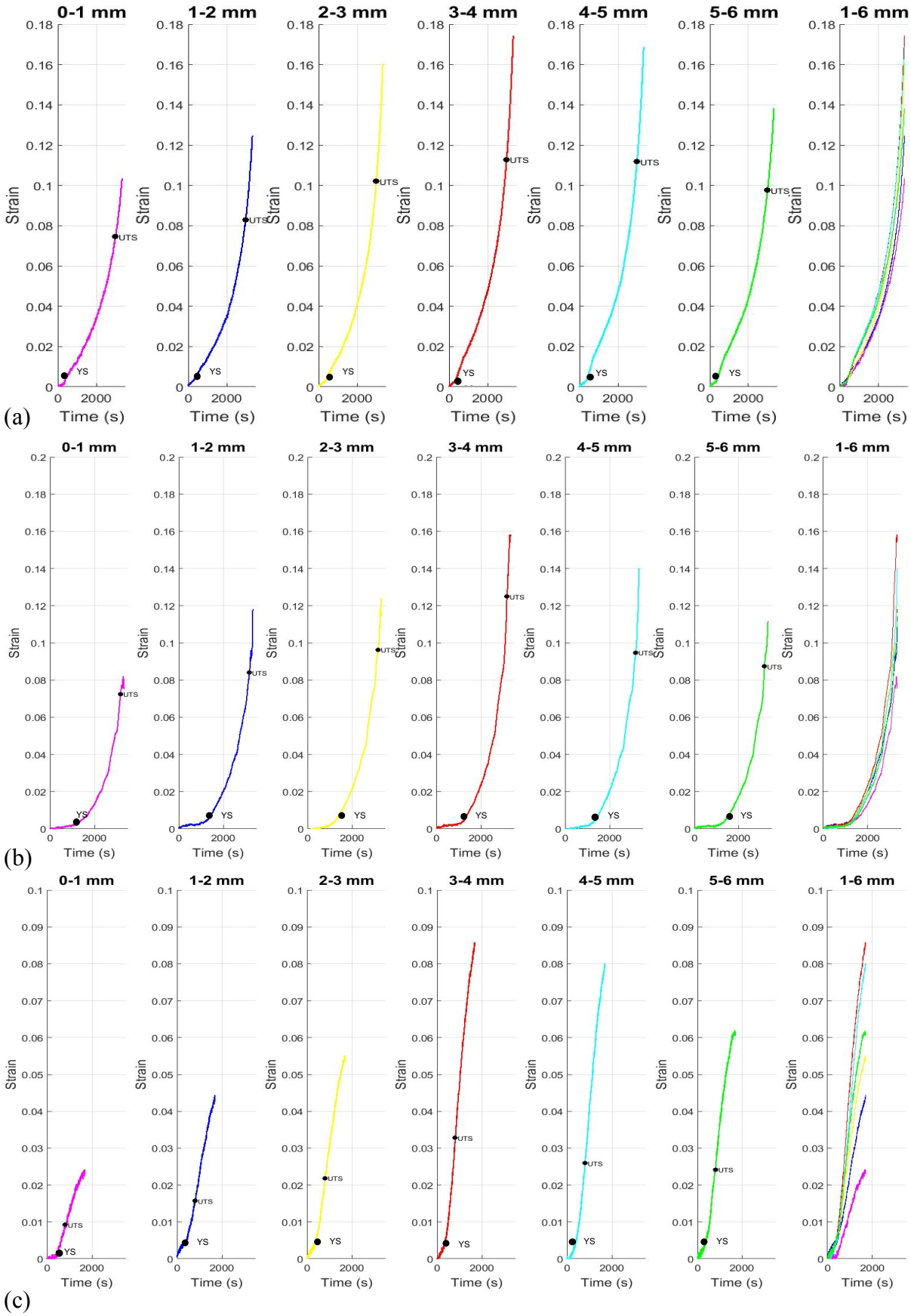

Figure 4.3.2-1: Incremental strain distribution across the LPW HAZ at (a) RT, (b) 300 ^{o}C and (c) 535 ^{o}C

4.3.3 STRAIN HARDENING COEFFICIENT

The strain hardening coefficient was determined by the Hollomon strain hardening equation (Equation 3.7.5-1). Stress data obtained from the Gleeble and incremental strain data recorded by the DIC system were converted into true stress and true strain data using Equation 3.6.5-2 and Equation 3.7.5-3. Subsequently, incremental true stress vs true strain curves were generated and are illustrated in Figure 4.3.3-1 for each experimental temperature.

Using the true stress vs true strain curves, the strain hardening coefficient was determined by curve fitting a polynomial over the plastic and elastic region of the true stress vs true strain curves. The strain hardening coefficient for each increment is illustrated in Figure 4.3.3-1. The average correlation coefficient of the curve fit taken over the six increments covering the HAZ and extending into the parent material was found to be 0.91, 0.88 and 0.89 for the RT, 300 ^{o}C and 535 ^{o}C experiments respectively; and provide reasonable confidence in the experimental results.

For all three experimental temperatures the strain hardening coefficient increased when moving from the weld material to the HAZ. For the RT experiments, the maximum strain hardening coefficient was recorded to have occurred in the fifth increment, whilst for the 300 ^{o}C and the 535 ^{o}C experiments the maximum strain hardening coefficient was recorded in the fourth increment. Even though the maximum strain hardening coefficient for the RT experiment was recorded in the fifth increment and not in the fourth increment, the differences between these two were negligible (0.01).

The strain hardening coefficient ranged from 0.136 – 0.149 for the RT experiment, 0.122 – 0.130 for the 300^{o}C experiment and 0.029 – 0.037 for the 535^{o}C experiment. With a correlation coefficient of approximately 0.89, it is very likely that the minimum and maximum strain hardening coefficient overlap thus the level of significant difference in strain hardening coefficient is low.

In order to fully understand the strain hardening coefficient evolution across the weldment, it has been found from previous studies that the strain hardening coefficient is strongly dependent on three properties, namely: microstructure grain size, temperature and strain rate [7]. The

combined influences of these properties would in turn result in the strain hardening coefficient distribution across the HAZ to be inhomogeneous. Figure 4.3.3-1 illustrates how the strain hardening coefficient increased when moving from the CGHAZ to the FGHAZ. The FGHAZ which is characterised by fine grains would have contributed to the strain hardening coefficient being largest in the region of the FGHAZ. This observation is in agreement with the findings made by Zhu et al. [7] where it was found that there was in inverse relationship between grain size and strain hardening coefficient.

The largest accumulation of strain across the HAZ was found to have occurred in the region of the FGHAZ. The gross accumulation of strain in the region of the FGHAZ would have resulted in a reduction in the specimen's cross sectional area which would have in turn caused an increase in strain rate in the region of the FGHAZ (especially for the experiments conducted at RT and 300 ^{o}C where necking occurred in the FGHAZ). An increase in strain rate in the region of the FGHAZ would have suggested a decrease in the strain hardening coefficient in this region, as a decrease in strain hardening coefficient would imply a decrease to the materials resistance to necking. The influence of strain rate would have countered against the effects of grain size however; in this analysis it was found that the effects of grain size had a greater influence on the stain hardening coefficient as the strain hardening coefficient increased in the region of the FGHAZ. Farabi et al. also reported that the strain hardening coefficient decreased with an increase in strain rate. It was deduced that higher strain rates lead to a stronger restriction to dislocation motion which in turn increased the strain hardening coefficient of the material [74].

It was also observed that the strain hardening coefficient decreased with an increase in experiment temperature. The average strain hardening coefficient for the RT and 300 ^{o}C experiments were 0.141 and 0.126 respectively, whilst for the 535 ^{o}C experiment the average strain hardening coefficient was 0.033. This finding was plausible as with an increase in experimental temperature there was more thermal energy available which made the material more ductile.

If the correlation coefficient was 1.0 then the differences in strain hardening coefficient in each increment would become more significant and reasonable to compare. With a more accurate reflection of the stain hardening coefficient, the influences due to grain size, strain rate and temperature can be better understood. The knowledge gained by accurately observing the

variation of the strain hardening coefficient across the HAZ will allow for weld material and/or welding parameters to be optimised aiming to for a balance in strength and ductility of the welds.

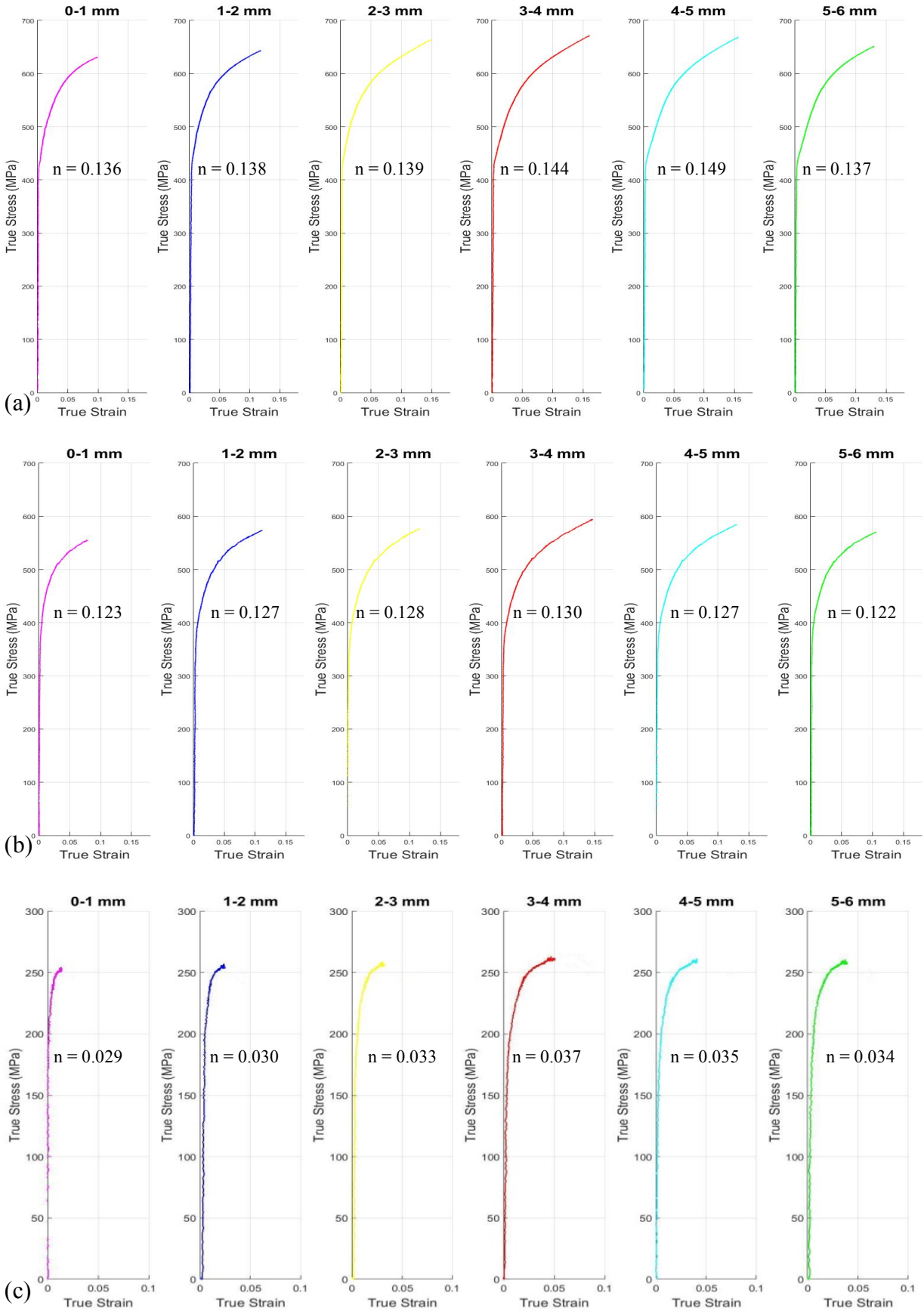

Figure 4.3.3-1: Incremental true stress vs. true strain curves of the LPW indicating the work hardening coefficient at (a) RT, (b) 300 ^{o}C and (c) 535 ^{o}C

4.4 TURBINE HOUSING WELD

In order to validate the application of the experimental technique a second weldment was placed under investigation. In this section the experimental results will be presented for the turbine housing weld (THW), first on a macro scale and then on a micro scale where the latter examines the strain distribution across the weld.

Tensile tests were conducted at three different temperatures (RT, 300 ^{o}C, and 535 ^{o}C) at a constant strain rate of 50 $\mu\varepsilon.s^{-1}$. To gain experimental confidence, each type of experiment was repeated; the repeat experiments can be found in Appendix 8.5.

4.4.1 MACRO SCALE STRAIN DISTRIBUTION

The total (acculturative) gauge strain was measured across the gauge length for each of the three experiment temperatures, and is illustrated in Figure 4.4.1-1. As was with the LPW experiments, secondary strains due to the application of the preload and thermal expansion were removed, and only the segments from when the specimen started to be extended at temperature are illustrated in these graphs.

The influences of machine compliance and actual material behaviour were also observed for the THW. Instead of a straight diagonal line passing through the origin, a bilinear strain-time trend was observed for each of the experiment temperatures. As was observed for the LPW experiments, the bilinear trend was more prominent for the RT and 300 ^{o}C experiments, and the strain rate at the end of the experiment was the highest at RT, and gradually decreased as the temperature was increased.

In the first segment (A-B) of the global (or total) strain-time curves, the strain initially remained at zero before it gradually increased at a constant strain rate up until the yield strength (YS). The length of segment A-B decreased with an increase in experimental temperature, this observation was primarily due to the effect of the material thermal softening. In the second segment (B-C) the specimen was observed to have strained at a much quicker strain rate. The increase in strain rate in segment B-C was as a result of slippage or take up within the Gleeble system which was observed to be most significant in the elastic region.

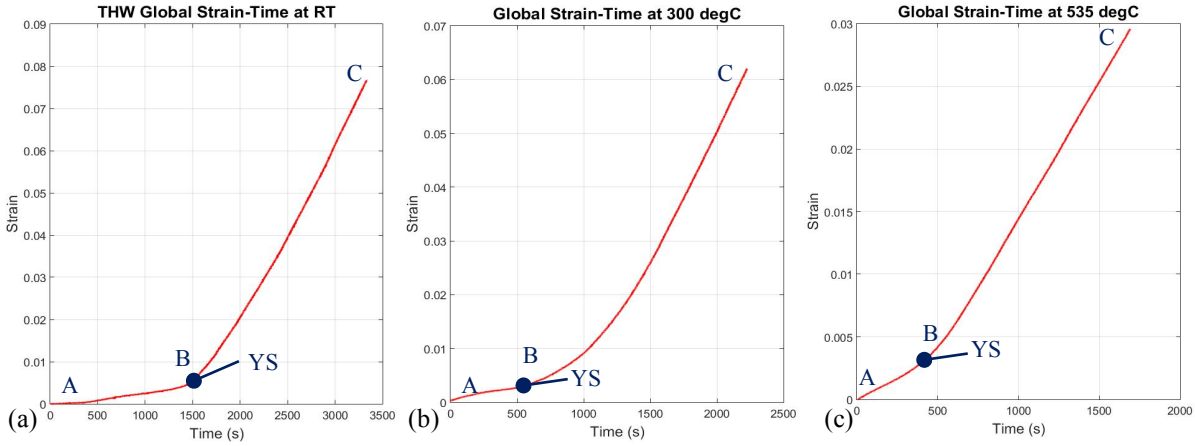

Figure 4.4.1-1: Global strain-time curves of the THW at (a) RT, (b) 300 ^{o}C and (c) 535 ^{o}C

The strain distribution across the each of the weldments were analysed by extracting the first Lagrangian principle strains just after yielding (YS), at the ultimate tensile stress (UTS), and at the end of the simulation. Figure 4.4.1-2 illustrates the strain and thermal distribution across the gauge length for each of the three experimental temperatures. The blue circular indicators illustrate the temperature distribution across the specimen's gauge length.

On analysis of the strain distribution across the gauge length at each of the three points of interest, the largest accumulation of strain for the RT and 300 ^{o}C experiments was found to have occurred in the weld material, whilst for the 535 ^{o}C experiment the largest accumulation of strain was found to have migrated to the region of the HAZ. As was observed for the LPW, it was also found that there was a rise and fall in strain moving from the weld material and across the HAZ. For the RT and 300 ^{o}C experiments, the strain distributions just after yielding (magenta curve) remained minimal, whilst the strain distribution at UTS (green curve) mimicked the strain distribution at the end of the experiment but to a less extent. However, for the 535 ^{o}C experiment the stain distribution just before yielding and at UTS remained minimal in comparison to the strain distribution at the end of the experiment.

For the 535 ^{o}C experiment, a maximum temperature of 544 ^{o}C was recorded at the centre of the gauge length, with a temperature difference of approximately 5 ^{o}C between the fusion line and the end of the HAZ. The migration of the point of localisation from the weld material (observed from the RT and 300 ^{o}C experiments) to the HAZ (observed from the 535 ^{o}C) was an interesting observation and was speculated to be due to the high temperature recorded across the HAZ, more than being due to the presence of a heterogeneous HAZ. In order to further

investigate if an increase in temperature triggered a change in the necked location, additional experiments were conducted at a temperature of 400 ^{o}C, 450 ^{o}C and 500 ^{o}C. At the lower experimental temperatures (300 ^{o}C and 400 ^{o}C) the largest accumulation of strain was found to have occurred in the weld material, indicating that the weld material was the weakest region. At 450 ^{o}C the location of the largest accumulation of strain also occurred in the region of the weld material however, it was observed to have migrated closer towards the HAZ when compared to the 300 ^{o}C and 400 ^{o}C experiments. Further increases in experimental temperature to 450 ^{o}C to 535 ^{o}C saw that the largest accumulation of strain migrate fully into the HAZ. Figure 5.2.2-1 (c) illustrates the strain distribution across the gauge length at 400 ^{o}C, 450 ^{o}C and 500 ^{o}C.

The increase in strain moving from the weld material and across the HAZ for each of the experiments was also observed. This finding is in accordance to the observations made for the LPW, where it was also found that the FGHAZ was the weakest zone of the weldment. For the RT and 300 ^{o}C experiments the strains across the HAZ at UTS and at the end of the experiment were almost identical, whilst for the 535 ^{o}C experiment there was a gross accumulation of strain between UTS and the end of the simulation. For each of these experiments the largest accumulation of strain recorded by the DIC software corresponded to the physical location at which necking occurred.

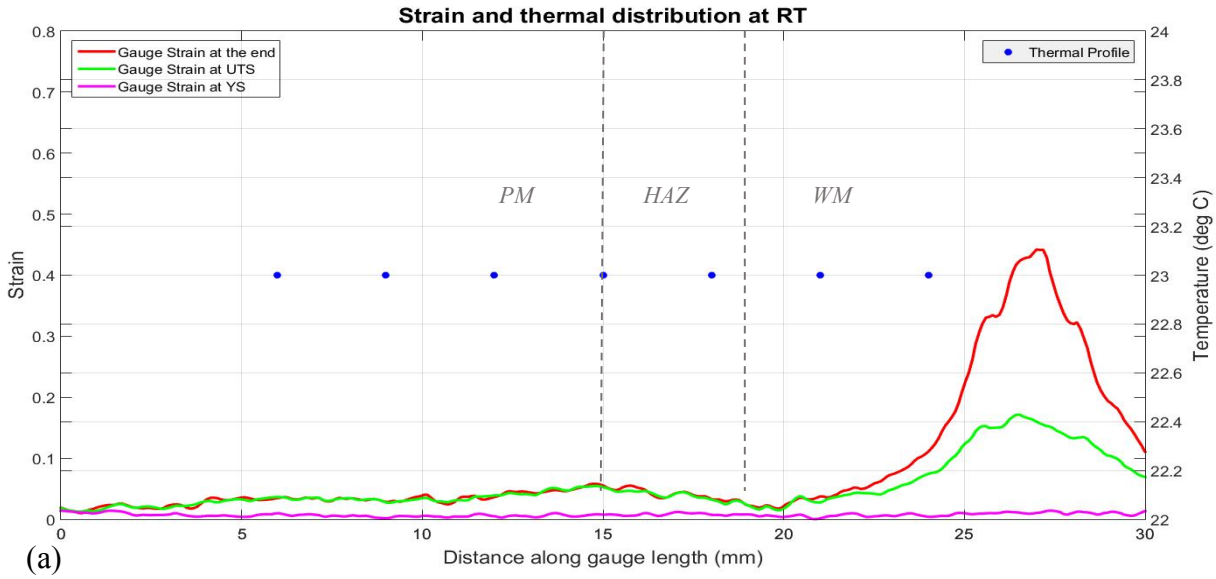

(a)

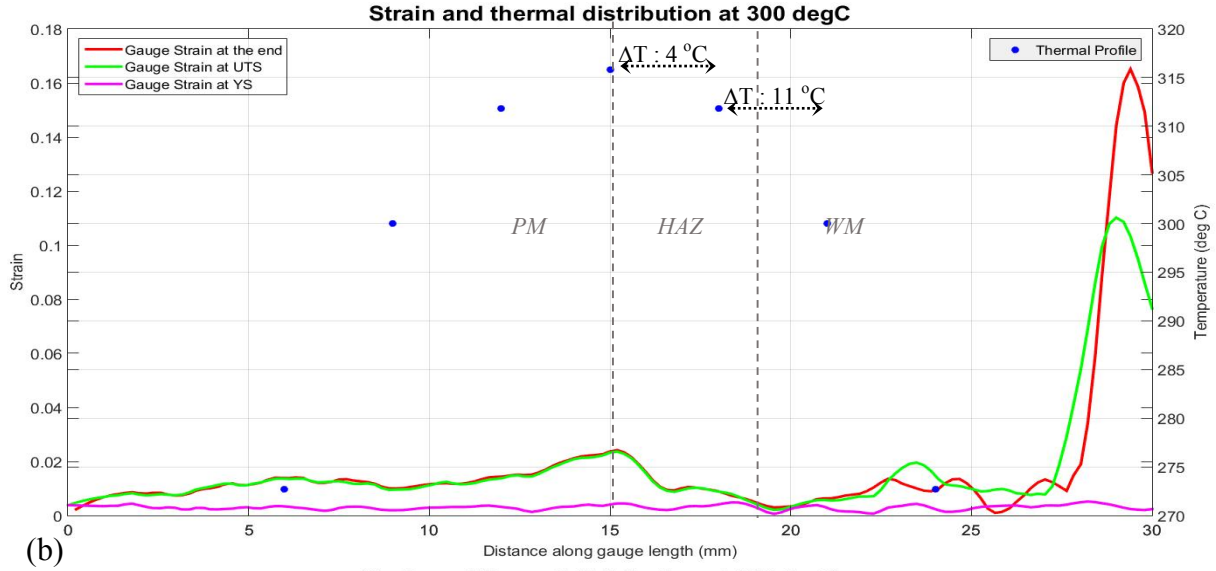

(b)

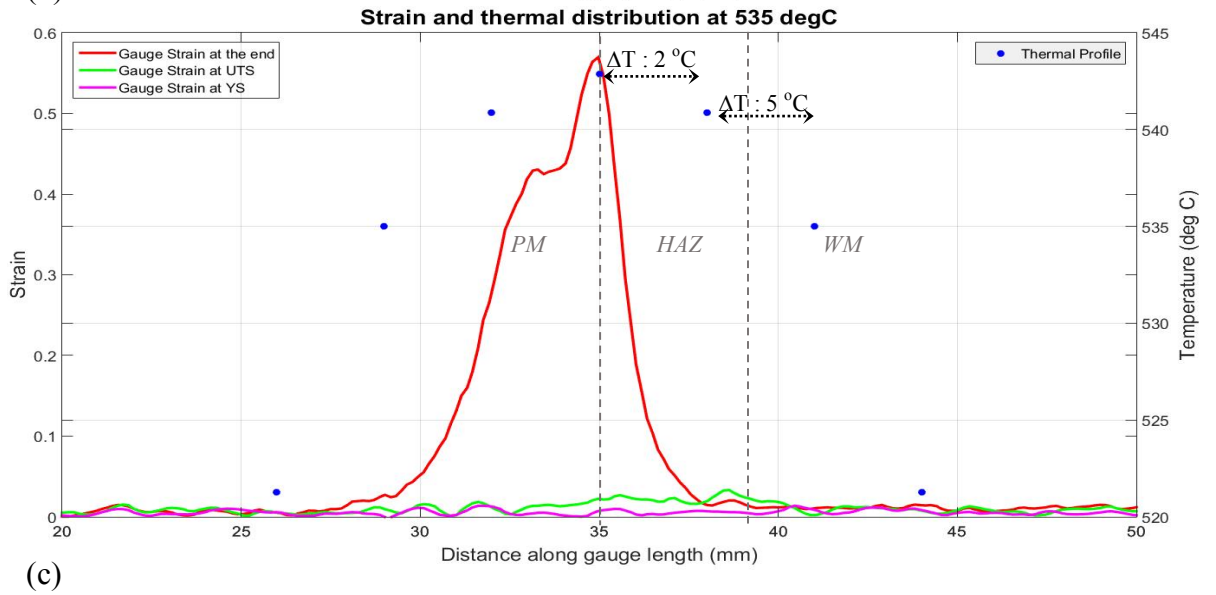

(c)

Figure 4.4.1-2: Strain and thermal distribution across the THW gauge length at (a) RT, (b) 300 °C and (c) 535 °C.

4.4.2 LOCALISED STRAIN DISTRIBUTION

The localised strain distribution across the HAZ at the end of each experiment are illustrated in Figure 4.4.2-1.

The trilinear form of the RT and 300 ^{o}C THW incremental strain distributions were similar to that of the LPW. The initial segment saw a gradual increase in linear-elastic in strain. In this segment the specimen was most resistant to elastic deformation which subsequently resulted in elastic deformation in the form of slack occurring thought the Gleeble's load train. The second segment which commenced once yielding had occurred saw a gradual increase in the strain rate. This observation was due to the reduction in specimen's cross sectional area which saw plastic deformation occurring only in the specimen's gauge; thus the strain rate between yielding and UTS was more or less constant. Unlike the LPW, the strain rate in the third segment was seen to have decreased post UTS. The strain distribution concluded in a plateau of strain which indicated that the specimen strained more in another region of the weldment and not in the HAZ. This observation is supported by the strain distributions illustrated by Figure 4.4.1-2 (a) and (b) where it was observed that there was a gross accumulation of strain in the region of the weld material. However, the strain distribution for the 535 ^{o}C experiment was almost bilinear in form. The gradual increase in linear-elastic strain due to slack in the system and the increase in strain rate due to reduction in the specimen's cross sectional area pre-UTS was found to have occurred in close succession after each other. Post UTS, reduction in the specimen's cross sectional area occurred in the HAZ and as a result the strain rate in this segment was the highest. The absence of the plateau in strain at the end of the experiment indicated that the specimen strained the most in the region of the HAZ.

For each of the three experimental temperatures it was observed that there was a gradual increase and then decrease in strain moving from the fusion line and into the parent material. As was found for the LPW, the maximum accumulation of strain was observed at the end of the HAZ (fourth incremental gauge line) for each of the experimental temperatures. This finding further confirmed that the HAZ nearest to the parent material; which was the FGHAZ was the weakest zone as it had strained the most relative to the other zones.

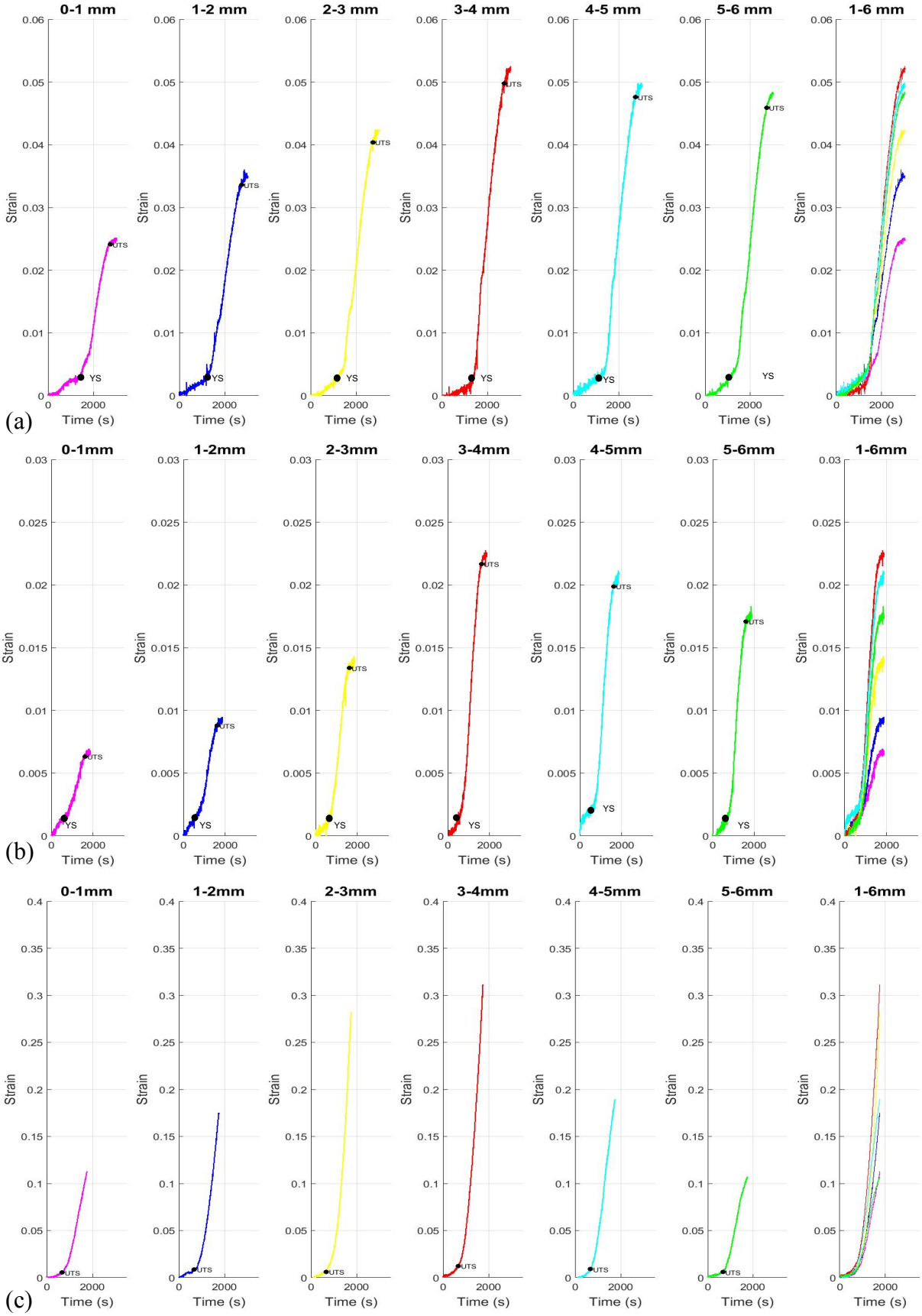

Figure 4.4.2-1: Incremental strain distribution across the THW HAZ at (a) RT, (b) 300 ^{o}C and (c) 535 ^{o}C

4.4.3 STRAIN HARDENING COEFFICIENT

The same method used to determine the strain hardening coefficient for the LPW was used for the THW; the strain hardening coefficient was determined using the Hollomon strain hardening coefficient (Equation 3.6.5-1). Incremental true stress vs. true strain curves were generated by combining stress data from the Gleeble with strain data from the DIC system.

By fitting a polynomial over the plastic and elastic region of the true stress vs. true strain curves the strain hardening coefficient was determined. The average correlation coefficient of the curve fit taken over the six increments covering the HAZ and extending into the parent material was found to be 0.89, 0.9 and 0.86 for the RT, 300 ^{o}C and 535 ^{o}C experiments respectively and provide reasonable confidence in the experimental results. The weaker correlation coefficient observed for the 535 ^{o}C could be as a result of the gross accumulation of strain that occurred across the FGHAZ.

From Figure 4.4.3-1 it is seen that the strain hardening coefficient ranged from 0.131 – 0.158 for the RT experiment, 0.132 – 0.143 for the 300^{o}C experiment and 0.037 – 0.075 for the 535^{o}C experiment; with a correlation coefficient of approximately 0.88. As was observed with the LPW, it is very likely that the minimum and maximum strain hardening coefficient overlapped thus the level of significant difference in strain hardening coefficient is low.

As was observed with the LPW weld, the strain hardening exponent increased when moving from the weld material to the HAZ. The effects of grain size had a greater influence on the stain hardening coefficient as the strain hardening coefficient increased in the region of the FGHAZ.

It was also observed that the strain hardening coefficient was much lower for 535 ^{o}C experiment than it was for the RT and 300 ^{o}C experiments. The average strain hardening coefficient for the RT and 300 ^{o}C experiments were 0.146 and 0.136 respectively, whilst for the 535 ^{o}C experiment the average strain hardening coefficient was 0.053. Even though an inhomogeneous distribution in strain hardening coefficient was observed across the HAZ, the significance of the distribution is low. A more perfect correlation coefficient would have attached greater significance to the difference in strain hardening coefficient.

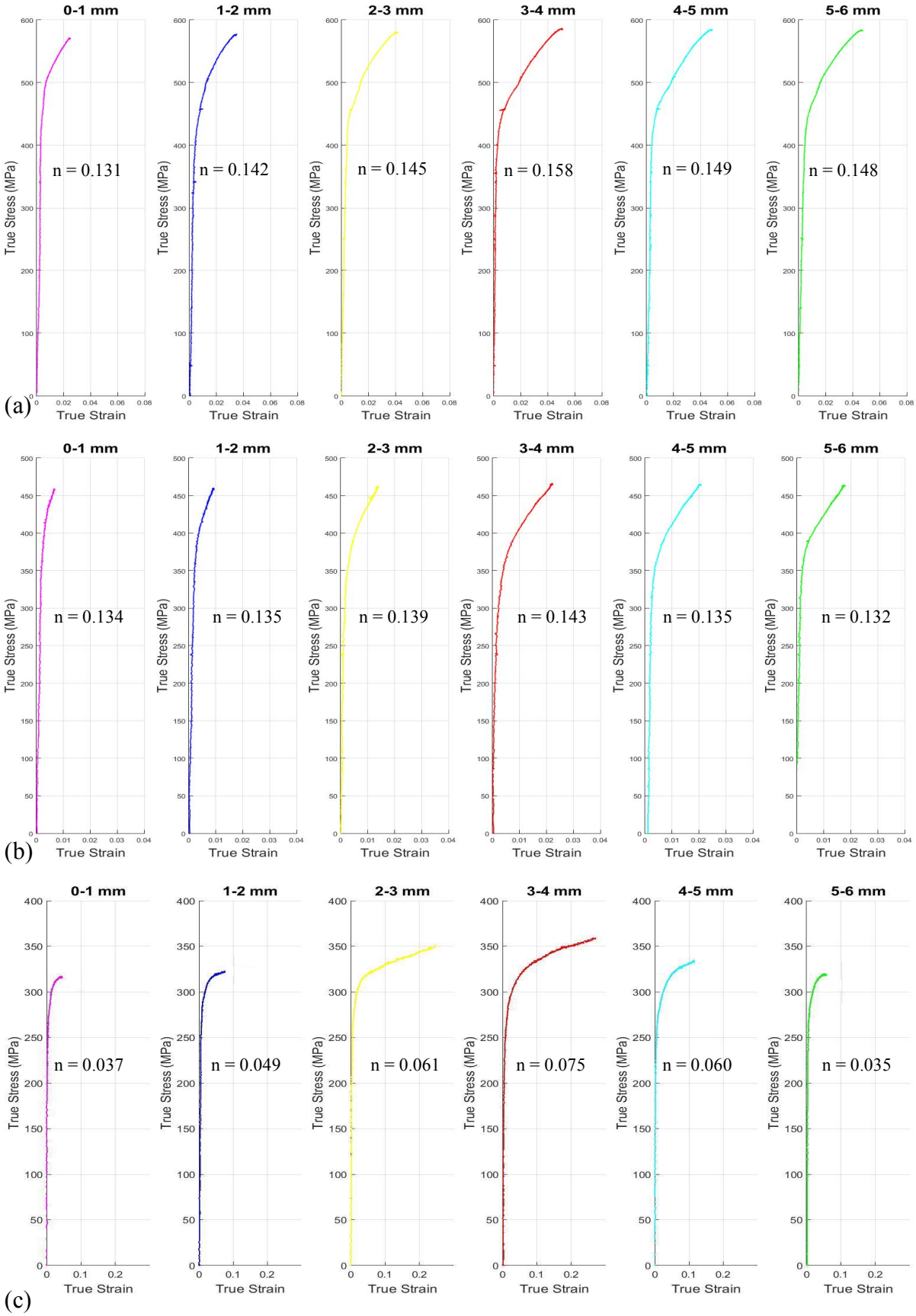

Figure 4.4.3-1: Incremental true stress vs. true strain curves of the THW indicating the work hardening coefficient at (a) RT, (b) 300 ^{o}C and (c) 535 ^{o}C

5 DISCUSSION

This section discusses the relevance of the experimental technique in light of the experimental development and validation outcomes. The overall objective of this study was to develop an experimental technique to measure the influence of temperature on the mechanical properties of weldments. The influence of temperature was analysed by observing the strain distribution across the loop pipe weld and the turbine housing weld as a function of temperature. Furthermore, a monolithic specimen containing just the parent material was analysed to compare the influence of temperature on each of the weldments with the parent material. Finally, significant sources of experimental error are discussed and recommendations are made.

5.1 EVALUATION OF THE EXPERIMENTAL TECHNIQUE

5.1.1 MICROSTRUCTURAL AND VICKERS HARDNESS ANALYSIS

In accordance with the operating temperatures for both the THW and the LPW being below the 727 ^{o}C phase transformation temperature, microstructural analysis of the parent material was found to comprise mostly of ferrite and cementite (α + Fe_3C), as illustrated by Figure 3.2.2-1. Due to the PWHT the HAZ for both welds was found to exhibit a combination of different microstructural phases. The grain size distribution across the HAZ allowed for the CGHAZ and the FGHAZ to be clearly identified, as illustrated by Figure 3.2.2-2.

Micro hardness ($HV_{0.3}$) tests were conducted on each weldment as outlined in section 3.2.3. For each of the welds, the highest hardness value was recorded at the fusion line (FL). A maximum hardness of 245 HV and 235 HV was recorded for the turbine housing weld (THW) and loop pipe weld (LPW) respectively. A possible reason for the peak hardness occurring at the FL was due to the FL strain hardening and becoming brittle during plastic deformation that occurred during the welding process [8]. On either side of the FL the hardness values decreased quickly, with the lowest hardness occurring in the weld material. Overall the THW had a harder hardness profile compared to the LPW; this indicated that due to the LPW's higher in service operating temperature it had undergone a larger degree of thermal softening. From both

hardness profiles, the length of the HAZ was determined to be approximately four millimetres wide. The hardness profile observed for both the THW and the LPW are similar to those found in previous studies [7], [8]. From both the light microscopy analysis and the hardness profile, it was established that the length of the HAZ for both weldments was approximately four millimetres wide.

5.1.2 SPECIMEN DESIGN AND OPTIMISATION OF THE THERMAL PROFILE

To reduce the effects of the irregular thermal loading, the length of the specimen's hot zone was optimised by following the geometry optimisation approach found in literature. This was achieved by reducing the gauge length cross-section of the conventional rectangular Gleeble tensile specimen. Due to the position of the weld zones relative to the edge of the steam pipe where it was cut off, the modified specimens were approximately 32 % shorter than the standard Gleeble specimen. By analysing the thermal profile of the short modified specimens, it was found that the thermal gradient across the HAZ was too steep for accurate material property extraction. Therefore, a series of adjustments were made to improve the thermal profile across the gauge length. These adjustments included:

1. Exchanging the Gleeble copper wedge grips for stainless steel wedge grips.
2. Drilling four millimetre holes through the ends of the specimens.
3. Increasing the four millimetre holes to six millimetre holes.

Each of these modifications improved the thermal profile across the gauge length. For the 300 ^{o}C experiments the thermal gradient across the HAZ improved from 22 ^{o}C to 7 ^{o}C, and for the 535 ^{o}C experiments the thermal gradient across the HAZ improved for 115 ^{o}C to 40 ^{o}C.

The thermal profile across the HAZ for the 535 ^{o}C experiments was found to still be too excessive, and as a result longer specimens were needed to improve the thermal profile. A longer specimen was achieved by welding on a piece of mild steel to the end of the specimen; however, this introduced the risk of the specimen failing at the new weld. In order to nullify this risk, the new weld was constrained to the thicker shoulder of the specimen. This modification was deemed successful for two primary reasons; firstly the new weld did not influence the overall behaviour of the material, and secondly the longer specimen improved

the thermal gradient across the HAZ. By using a longer specimen, the thermal gradient across the HAZ for the 535 ^{o}C experiment was further improved from 40 ^{o}C to 9 ^{o}C, and for the 300 ^{o}C experiments the thermal gradient improved from 7 ^{o}C to 4 ^{o}C. The sequential improvement to the thermal profile can be seen in Figure 3.4.2-6 and Figure 3.4.2-7.

Errors associated with the IR system included the emissivity of the IR window and of the paint. The surface emissivity and transmission correction of the IR window were adjusted until the maximum temperature corresponded to the Gleeble control thermocouple. An approximate transmission correction factor of 53 ± 2 % was used for all experiments. A single emissivity value was applied across the high temperature paint across the entire gauge length. It was found that the black paint discoloured in regions of the hot zone. This error can be minimised by using a high quality paint capable of withstanding higher temperatures. Furthermore, installing an analogue to digital connection from the Gleeble to the IR camera will also minimise the errors associated with manually synchronising the thermal data from the Gleeble and the IR camera.

5.1.3 ALIGNMENT OF THE GLEEBLE AND DIC DATA

By combining displacement data from the DIC system with temperature, force and displacement data from the Gleeble, insight of the mechanical and material properties across each of the weld zones were gained.

A comparison of the global strain determined by both the Gleeble and DIC data found that there was a discrepancy in strain across the gauge length. The Gleeble's strain data was found to be a straight diagonal line, whilst the DIC's strain data was trilinear, as illustrated in Figure 3.6-1. This discrepancy in strain profile was found to be due to the different techniques each of the two systems used to measure strain. Strain data from the Gleeble direct output was measured by recording the cross head displacement of the stroke, whilst the DIC system measured strain by evaluating the relative displacement of pixels. The fundamental difference between the strain data from the Gleeble and DIC was due to machine compliance; which is the nonlinear displacement associated with the many linkages within the Gleeble system. The strain data from the DIC was determined as being a true reflection of the gauge strain as it

overcame the influences of machine compliance and necking on the actual material behaviour as the specimen was extended.

Data from the Gleeble and DIC were synchronised by introducing a strain artefact. During the heating period a preload was applied to the specimen which acted as the strain artefact. Strain-time curves were generated using data from both the Gleeble and DIC system, and using the strain artefact as a reference a time stamp was determined by comparing the delay between the Gleeble and DIC data. Using this time stamp, DIC data were aligned to match the Gleeble data.

Synchronising of the Gleeble and the DIC system was possibly another source of error with the experimental technique. In this study, the DIC system was initiated separately before the Gleeble system. During data processing, the two systems were synchronised manually. In order to eliminate the error associated with manual synchronisation, an analogue to digital connection can be installed from the Gleeble to the DIC system which will automatically synchronise the two systems.

5.2 APPLICATION OF THE EXPERIMENTAL TECHNIQUE

5.2.1 STRESS-STRAIN BEHAVIOUR OF THE WELDS AS A FUNCTION OF TEMPERATURE

High temperature tensile tests were conducted on the steam penetration material (parent material), LPW and the THW at a constant strain rate of 50 $\mu\varepsilon.s^{-1}$.

From the tensile test experiments, ranging from RT to 535 ^{o}C illustrated in Figure 4.2-1, a steady decrease in material strength was observed as the tensile test temperature was increased. When a material is heated its atomic bonds weaken due to a decrease in binding energy, and consequently the material weakens. With an increase in temperature from RT to 535 ^{o}C, the parent material's yield and ultimate tensile strength was found to have both decreased by 46 %, and 48 % respectively, as illustrated in Figure 5.2.1-1.

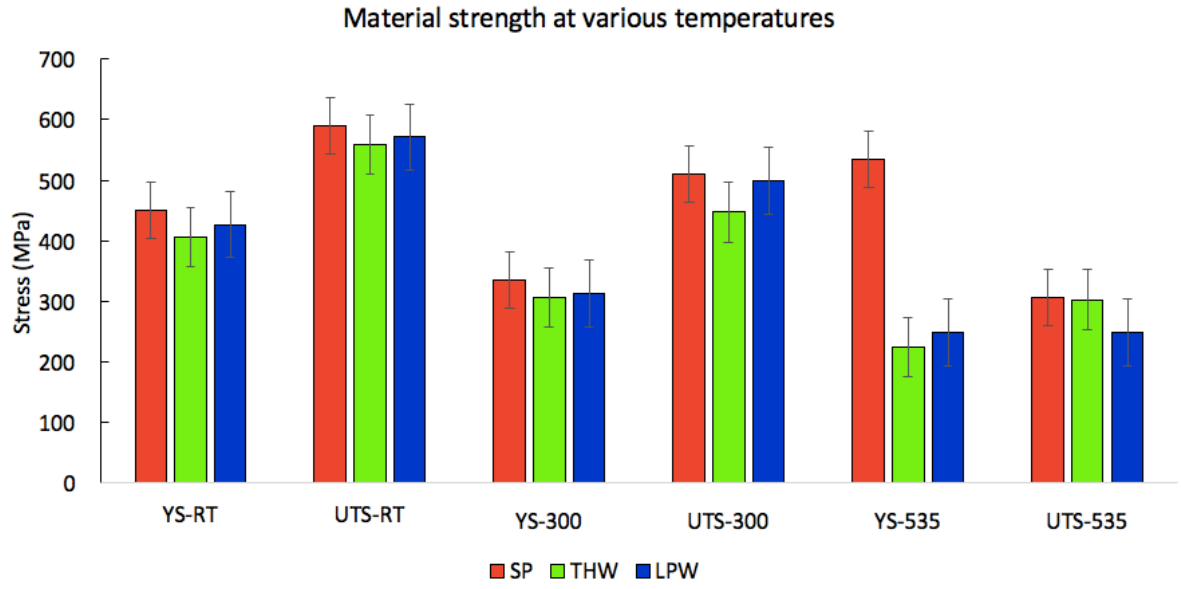

Figure 5.2.1-1: Material strength at various temperatures.

The welded specimens (LPW and THW) also displayed a decrease in material strength with an increase in experimental temperature. However, the reason for this can be attributed to both the decrease in atomic binding energy, as well as to the presence of a heterogeneous weld zone. The type of weld filler material selected is governed by the desired weld strength abilities. By choosing a weld filler material that has dissimilar strength properties compared to the parent material, allows for material degradation to be concentrated in the weaker of the two materials.

In this instance, due to the size and geometric complexities of the steam penetration, it would have been deemed most economical to have a sacrificial weld filler material, thus a weaker weld filler material would have been selected.

With an increase in temperature from RT to 535 ^{o}C, both the LPW and THW specimen's yield and ultimate tensile strength were found to have both decreased more than that of the parent material. The welding process would have attributed to this finding. During the welding process the material is subjected to high melting temperatures, and consequently a temperature gradient is developed from the weld location to the unaffected material. The hottest region would be at the weld location, and the temperature would taper off towards the extremities of the weld. Due to the application of elevated temperatures in the region of the weld material, the weld material would have undergone some degree of annealing, and subsequently its material's strength would have decreased.

The LPW's yield and ultimate tensile strengths decreased by 58 % and 57 % respectively, and the THW's yield and ultimate tensile strengths decreased by 45 % and 46 % respectively. The material strength disparities between the THW and the LPW could be attributed to a number of reasons, namely: the welds were exposed to different operating temperatures, the difference in the weld filler material properties, dissimilar welding and PWHT could have been used, and the change in location at which necking occurred.

In this study, each type of experiment was repeated once. Figure 5.2.1-2 illustrates a comparison of material strength between the two experiments for each of the welds. On a macroscale, the material properties between the original experiment and the repeat experiment for both the THW and the LPW were very similar. This indicated good experimental variability, and placed confidence in the experimental setup and data acquisition procedures. A maximum deviation of 7 % and 8 % was found to have observed for the yield strength at 300 ^{o}C for both the THW and the LPW respectively.

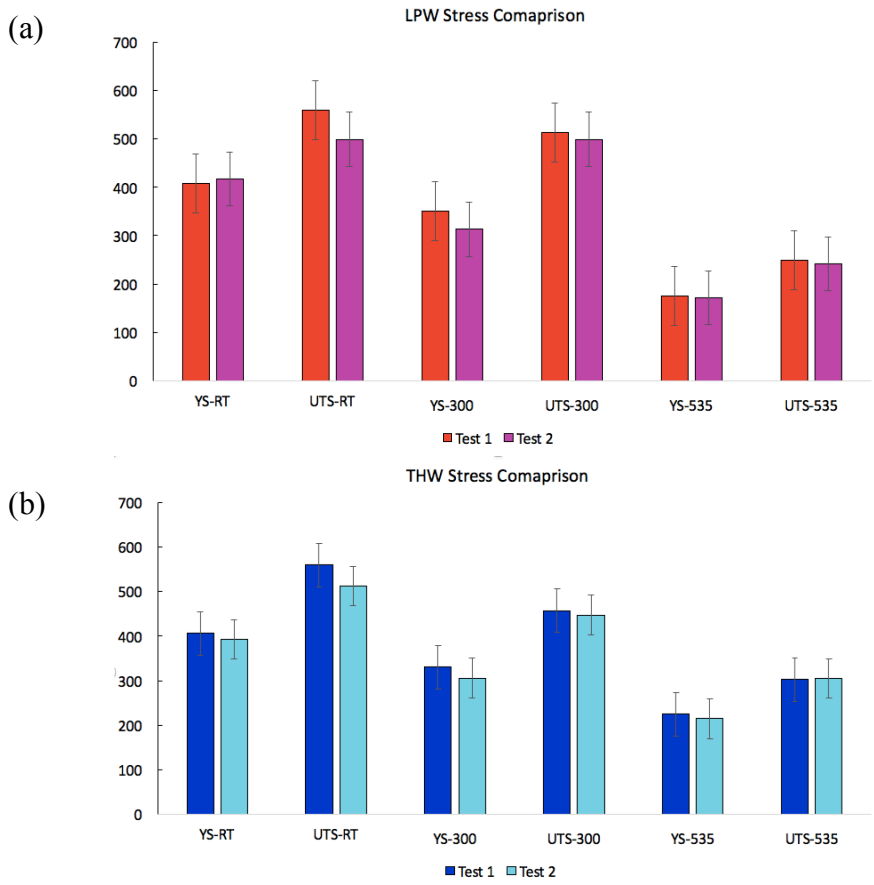

Figure 5.2.1-2: Material strength comparison of two test at three different temperatures for (a) the LPW, and (b) the HPW.

5.2.2 MACRO-STRAIN DISTRIBUTION ACROSS THE WELDS

For each of the weldments, the location at which necking occurred was found to have been influenced by two main contributors; firstly, the presence of a temperature gradient across the gauge length, and secondly due to the inhomogeneous microstructure across the HAZ. In order to remove the influence of an inhomogeneous microstructure, a monolithic specimen containing only the parent material was elongated at temperatures ranging from RT to 535 ^{o}C.

The monolithic specimen was used to compare the influences of temperature on the mechanical properties of the two weldments. The monolithic specimens were elongated at the identical strain rate and temperatures as the specimens containing welds. Figure 5.2.2-1 illustrates the strain distribution across the gauge length for each of the three materials (PM, LPW and THW).

By elongating a monolithic specimen, the influence of an inhomogeneous microstructure was eliminated, and only the influence of temperature on strain accumulation was observed. Figure 5.2.2-1 (a) illustrates the strain accumulation for the monolithic specimen. Ignoring the 7 ^{o}C and 4 ^{o}C temperature gradients along the specimen for the 535 ^{o}C and 300 ^{o}C experiments, it was seen that the largest strain accumulation occurred at the centre region of the specimen. For the 300 ^{o}C experiment a maximum strain of approximately 0.07 was found, and for the 535 ^{o}C experiment, the maximum strain increased to 0.58. This result served as confirmation that the largest accumulation of strain will occur at the centre of a homogenous specimen.

For the LPW, illustrated in Figure 5.2.2-1 (b) the peak strain occurred within a 15 millimetre band in the region of the HAZ and the weld material. The influence of increasing temperature was not very prominent. For the 300 ^{o}C experiment the maximum accumulation of strain occurred in the HAZ, with the second highest accumulation of strain occurring 10 millimetres away into the weld material. However, for the 450 ^{o}C and the 535 ^{o}C experiments the maximum accumulation of strain migrated from being located in HAZ to being located in the weld material; approximately 15 millimetres away from the HAZ. At these two experimental temperatures the second highest accumulation of strain was found to have occurred in the region of the HAZ.

For the THW, illustrated in Figure 5.2.2-1 (c), the influence of increasing temperature was noticeable. Depending on the experimental temperature necking was observed to have occurred in various regions of the weldment, ranging from the weld material to the parent material. At lower experimental temperatures (300 ^{o}C and 400 ^{o}C) the largest accumulation of strain occurred in the weld material, indicating that the weld material was the weakest region. Whilst for higher temperatures (450 ^{o}C to 535 ^{o}C) the location of the peak strain migrated from the weld material and into the parent material. With an increase of temperature from 300 ^{o}C to 535 ^{o}C there was a 71 % increase in the maximum recorded strain.

The purpose of these sets of experiments was to gain an understanding of the influence of temperature on the weldment. From the previous results, the strain distribution patterns across the gauge length were found to be attributed to both the presence of an inhomogeneous microstructure and elevated temperatures. The monolithic parent material experiment removed the influences of the inhomogeneous microstructure and assessed only the influence of temperature. Here it was found that for both the 300 ^{o}C and the 535 ^{o}C tests, necking occurred

at the centre of the specimen. However, for the both the THW and the LPW it was found that the weld material was the weakest region. From the THW and LPW strain distributions, it was found that the presence of the weldment reduced the strength of the parent material, and subsequently an increase in temperature further aided a reduction in strength.

The difference in the LPW and the THW material behaviour at various temperatures is due to the difference in operating conditions that these two welds were exposed to. The LPW had nominal operating conditions of 535 ^{o}C and 16.1 MPa, whilst the THW had nominal operating conditions of 332 ^{o}C and 4.1 MPa. The ability to detect the change in strain behaviour for each of the two weldments at varying experimental temperatures validates the experimental technique and evaluation procedure followed.

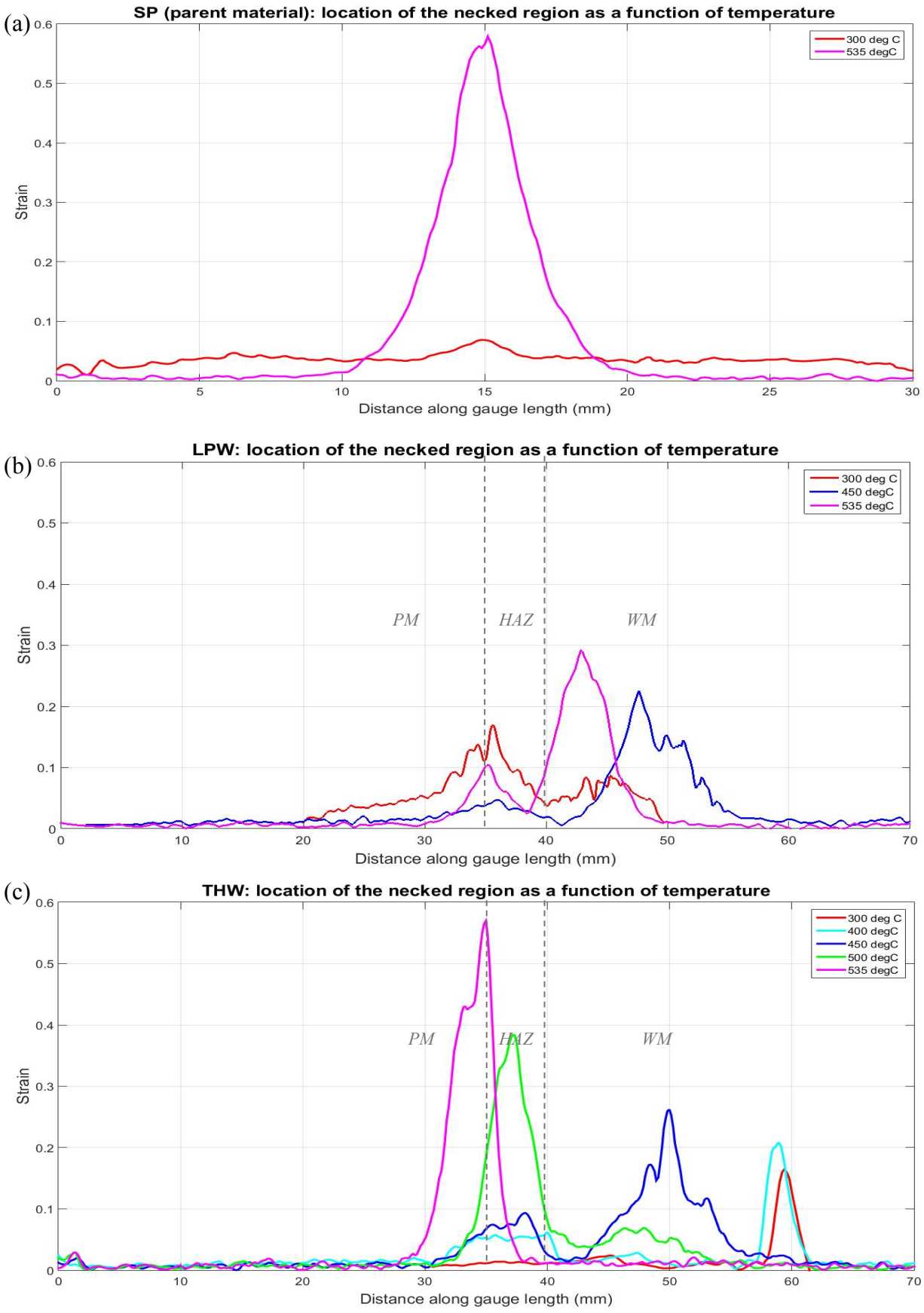

Figure 5.2.2-1: Strain distribution across the gauge length of (a) the steam penetration / PM, (b) LPW, and (c) THW to failure.

5.2.3 LOCALISED STRAIN DISTRIBUTION ACROSS THE WELDS

Localised strain analysis across the HAZ was conducted by virtual strain gauges of one millimetre in length at intervals of one millimetre apart; covering a total distance of six millimetres, as outlined in detail in section 0. The first one millimetre increment commenced at the FL and progressively moved through the CGHAZ, FGHAZ and into the parent material

For all of the LPW and the THW experiments (including the repeat experiments) the localised strain distributions across the HAZ illustrated that there was an increase in strain from the first incremental gauge line to the fourth incremental gauge line; thereafter the strain decreased in the remaining two incremental gauge lines. The gradual rise in strain from the FL (first incremental gauge line) up until the FGHAZ (fourth incremental gauge line) was observed in all of the experiments, and indicated that the FGHAZ was the weakest region of the HAZ; a similar finding was reported by Saranath et al. [16]. Saranath et al. reported that the FGHAZ was the weakest zone in a weld as it was furthest from the heat source during welding, thus the microstructural restoration processes were not as prominent as other regions of the weldment. And as a result, the FGHAZ consisted mostly of soft ferrite and pearlite colonies.

Comparing the incremental strain distribution between the first experiment and the repeat experiment revealed that there was a variation in the strain recordings. The primary reason for this variation was the placement of the virtual strain gauges. Even though a fixed marked point was scribed onto the specimen, and the DIC system was magnified to its maximum magnification (200 %) when placing the virtual strain gauges, it was still found that a slight human inaccuracy in placing a virtual strain gauge did cause a significant difference in data from experiment to experiment. Figure 5.2.3-1 illustrated the slight deviation in the placement of the virtual strain gauges.

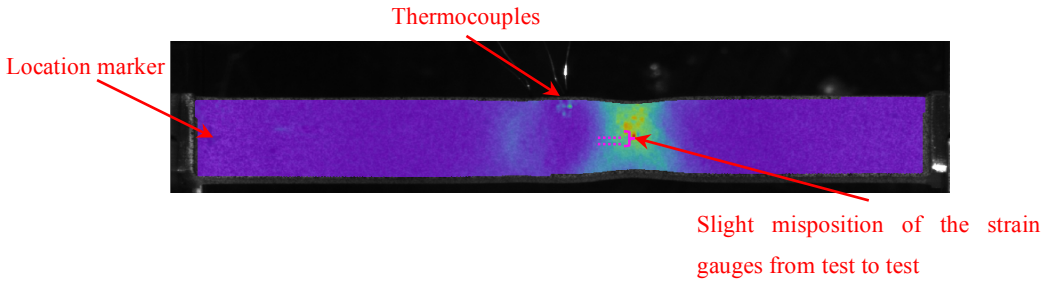

Figure 5.2.3-1: Schematic illustrating the placement of the virtual strain gauges (not drawn to scale).

Additional areas for the introduction of uncertainty in testing could be due to the size of the speckle pattern, disparities in lighting conditions, base floor noise and uneven circumferential material degradation. A speckle pattern with a larger diameter would not be able to detect small displacements when compared to speckles of a smaller diameter. If the speckle pattern diameter is too large, the DIC software will be unable to detect small displacements as there would be no apparent change in pixel movement. This inaccuracy can be compensated for by increasing the subset size which will be at the cost of a decrease spatial resolution.

Furthermore, disparities in lighting signal due to frequency flickering and/or stray shadows would also attribute to variations in strain readings. The inherent floor vibrations caused by the Gleeble machine itself and/or other disturbances in the building would have induced artificial displacements to the speckle pattern. In order to quantify this variation, a tensile specimen was placed within the Gleeble chamber and a sequence of 20 photographs were recorded without the Gleeble being turned on. Post processing these 20 photographs revealed that base floor vibration attributed up to 0.015 artificial strain. Lastly, due to systematic vibrations experienced at the coal fired power station, there were inherent unbalanced hoop stresses around the steam penetration pipe, and this would have caused dissimilar material degradation patterns around the pipe. Therefore, when a specimen from a high damaged segment of the pipe was loaded, it would have strained more than a specimen from a less damaged segment.

In essence, a weldment is a composite material, comprising of a set of materials in series. Using the analogy of a set of springs in series; when a force is applied to the springs the element with the lowest stiffness will deform the most. Figure 5.2.3-2 illustrates the behaviour of a set of springs in series when an external load is applied.

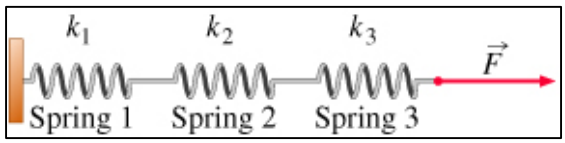

Figure 5.2.3-2: Hooke's law explanation for a set of springs in series [75].

$$F = kx : Hookes's\ Law$$

where F is the applied force in N, k is the coefficient of spring stiffness in N/mm and, x is the displacement in mm.

The overall displacement (x_T) of all three springs due to the applied force, is modelled using the following relationship:

$$X_T = \frac{F}{k_1} + \frac{F}{k_2} + \frac{F}{k_3}$$

Thus, it can be seen that the spring with the lowest coefficient of spring stiffness will be displaced the most.

The weld material, HAZ, and parent material all act as separate springs in series, each with its own material (plastic) stiffness. From the tensile tests conducted in this study, it was found that the FGHAZ was the weakest material in the weldment as it showed the largest amount of strain. In a study assessing the microstructure and material properties of an aged chromium steel weldment, Molokwane et al. also reported the FGHAZ was the weakest zone [67]. Molokwane et al. reported that the decrease in mechanical properties in the FGHAZ was due to a coarse distribution of $M_{23}C_6$ precipitates, as well as to the fine grained microstructure which formed after the welding process.

For each of the three different experimental temperatures, and for each of the two welds, there was a fluctuation in recorded strain values. The significance of these elevated experimental temperatures was to mimic the service operating temperatures that the steam penetration was exposed to. The THW and the LPW were exposed to operating temperatures of 332 ^{o}C and 535 ^{o}C respectively. Figure 5.2.3-3 illustrates the strains across the HAZ for each of the three experimental temperatures.

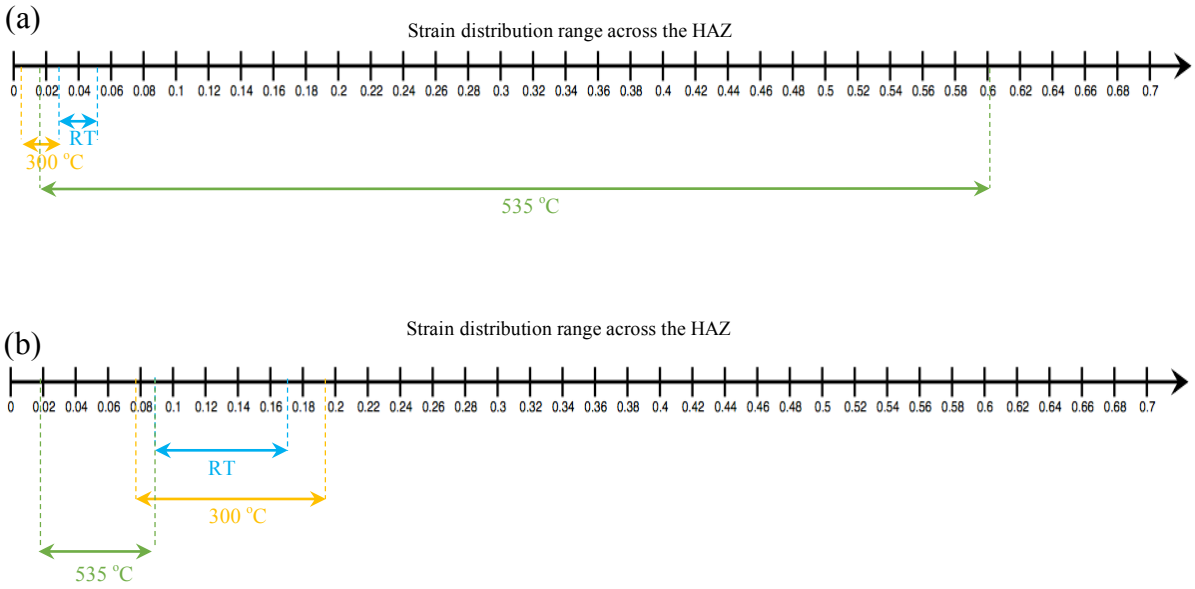

Figure 5.2.3-3: Strain distributions across the HAZ at various temperatures for (a) THW, and (b) LPW.

It can be seen that there was a significant variation in the strain values at the same temperature between the two welds. The primary reason for this was that the welds necked at different locations for each temperature range. For example, at 535 °C the THW necked in the HAZ which corresponded to the hottest point of the specimen, whilst the LPW necked in the weld material. Another reason for this variation may include the removal of the actual steam penetration pipe from the power station. The process whereby the steam penetration pipe was cut at each of the welds was unknown. Therefore, it remains unclear where a coolant was used, and if the cutting temperature was high enough to anneal any of the two welds.

A similarity between the two welds was that the localised strain across the HAZ at 300 °C and 535 °C occurred at a lower global strain than the RT experiment. This finding was plausible, as at higher temperatures there was more energy available for dislocation activation and mobilization.

5.2.4 STRAIN HARDENING COEFFICIENT

For each of the welds the strain hardening coefficient was determined using the Hollomon strain hardening equation for each increment across the HAZ. True stress vs. true stain curves were generated for each increment and a polynomial curve fit over the plastic region up until UTS was used to determine the strain hardening coefficient in each increment.

A distribution in strain hardening coefficients was determined across the HAZ for each of the welds. An inhomogeneous distribution in strain hardening coefficient was expected due to the influences of grain size, strain rate and temperature. However, the significance of the variation in strain hardening coefficient across the HAZ is low. The average correlation coefficient of the polynomial curve fit taken over the six increments covering the HAZ and extending into the parent material for both welds was found to be approximately 0.9, and provide reasonable confidence in the experimental results. A correlation coefficient of 0.9 is not adequate to place significance on the strain hardening coefficient distribution across the HAZ as it is very likely that the minimum and maximum strain hardening coefficient overlap and thus the strain hardening coefficient across the HAZ may in fact be constant.

The method used to determine the stain hardening coefficient could be a possible source of error. Instead of curve fitting a polynomial over the plastic region, the gradient of a log true stress vs. log true strain could also be used to determine the strain hardening coefficient in each increment. In addition, an alternate strain hardening coefficient equation such as the Ludwik relationship could be used. Zhu et al. found that the strain hardening coefficient derived from using the Hollomon equation differed when compared to the strain hardening coefficient determined from the Ludwik equation [24].

5.3 IMPROVEMENTS AND RECOMMENDATIONS

The Gleeble window was a source of optical distortion which affect the quality of the DIC images. This can be overcome by fitting an optical quality window with a lower refractive index which will be better suited for recording digital images. Furthermore, the external LED lighting had to be positioned very close to the window, and consequently over exposed reflections developed. This type of error can be minimised in future research by using linear polarised filters which will reduce the glare, as well as by mounting LED lighting inside of the Gleeble chamber.

In section 3.5, the facet and grid spacing sizes were refined once, and subsequently kept constant for all remaining analysis. The facet and grid spacing sizes are critical in determining accurate displacements as it demarcates the area used by the correlation algorithm to track displacements. Smaller facet and grid spacing sizes are capable of resolving down to smaller displacements. Future research can further investigate the effects of reducing the facet and grid spacing sizes and its influences on determining localised strain across the different weld zones.

One of the potential sources of error with the DIC system was due to the debonding of the speckle pattern paint. It was found that the paint discoloured at elevated temperatures, which resulted in a narrower range in grayscale facets for the DIC correlation algorithm. Furthermore, the paint was also found to have peeled off in regions where the specimen necked, and as a result these areas could not be correlated further by the DIC software. To improve on these distortions, a more robust paint with a higher colour stability at elevated temperatures should be used. The irregularities due to paint speckling can be avoided altogether by applying a thinner layer of paint as well as by using alternate speckling techniques such as chemical etching.

A main uncertainty in understanding the influence of temperature on the weld zone was the position of the FL relative to the gauge length. The FL had to be positioned at the centre of the gauge length due to the length of material available. Due to direct resistance heating, the centre of the gauge length was the hottest region and therefore the weld material evolution was always in the hottest region of the specimen. In order to improve on this understanding, future studies

may include increasing the size of the hot zone as well as moving the position of the FL relative to the hot region, thus the influence of temperature on the weld will be more apparent.

In order to contribute towards material behaviour and creep models, the strain rates can be reduced to meet those of typical creep tests. By reducing the strain rate and extending the duration of the experiments at elevated temperatures will mimic the in service material behaviour. This will provide useful information and insight of the localised weld behaviour which can contribute towards creep models.

6 CONCLUSION

The influence of temperature on the mechanical properties of a weldment was investigated experimentally. An experimental technique that was capable of recording strain deformation across the localised zones of a weldment at elevated temperature was developed and applied to two dissimilar welds. As set out in section 1.3, subsidiary objectives of this study included:

a) Design of a tensile specimen to include a weldment at its centre.

- Tensile test specimens from both weld zones were machined such that that fusion line was located at the centre of the specimen's gauge length. This was done to ensure that the weld zones were located in the hot zone which was required for accurate strain localisation measurements.

b) Optimisation of the thermal profile of the designed tensile specimen.

- A reduced cross-section Gleeble specimen was found to have improved the thermal gradient compared to the conventional square cross-section Gleeble specimen.

- Replacing the copper wedge grips with stainless steel wedge grips was also found to yield a more favourable thermal gradient across the gauge length.

- Removing material from heat sink locations also improved the thermal profile. Six millimetre diameter holes drilled into either end of the specimen was found to have improved the thermal gradient to a larger extent when compared to the thermal gradient achieved from the four millimetre diameter holes.

- The thermal gradient across the gauge length was also found to have improved by extending the specimen length from 84 millimetres to 124 millimetres.

c) Accurately identifying and characterising the different heat affected zones.

- Light microscopy from both welds revealed similar features. The fusion line (FL) was easily identified, and a distribution in grain sizes was observed from the coarse grain heat affected zone (CGHAZ) through to the fine grain heat affected zone (FGHAZ). From the light microscopy analysis the length of both weld zones was measured to be approximately four millimetre wide.

- Micro-hardness tests for both welds revealed that the peak hardness occurred at the FL, with a gradual decrease in hardness occurring in the parent material. The peak in hardness at the FL was due to brittleness, which was as a result of strain hardening that occurred during plastic deformation experienced during welding. Soft ferrite islands in the heat affected zone (HAZ) saw the decrease in hardness values from the FL through to the HAZ. Micro-hardness tests for both welds confirmed that the width of each weldment was approximately four millimetres wide.

d) Evaluating the experimental technique by monitoring the evolution in material properties across the two dissimilar weldments.

- From the high temperature tensile tests it was found that the parent material was stronger than both the welds. This finding confirmed that the presence of a weldment weakens a material.

- On a macro-scale, an evaluation of strain across the gauge length revealed a rise in strain in the region of the HAZ. This observation was made for both welds at each of the three experimental temperatures, and indicated that the HAZ closest to the parent material (which was the FGHAZ) was the weakest zone as it had strained the most relative to the rest of the HAZ.

- Observing the localised strain distribution across the HAZ illustrated in more detail the gradual increase and then decrease in strain moving from the fusion line into the parent material. In each of the experiments the maximum accumulation of strain was observed

at the end of the HAZ. This finding further confirmed that the FGHAZ was the weakest zone as it had strained the most relative to the other zones.

- It was observed that there was a difference in strain measurements between the two welds at the same experimental temperature. This variation in strain was found to be due to the different operating temperatures and pressures that the two welds were exposed to, as well as possibly due to the unknown procedure and conditions used to remove the steam penetration pipe from the coal fired power station.

- At elevated temperatures (300 ^{o}C and 535 ^{o}C) it was found that strain across the HAZ occurred at lower strain values than at RT. This finding was plausible as at higher temperatures there was more energy available for dislocation activation and mobilization.

- Experimental investigation of extending a monolithic specimen (containing only the parent material) removed the influences of the inhomogeneous microstructure, and assessed only the influence of temperature. For each of the experimental temperatures it was found that necking occurred at the centre of the specimen which corresponded to the hot zone. This finding was in contrast to the locations at which necking occurred for both welds, and further confirmed that the presence of a weld reduced the strength of the component.

- The strain hardening coefficient was determined at one millimetre intervals across the HAZ for each of the welds. Even though a distribution in strain hardening coefficients was determined the significance of the variation in strain hardening coefficient across the HAZ is low. The low reliability in determining significant differences in strain hardening coefficient was possibly due to the average correlation coefficient of the polynomial curve fit taken over the six increments being approximately 0.9.

7 REFERENCES

[1] C. Maharaj, J. P. Dear, and A. Morris, “A review of methods to estimate creep damage in low-alloy steel power station steam pipes,” *Strain*, vol. 45, no. 4, pp. 316–331, 2009.

[2] G. Division, W. Coast, C. Town, and W. Cape, “Eskom ’ s generation plant mix,” 2002.

[3] T. Matona, “Power System Status Update,” no. December, 2014.

[4] NERSA, “Electricity Generation: Independent Technical Audits Conductred on Twelve South African Power Stations,” no. December, 2009.

[5] F. Van Zyl, G. Von dem Bongart, M. E. . Bezuidenhiut, F. C. Havinga, P. Doubell, D. Pegler, M. Newby, and W. Smith, “Life Assessment and Creep Damage Monitoring of High Temperature and Pressure Components in South Africa’s Power Plants,” pp. 1–12, 2009.

[6] Correlated Solutions, “Digital Image Correlation : Overview of Principles and Software 2D Image Correlation Fundamentals,” *South Carolina Univ.*, 2009.

[7] M. L. Zhu and F. Z. Xuan, “Correlation between microstructure, hardness and strength in HAZ of dissimilar welds of rotor steels,” *Mater. Sci. Eng. A*, vol. 527, no. 16–17, pp. 4035–4042, 2010.

[8] K. M. Saranath, A. Sharma, and M. Ramji, “Zone wise local characterization of welds using digital image correlation technique,” *Opt. Lasers Eng.*, vol. 63, pp. 30–42, 2014.

[9] H. Fujii, L. Cui, N. Tsuji, M. Maeda, K. Nakata, and K. Nogi, “Friction stir welding of carbon steels,” *Mater. Sci. Eng. A*, vol. 429, no. 1–2, pp. 50–57, 2006.

[10] C. Xi, D. Sun, Z. Xuan, J. Wang, and G. Song, “Microstructures and mechanical properties of flash butt welded high strength steel joints,” *Mater. Des.*, vol. 96, pp. 506–514, 2016.

[11] T. H. E. Volume, C. Were, D. Leroy, T. a Siewert, S. Liu, and G. R. Edwards, “Volume Handbook . the Volume Was Prepared Under the Direction of the Asm Handbook,” *Weld. Brazing Solder.*, vol. 6, p. 2873, 1993.

[12] H. H. Cho, S. H. Kang, S. H. Kim, K. H. Oh, H. J. Kim, W. S. Chang, and H. N. Han, “Microstructural evolution in friction stir welding of high-strength linepipe steel,” *Mater. Des.*, vol. 34, pp. 258–267, 2012.

[13] F. H. T Ngoasheng, W Smith, “Title : Standard for Evaluation of Surface Microstructures Using the Metallographic Replication Technique Unique Identifier : Alternative Reference Number : N / A Area of Applicability : Physical Documentation

Type : Revision : Total Pages : Next Review D," 2014.

[14] W. D. Callister and D. G. Rethwisch, *Materials science nad engineering: An introduction*. 2009.

[15] W. J. Hall and W. J. Hall, *Welding Innovation: Advanced Arc Welding Design and Practice Worldwide*, 15th ed. The James F. Lincoln Arc Welding Foundation, 1998.

[16] T. S. Relief, P. Weld, and H. Treatment, "Post-Weld Heat Treatment – Case Studies," no. 111, pp. 111–115.

[17] B. K. Srivastava and J. Prakash, "a Review on Effect of Preheating and/or Post Weld Heat Treatmemt (Pwht) on Mechanical Behaviour of Ferrous Metals," *Int. J. Eng. Sci. Technol.*, vol. 2, no. 4, pp. 625–631, 2010.

[18] J. Trzaska, A. Jagiełło, and L. A. Dobrzañski, "The calculation of CCT diagrams for engineering steels," *Arch. Mater. Sci. Eng.*, vol. 39, no. 1, pp. 13–20, 2009.

[19] A. . Olabi and M. S. . Hashmi, "The Effect of pre- and post-weld heat treatments on the mechanical properties of electron beam welded Ti-6Al-4V alloy," *J. Mater. Process. Technol.*, vol. 55, no. 2, pp. 117–122, 1995.

[20] G. Taniguchi and K. Yamashita, "Effects of Post Weld Heat Treatment (PWHT) Temperature on Mechanical Properties of Weld Metals for High-Cr," *Kobelco Technol. Reveiew*, no. 32, pp. 33–39, 2013.

[21] C.- Mo and B. King, "University of Wollongong Thesis Collection Welding and post weld heat treatment of."

[22] D. J. Abson and J. S. Rothwell, "Review of type IV cracking of weldments in 9–12%Cr creep strength enhanced ferritic steels," *Int. Mater. Rev.*, vol. 58, no. 8, pp. 437–473, 2013.

[23] A. P. Reynolds and F. Duvall, "Digital image correlation for determination of weld and base metal constitutive behavior," *Weld. Res. Suppl.*, vol. 78, no. 10, pp. 355–360, 1999.

[24] M.-L. Zhu and F.-Z. Xuan, "Effect of microstructure on strain hardening and strength distributions along a Cr–Ni–Mo–V steel welded joint," *Mater. Des.*, vol. 65, pp. 707–715, 2015.

[25] M.-L. Zhu, D.-Q. Wang, and F.-Z. Xuan, "Effect of long-term aging on microstructure and local behavior in the heat-affected zone of a Ni–Cr–Mo–V steel welded joint," *Mater. Charact.*, vol. 87, pp. 45–61, 2014.

[26] E. J. Pavlina and C. J. Van Tyne, "Correlation of Yield strength and Tensile strength with hardness for steels," *J. Mater. Eng. Perform.*, vol. 17, no. 6, pp. 888–893, 2008.

[27] S. M. Chowdhury, D. L. Chen, S. D. Bhole, X. Cao, E. Powidajko, D. C. Weckman, and

Y. Zhou, “Tensile properties and strain-hardening behavior of double-sided arc welded and friction stir welded AZ31B magnesium alloy,” *Mater. Sci. Eng. A*, vol. 527, no. 12, pp. 2951–2961, 2010.

[28] D. R. Ni, D. L. Chen, D. Wang, B. L. Xiao, and Z. Y. Ma, “Tensile properties and strain-hardening behaviour of friction stir welded SiCp/AA2009 composite joints,” *Mater. Sci. Eng. A*, vol. 608, pp. 1–10, 2014.

[29] K. . Challenger and J. Moteff, “A correlation between strain hardneing parameters and dislocation substructure in austenitic stainless steel,” *Scr. Met.*, vol. 6, pp. 155–160, 1972.

[30] D. . LaVan, “Microtensilte properties of weld metal,” 1999.

[31] S. M. Zuniga and S. D. Sheppard, “Determining the constitutive properties of the heat-affected zone in a resistance spot weld,” *Model. Simul. Mater. Sci. Eng.*, vol. 3, pp. 391–416, 1999.

[32] R. R. Ambriz, D. Chicot, N. Benseddiq, G. Mesmacque, and S. D. De La Torre, “Local mechanical properties of the 6061-T6 aluminium weld using micro-traction and instrumented indentation,” *Eur. J. Mech. A/Solids*, vol. 30, no. 3, pp. 307–315, 2011.

[33] G. R. Song, C. F. He, X. Y. Li, Z. H. Liu, and B. Wu, “Determining the change of the HAZ mechanical properties of TA15 titanium alloy by electron beam welding with ultrasonic method,” in *Advances in Heterogeneous Material Mechanics 2008 - Proceedings of the 2nd International Conference on Heterogeneous Material Mechanics, ICHMM 2008*, 2008, pp. 1362–1365.

[34] B. S. Yilbas, S. Akhatar, and S. Z. Shuja, *Laser Forming and Welding Processees*. Switerland: Springer Internatinal Publishing, 2013.

[35] T.-L. Teng and C.-C. Lin, “Effect of welding conditions on residual stresses due to butt welds,” *Int. J. Press. Vessel. Pip.*, vol. 75, no. 12, pp. 857–864, 1998.

[36] A. R. Kohandehghan and S. Serajzadeh, “Arc welding induced residual stress in butt-joints of thin plates under constraints,” *J. Manuf. Process.*, vol. 13, no. 2, pp. 96–103, 2011.

[37] L. Tall and N. R. N. Rao, *Residual stresses in welded plates , presented at the Fall Meeting of the AWS in New York , (April L TEl*, vol. 194, no. 194. 1961.

[38] S. G. and P. J. B. Y. Sakanashi, “Measurement of local creep properties in stainless steel welds Conference Item,” *4th Int. Conf. Integr. High Temp. Welds.*, 2012.

[39] S. S. Guide, “Gleeble Systems,” *Dyn. Syst. Inc.*, vol. 1, no. 518, 2015.

[40] D. W. Walsh, M. J. Cieslak, and W. F. Savage, “Temperature measurements in

resistance-heated specimens : Longitudinal gradients," *Weld. J.*, vol. 65, no. July, pp. 184–192, 1986.

[41] W. S D, Norris I, "Application of 3D numerical modelling for thermal profile optimization on the Gleeble thermomechanical simulator," *Model. Simul. Mater. Sci. Eng.*, pp. 297–309, 1999.

[42] Y. Su, Q. Zhang, X. Xu, and Z. Gao, "Quality assessment of speckle patterns for DIC by consideration of both systematic errors and random errors Quality assessment of speckle patterns for DIC by consideration of both systematic errors and random errors," *Opt. Lasers Eng.*, vol. 86, no. September 2017, pp. 132–142, 2016.

[43] M. Van Rooyen, "Thermal Power Plant Steel Creep Deformation Measurement Using Stereo Digital Image Correlation," no. December, 2016.

[44] M. . Schreier, H., Orteu, J.J. & Sutton, "Motion and Deformation Measurements: Basic Concepts, Theory and Applications," *Image Correl. Shape*, vol. 83, no. New York: Springer, 2009.

[45] M. A. Sutton, J. H. Yan, V. Tiwari, H. W. Schreier, and J. J. Orteu, "The effect of out-of-plane motion on 2D and 3D digital image correlation measurements," *Opt. Lasers Eng.*, vol. 46, no. 10, pp. 746–757, 2008.

[46] H. Schreier and M. a. Sutton, "Systematic Errors in Digital Image Correlation Due to Undermatched Subset Shape Functions," *Exp. Mech.*, vol. 42, no. 3, pp. 303–310, 2002.

[47] B. Pan, "Bias error reduction of digital image correlation using Gaussian pre-filtering," *Opt. Lasers Eng.*, vol. 51, no. 10, pp. 1161–1167, 2013.

[48] M. A. Sutton, J. H. Yan, S. Avril, F. Pierron, and S. M. Adeeb, "Identification of heterogeneous constitutive parameters in a welded specimen: Uniform stress and virtual fields methods for material property estimation," *Exp. Mech.*, vol. 48, no. 4, pp. 451–464, 2008.

[49] Y. H. Wang, J. H. Jiang, C. Wanintrudal, C. Du, D. Zhou, L. M. Smith, and L. X. Yang, "Whole field sheet-metal tensile test using digital image correlation," *Exp. Tech.*, vol. 34, no. 2, pp. 54–59, 2010.

[50] J. S. Lyons, J. Liu, and M. a. Sutton, "High-temperature deformation measurements using digital-image correlation," *Exp. Mech.*, vol. 36, no. 1, pp. 64–70, 1996.

[51] X. Chen, N. Xu, L. Yang, and D. Xiang, "High temperature displacement and strain measurement using a monochromatic light illuminated stereo digital image correlation system," *Meas. Sci. Technol.*, vol. 23, no. 12, p. 125603, 2012.

[52] B. Pan, D. Wu, and Y. Xia, "High-temperature deformation field measurement by

combining transient aerodynamic heating simulation system and reliability-guided digital image correlation," *Opt. Lasers Eng.*, vol. 48, no. 9, pp. 841–848, 2010.

[53] B. Pan, D. Wu, and Y. Xia, "An active imaging digital image correlation method for deformation measurement insensitive to ambient light," *Opt. Laser Technol.*, vol. 44, no. 1, pp. 204–209, 2012.

[54] B. Pan, Z. Lu, and H. Xie, "Mean intensity gradient : An effective global parameter for quality assessment of the speckle patterns used in digital image correlation," *Opt. Lasers Eng.*, vol. 48, no. 4, pp. 469–477, 2010.

[55] G. Crammond, S. W. Boyd, and J. M. Dulieu-barton, "Speckle pattern quality assessment for digital image correlation," *Opt. Lasers Eng.*, vol. 51, no. 12, pp. 1368–1378, 2013.

[56] B. Pan, D. Wu, Z. Wang, and Y. Xia, "High-temperature digital image correlation method for full-field deformation measurement at 1200 °C," *Meas. Sci. Technol.*, vol. 22, no. 1, p. 015701, 2010.

[57] B. Swaminathan, J. Lambros, and H. Sehitoglu, "Digital image correlation study of mechanical response of nickel superalloy Hastelloy X under thermal and mechanical cycling: Uniaxial and biaxial stress states," *J. Strain Anal. Eng. Des.*, vol. 49, no. 4, pp. 233–243, 2013.

[58] D. Wittevrongel, L., Lava, P., Lomov, S. V. & Debruyne, "A Self Adaptive Global Digital Image Correlation Algorithm," *Exp. Mech.*, vol. 55, pp. 361–378, 2015.

[59] B. Pan, H. Xie, Z. Wang, K. Qian, and Z. Wang, "Study on subset size selection in digital image correlation for speckle patterns," vol. 16, no. 10, pp. 967–974, 2008.

[60] L. Schäfer, "Influence of delta ferrite and dendritic carbides on the impact and tensile properties of a martensitic chromium steel," *J. Nucl. Mater.*, vol. 258–263, pp. 1336–1339, 1998.

[61] I. Farup, "Gleeble Machine Determination of Creep Law Parameters for Thermally Induced Deformations in Aluminium Dc Casting," *J. Therm. Stress.*, vol. 23, pp. 47–58, 2000.

[62] K. J. F, *Some effects of hydrostatic tension on the fracture behaviour of mild steel*. J. Iron Steel Inst., 1966.

[63] D. D. E, *Mechanical Metallurgy*. New York: McGraw-Hill, 1992.

[64] L. Jang, L. Smith, A. Gothekar, and X. Chen, "Measure Strain Distribution Using Digital Image Correlation (DIC) for Tensile Tests," pp. 1–27, 2010.

[65] S. R. Kalidindi, a. Abusafieh, and E. El-Danaf, "Accurate characterization of machine

compliance for simple compression testing," *Exp. Mech.*, vol. 37, no. 2, pp. 210–215, 1997.

[66] S. Singh, "ENGG & TECHNOLOGY DEPARTMENT OF PRODUCTION ENGINEERING SUBJECT : MECHANICAL WORKING OF METALS," *ENGG Technol. Dep. Prod. Eng.*, vol. 5.

[67] Y. Bergstr and G. It, "The Hollomon n – value , and the strain to necking in steel," no. February, pp. 1–10, 2011.

[68] B. Benny, "Use of Hollomon equation in combination with conventional equation , for finding change in strain hardening exponent value , among differently aged and tensile tested maraging steel samples," vol. 2, no. December, pp. 6–8, 2016.

[69] M. Van Rooyen and T. H. Becker, "High-temperature tensile property measurements using digital image correlation over a non-uniform temperature field," vol. 53, no. 3, pp. 117–129, 2018.

[70] Eskom, "Turbine power plant manual," 2007.

[71] P. Vince and C. Janet, "Spectrographic (Compositional) Analysis on steam penetration," *One Eighty*, no. R-MA11-06-1, p. 55, 2015.

[72] S. Mehluleli and L. Lunga, "Spectrographic (Compositional) Analysis on turbine housing weld," *One Eighty*, no. R-MA11-08-1, p. 2016, 2016.

[73] P. Vince and L. Lunga, "Spectrographic (Compositional) Analysis on loop pipe weld," *One Eighty*, no. R-MA-11-09-1, p. 78, 2016.

[74] N. Farabi, D. L. Chen, and Y. Zhou, "Tensile properties and work hardening behavior of laser-welded dual-phase steel joints," *J. Mater. Eng. Perform.*, vol. 21, no. 2, pp. 222–230, 2012.

[75] M. Physics, "Springs in Series." [Online]. Available: https://notendur.hi.is/eme1/skoli/edl_h05/masteringphysics/13/springinseries.htm. [Accessed: 30-Jan-2017].

8 APPENDICES

8.1 DRAWINGS OF THE TENSILE SPECIMENTS

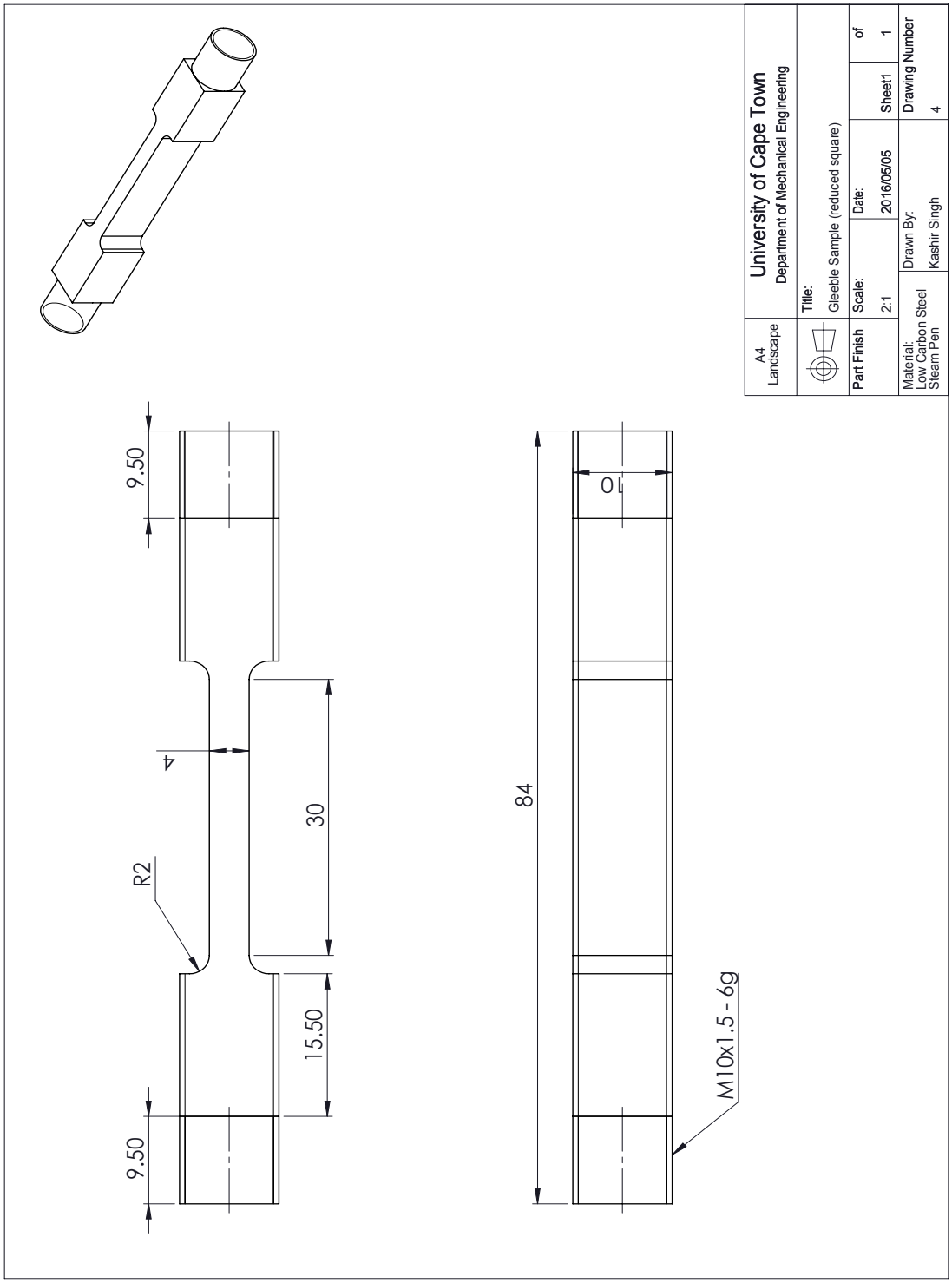

8.2 DRAWINGS OF THE GLEEBLE STIFF LOAD TRAIN COMPONENTS

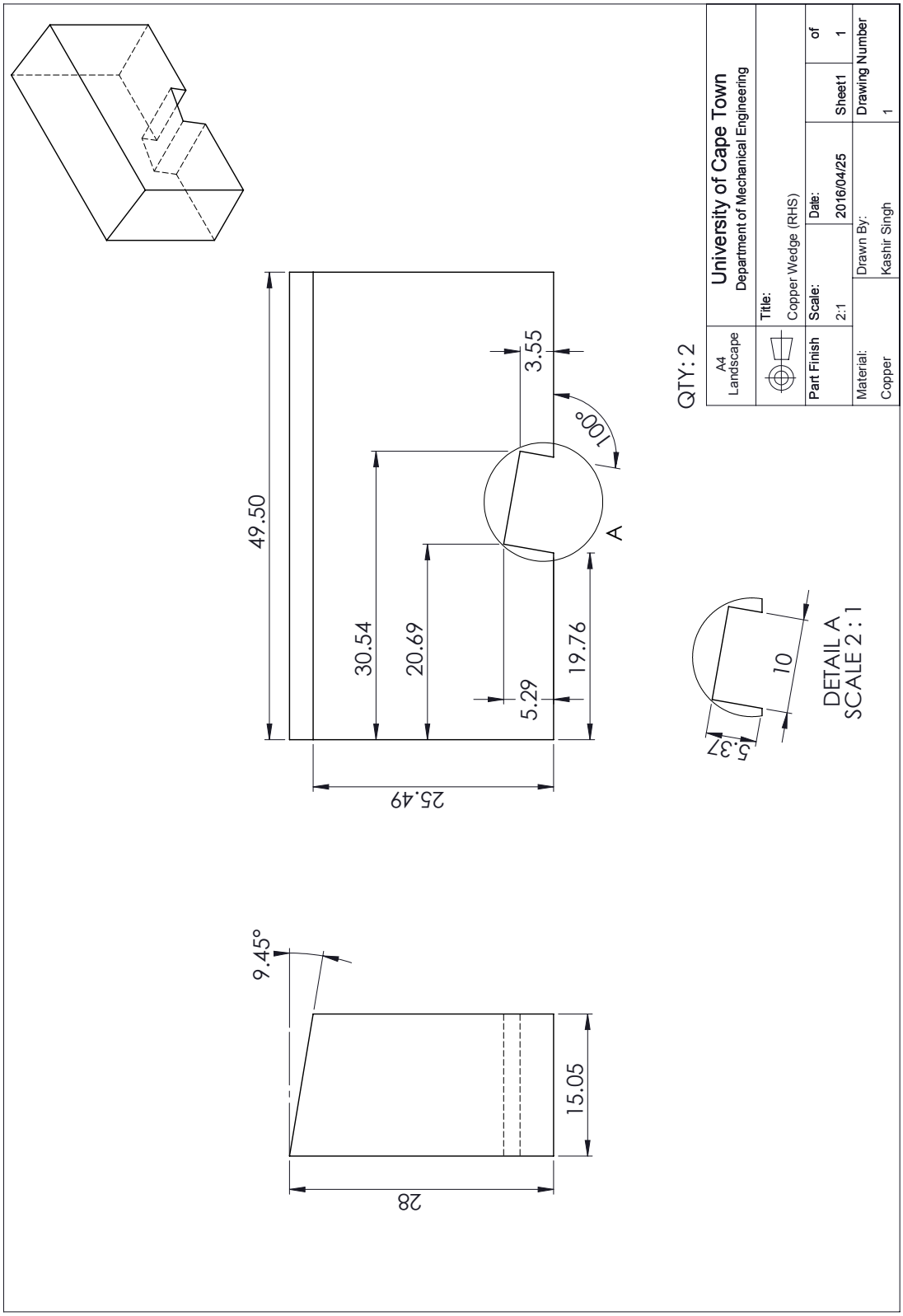

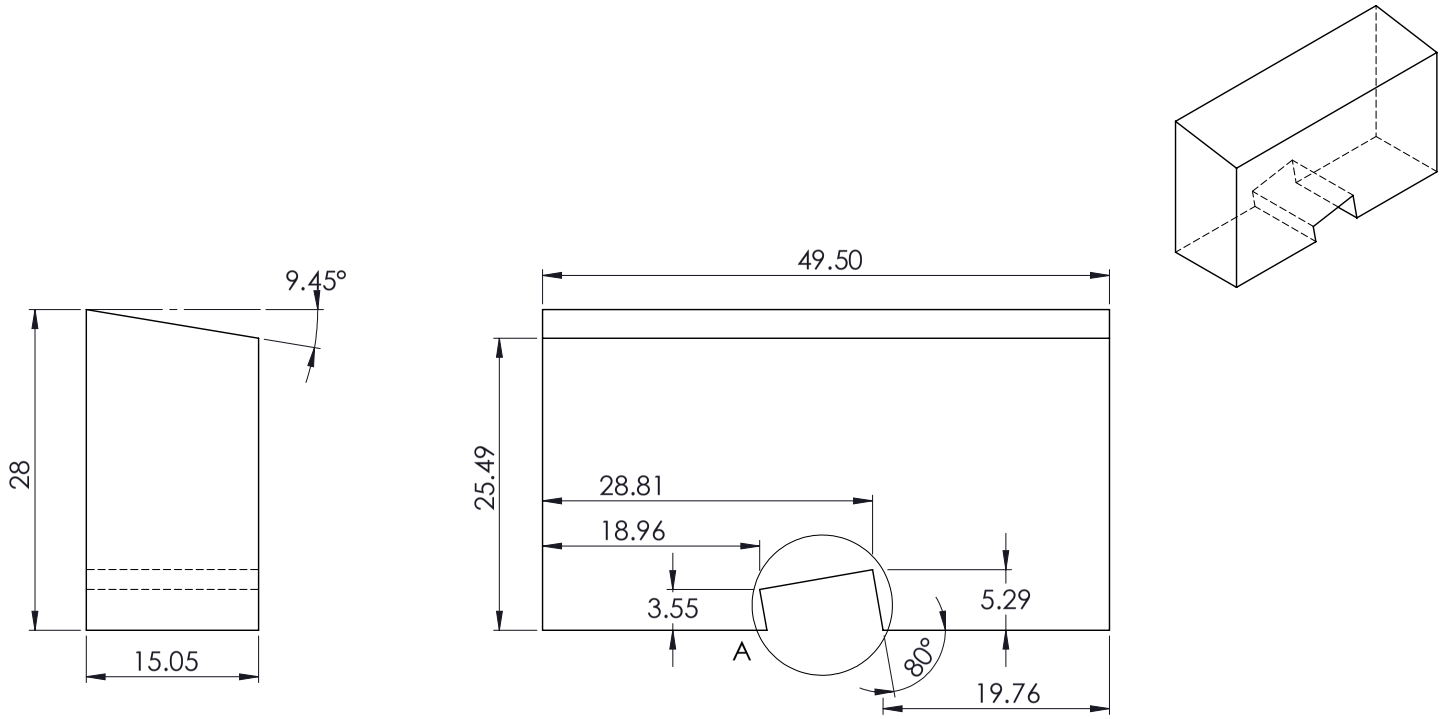

DETAIL A
SCALE 2 : 1

QTY: 2

A4 Landscape	University of Cape Town Department of Mechanical Engineering			
	Title: Copper Wedge (LHS)			
Part Finish	Scale: 2:1	Date: 2016/04/25	Sheet1	of 1
Material: Copper	Drawn By: Kashir Singh		Drawing Number 2	

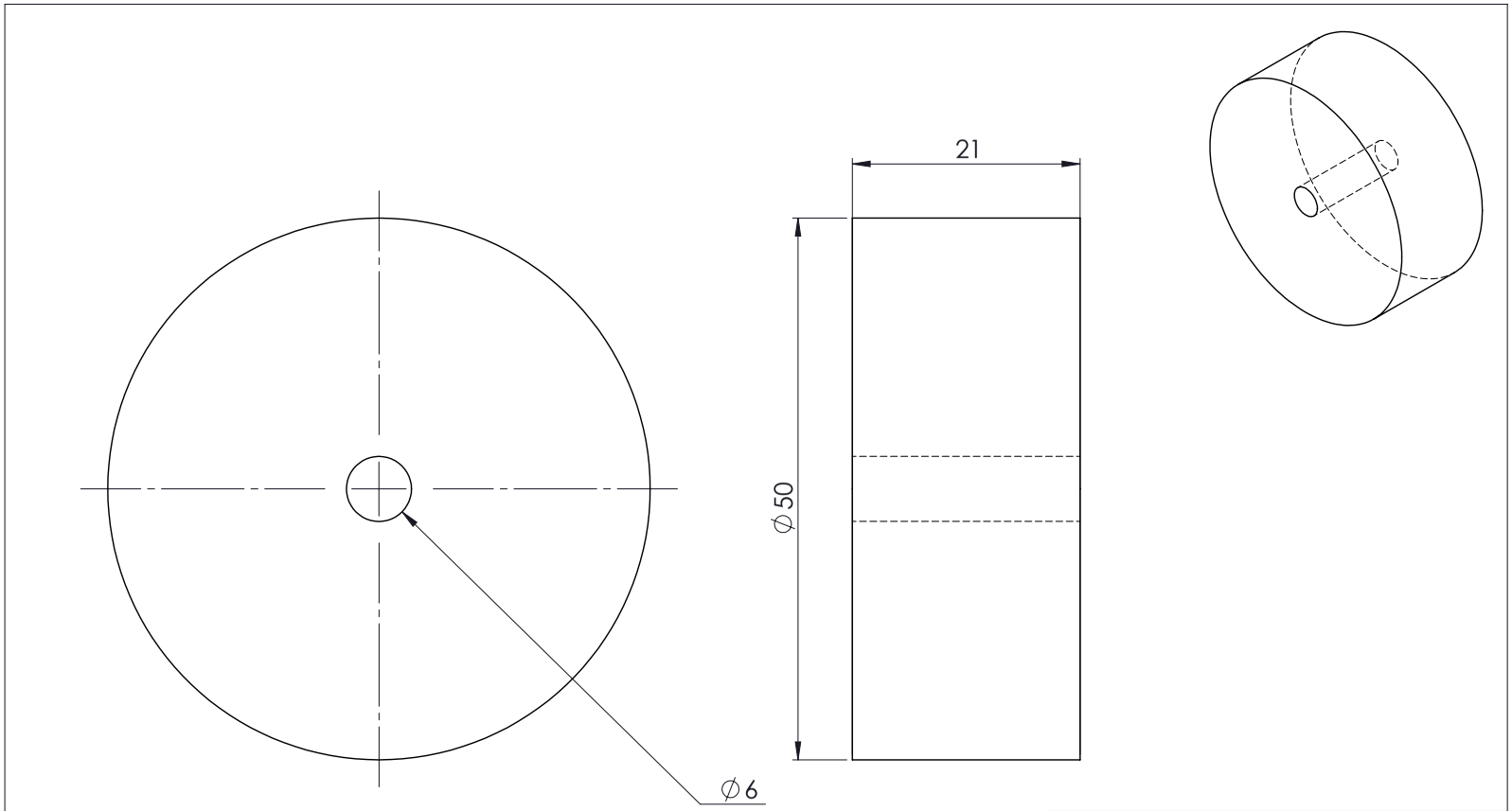

A4 Landscape	University of Cape Town Department of Mechanical Engineering			
	Title: End Spacer			
Part Finish	Scale: 2:1	Date: 2016/03/15	Sheet1	of 1
Material: Ferritic Stainless Steel	Drawn By: Kashir Singh		Drawing Number 3	

Parent Material – Steam Penetration

R-MA11-06-1

ONE EIGHTY MATERIALS TESTING (PTY) LTD - TEST REPORT			
ONE EIGHTY MATERIALS TESTING (PTY) LTD	**DATE:**	21/08/2015	
	CLIENT PO NO:	-	
Postnet Suite 78, Private Bag X11, Mowbray, Cape Town	**REPORT NUMBER:**	R-MA11-06-1	
	AUTHOR:	Vince Phasha	
Building 23B, Unit 15, The Waverley Business Park, Mowbray	**TECHNICAL SIGNATORY:**	Janet Cotton	
+27 21 447 5258/4643	**WITNESSED BY:**	-	**Reg No** 2007/007050/07
+27 86 617 1047	**TESTED BY:**	Vince Phasha	**Director** JA Cotton BSc (Eng) PhD (Mat Eng UCT)

Chemical Composition of carbon Steel Sample

Carbon Steel Sample												
Symbol:	**C**	**Si**	**Mn**	**P**	**S**	**Cr**	**Mo**	**Ni**	**Cu**	**Al**	**V**	**Fe**
Unit:	**%**	**%**	**%**	**%**	**%**	**%**	**%**	**%**	**%**	**%**	**%**	**%**
Tests 1	0.237	0.273	0.653	0.019	0.0073	1.31	0.688	0.097	0.132	0.033	0.264	96.03
Tests 2	0.237	0.259	0.65	0.018	0.0078	1.329	0.687	0.092	0.128	0.032	0.264	96.06
Tests 3	0.235	0.262	0.656	0.018	0.0083	1.333	0.687	0.094	0.129	0.032	0.264	96.03
Tests 4	0.233	0.255	0.658	0.017	0.0073	1.345	0.694	0.091	0.128	0.034	0.266	96.04
Tests 5	0.237	0.26	0.656	0.018	0.0078	1.333	0.698	0.093	0.129	0.032	0.267	96.03
Average	**0.236**	**0.262**	**0.655**	**0.018**	**0.008**	**1.330**	**0.691**	**0.093**	**0.129**	**0.033**	**0.265**	**96.038**
AISI 6118H	**0.15-0.21**	**0.15-0.35**	**0.40-0.80**	**0.035 Max**	**0.04 max**	**0.40-0.80**	**-**	**0.25 max**	**0.35 xax**	**-**	**0.10-0.15**	**Rem.**

Material closely matches AISI 6118H-Steel with highlighted elements slightly out of range

OFFSITE TESTING DONE:
None
OFFSITE MACHINING DONE:
None

One Eighty Test Methods Used	
Samples Received Date:	08/2015
Test Methods used – SANAS Accredited	☐ OE-TSP-03 TM01 Tensile Testing Metals ☐ OE-TSP-03 TM03 Impact Testing Metals ☐ OE-TSP-03 TM011 Bend Tests ☐ OE-TSP-03 TM05 Vickers Hardness Testing ☑ OE-TSP-03 TM06 Spectrometric Analysis ☐ OE-TSP-03 TM07 Spectrometric Analysis Handheld – **NOT SANAS Accredited** ☐ OE-TSP-03 TM08 Microstructural Analysis
For the Customer's Information	
PLEASE NOTE: Samples will be kept for **1 month** from this report date. Please collect within this time, otherwise ALL samples/material will be scrapped, as we do not provide a storage service.	

Weld Material – Loop Pipe Weld

R-MA09-11-1.xlsx

ONE EIGHTY MATERIALS TESTING (PTY) LTD - TEST REPORT		
ONE EIGHTY MATERIALS TESTING (PTY) LTD	**DATE:**	31/03/2016
	REPORT NUMBER:	R-MA11-09-1
Postnet Suite 78, Private Bag X11, Mowbray, Cape Town	**AUTHOR:**	Vince Phasha
Building 23B, Unit 15, The Waverley Business Park, Mowbray	**TECHNICAL SIGNATORY:**	Lunga Lusasa
Tel +27 21 447 5258/4643	**WITNESSED BY:**	-
Fax +27 86 617 1047	**TESTED BY:**	V. Phasha
	CLIENT:	Material Engineering, UCT
	CLIENT PO NO:	1495926
	CLIENT ADDRESS:	UCT, Library Rd, Upper Campus

ONE EIGHTY MATERIALS TESTING

sanas Testing Laboratory T0593

Reg No 2007/007050/07

Director JA Cotton BSc (Eng) PhD (Mat Eng UCT)

Composition Analysis of Carbon Steel

Elements (Wt%):	C	Si	Mn	P	S	Cr	Mo	Ni	Cu	Al	Ti	V	W	Fe
1.Measurement:	0.085	0.319	0.915	0.013	0.0098	0.465	0.948	0.025	0.027	0.0039	0.011	0.475	0.028	96.59
2.Measurement:	0.084	0.32	0.915	0.013	0.0096	0.462	0.943	0.025	0.027	0.0036	0.011	0.477	0.026	96.60
3.Measurement:	0.085	0.324	0.919	0.013	0.0097	0.464	0.944	0.026	0.027	0.0043	0.011	0.476	0.024	96.59
4.Measurement:	0.085	0.323	0.92	0.013	0.0093	0.461	0.946	0.026	0.027	0.004	0.011	0.477	0.027	96.58
5.Measurement:	0.085	0.326	0.927	0.013	0.0097	0.466	0.952	0.027	0.027	0.0043	0.011	0.482	0.027	96.55
Average	**0.085**	**0.322**	**0.919**	**0.013**	**0.0096**	**0.464**	**0.947**	**0.026**	**0.027**	**0.0040**	**0.011**	**0.477**	**0.026**	**96.58**

OFFSITE TESTING DONE:
None
OFFSITE MACHINING DONE:
None

One Eighty Test Methods Used	
Samples Received Date:	03/2016
Test Methods used – SANAS Accredited	☐ OE-TSP-03 TM01 Tensile Testing Metals
sanas Testing Laboratory T0593	☐ OE-TSP-03 TM03 Impact Testing Metals (KV_8)
	☐ OE-TSP-03 TM011 Bend Tests
	☐ OE-TSP-03 TM05 Vickers Hardness Testing
	☑ OE-TSP-03 TM06 Spectrometric Analysis
	☐ OE-TSP-03 TM07 Spectrometric Analysis Handheld – **NOT SANAS Accredited**
	☐ OE-TSP-03 TM08 Microstructural Analysis
	☐ Other, please state:
For the Customer's Information	
PLEASE NOTE: Samples will be kept for 1 month from this report date. Please collect within this time, otherwise ALL samples/material will be scrapped, as we do not provide a storage service.	

Weld Material – Turbine Housing Weld

R-MA11-04-1.xlsx

ONE EIGHTY MATERIALS TESTING (PTY) LTD - TEST REPORT		
ONE EIGHTY MATERIALS TESTING (PTY) LTD	**DATE:**	02/02/2016
Postnet Suite 78, Private Bag X11, Mowbray, Cape Town	**REPORT NUMBER:**	R-MA11-08-1
	AUTHOR:	Mehluleli Sibanda
Building 23B, Unit 15, The Waverley Business Park, Mowbray	**TECHNICAL SIGNATORY:**	Lunga Lusasa
	WITNESSED BY:	-
Tel +27 21 447 5258/4643	**TESTED BY:**	Mehluleli Sibanda
Fax +27 86 617 1047	**CLIENT:**	Materials Engineering
	CLIENT PO NO:	1484844
	CLIENT ADDRESS:	UCT, Rondebosch

ONE EIGHTY MATERIALS TESTING

sanas Testing Laboratory T0593

Reg No 2007/007050/07

Director JA Cotton BSc (Eng) PhD (Mat Eng UCT)

Spectrographic (Compositional) Analysis on weld sample

Elements	C	Si	Mn	P	S	Cr	Mo	Ni	Cu	Al	V	Fe
Unit	%	%	%	%	%	%	%	%	%	%	%	%
Test 1	0.060	0.459	0.685	0.006	0.008	0.661	0.500	0.083	0.114	0.003	0.249	97.03
Test 2	0.059	0.455	0.686	0.006	0.008	0.657	0.499	0.082	0.114	0.002	0.248	97.05
Test 3	0.059	0.463	0.690	0.006	0.008	0.658	0.501	0.082	0.114	0.002	0.249	97.04
Test 4	0.060	0.462	0.682	0.006	0.008	0.652	0.499	0.080	0.113	0.002	0.246	97.06
Test 5	0.060	0.460	0.683	0.006	0.008	0.654	0.499	0.079	0.113	0.002	0.246	97.06
Average	**0.060**	**0.460**	**0.685**	**0.0057**	**0.0078**	**0.656**	**0.500**	**0.081**	**0.114**	**0.0022**	**0.248**	**97.05**

OFFSITE TESTING DONE:
None
OFFSITE MACHINING DONE:
None

One Eighty Test Methods Used	
Samples Received Date:	02/2016
Test Methods used – SANAS Accredited	☐ OE-TSP-03 TM01 Tensile Testing Metals
	☐ OE-TSP-03 TM03 Impact Testing Metals (KV_8)
	☐ OE-TSP-03 TM011 Bend Tests
	☐ OE-TSP-03 TM05 Vickers Hardness Testing
	☑ OE-TSP-03 TM06 Spectrometric Analysis
	☐ OE-TSP-03 TM07 Spectrometric Analysis Handheld – **NOT SANAS Accredited**
	☐ OE-TSP-03 TM08 Microstructural Analysis
	☐ Other, please state:
For the Customer's Information	
PLEASE NOTE: Samples will be kept for 1 month from this report date. Please collect within this time, otherwise ALL samples/material will be scrapped, as we do not provide a storage service.	

8.4 LOOP PIPE WELD REPEAT EXPERIMENTS

Figure 8.3-1: Strain and thermal distribution across the LPW gauge length at (a) RT, (b) 300 ^{o}C and (c) 535 ^{o}C

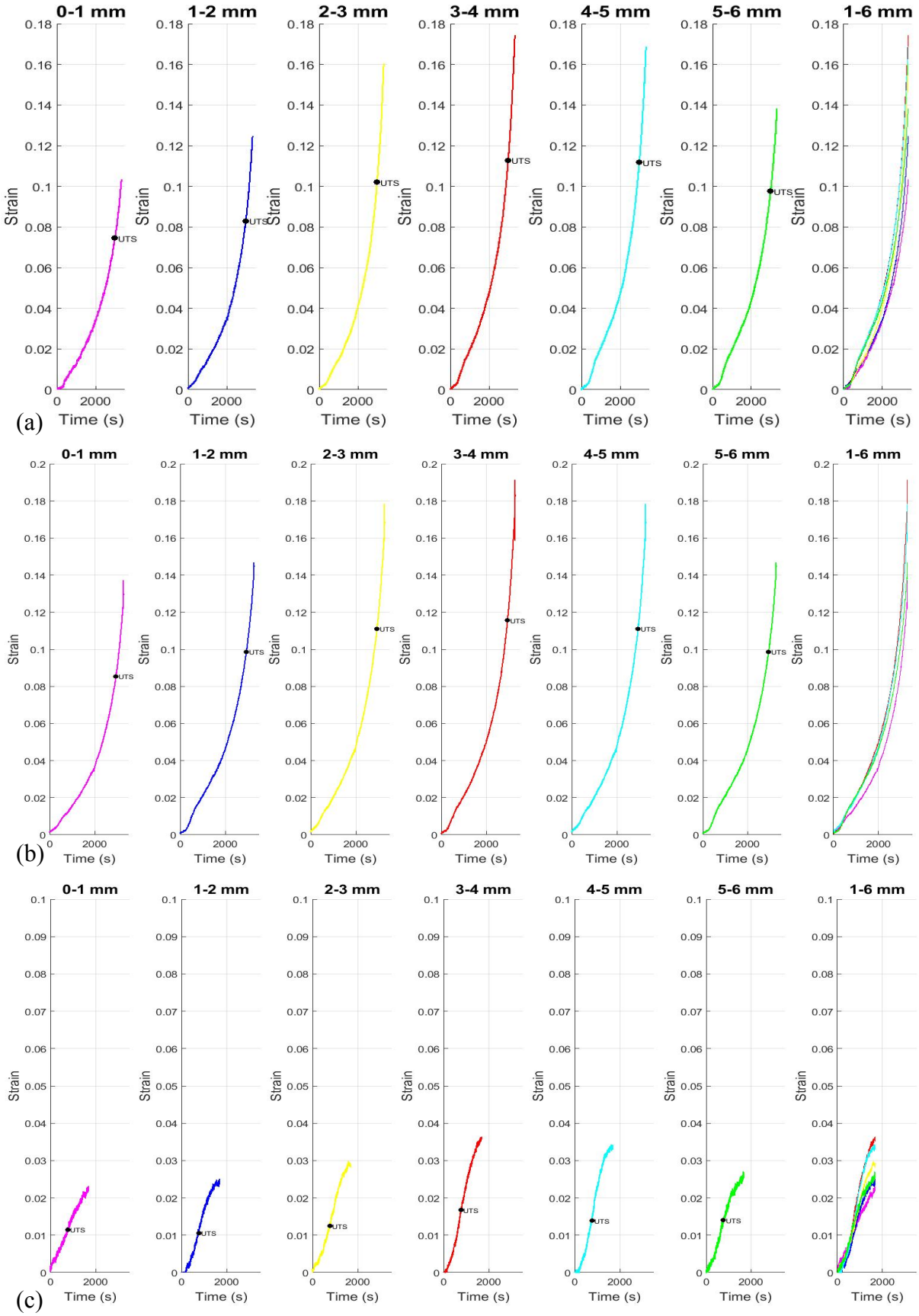

Figure 8.4-2: Incremental strain distribution across the LPW HAZ at (a) RT, (b) 300 ^{o}C and (c) 535 ^{o}C

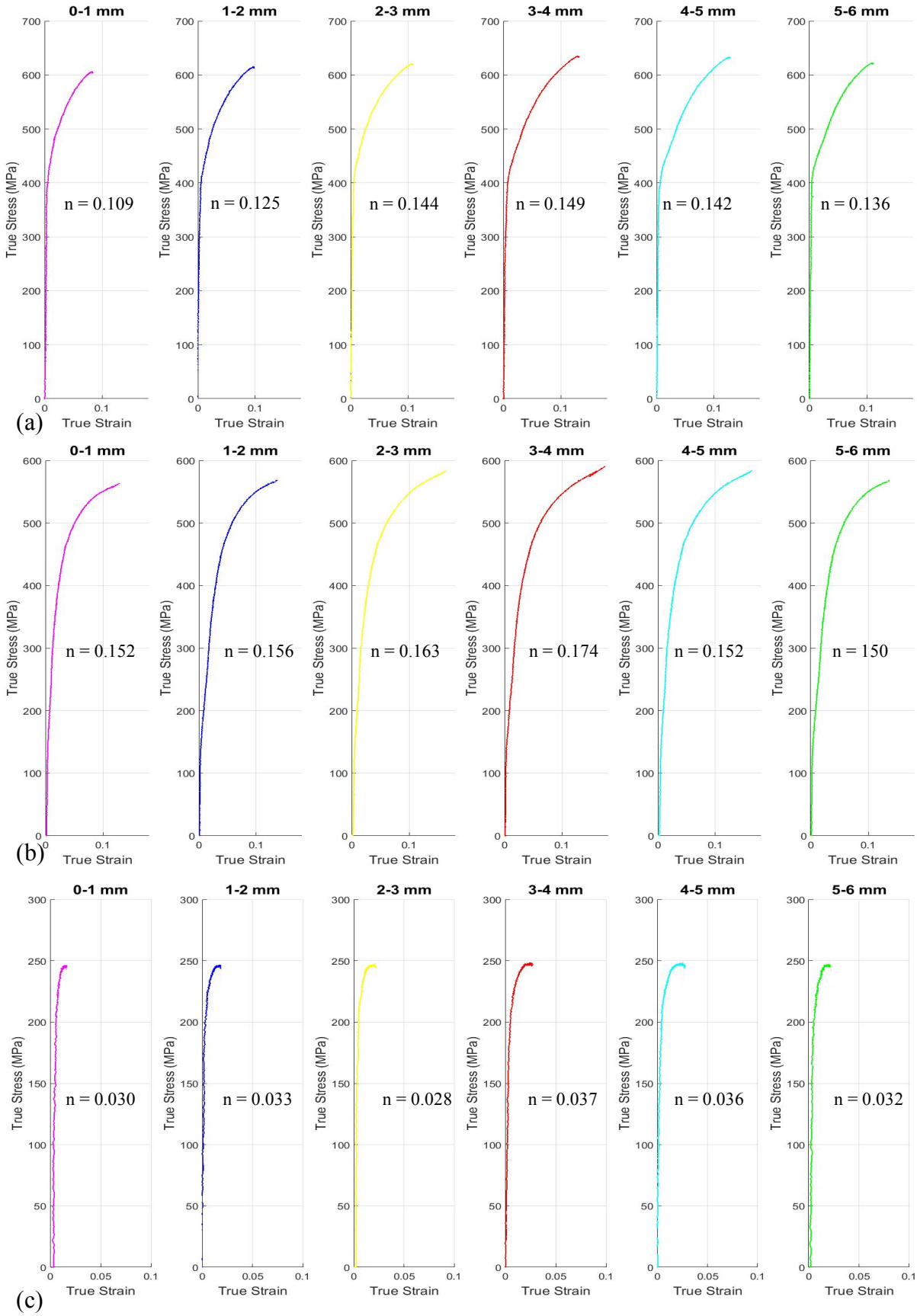

Figure 8.4-3: Incremental true stress - true strain curves of the LPW at (a) RT, (b) 300 ^{o}C and (c) 535 ^{o}C

8.5 TURBINE HOUSING WELD REPEAT EXPERIMENTS

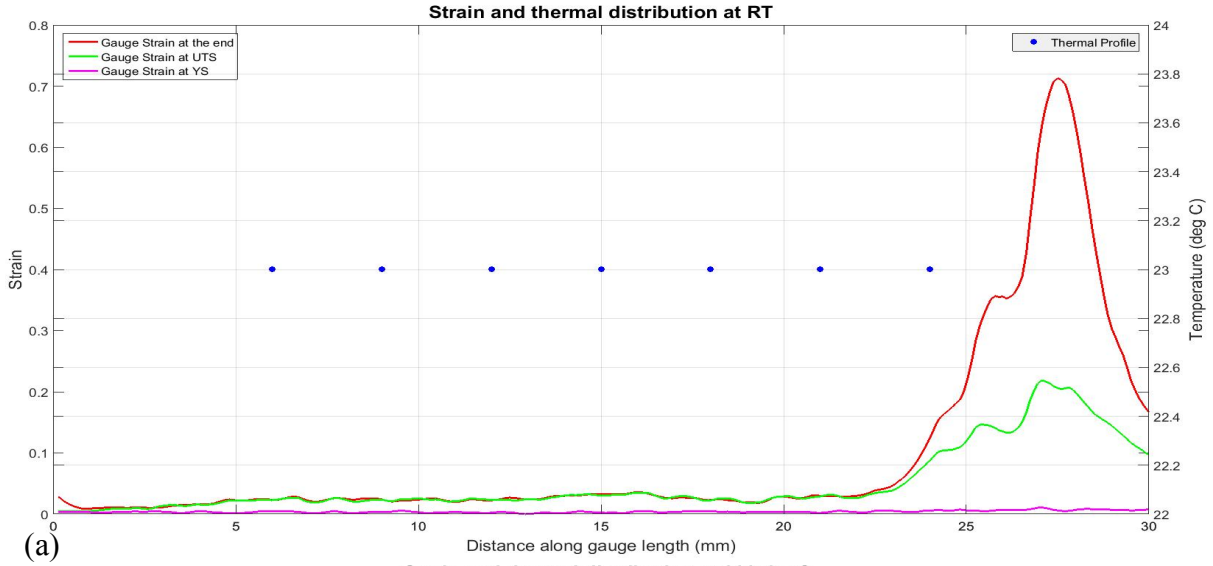

(a)

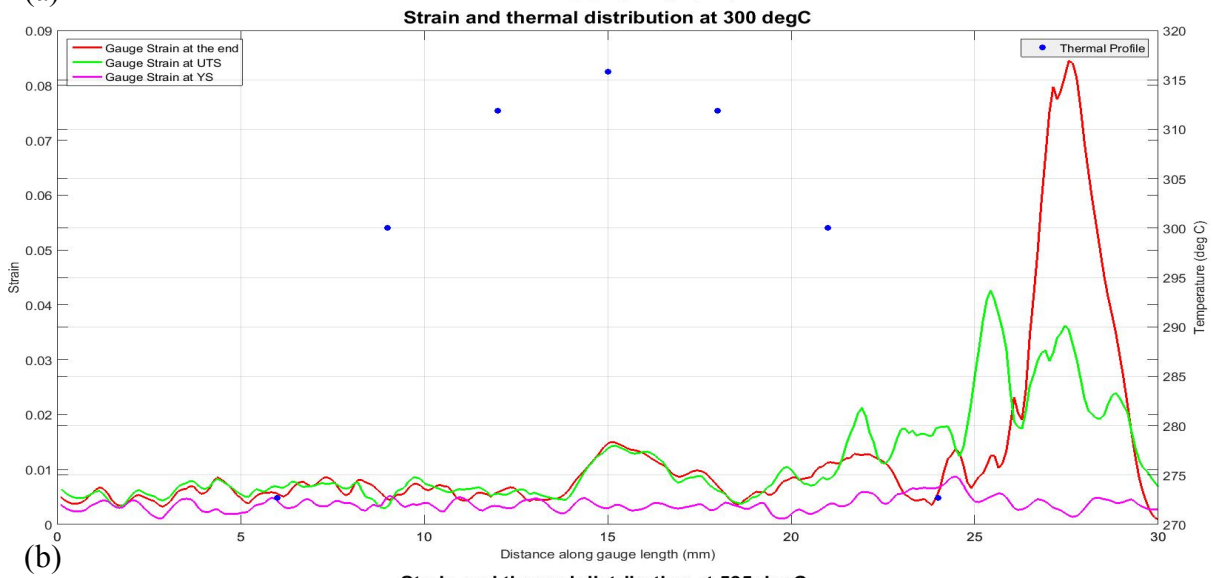

(b)

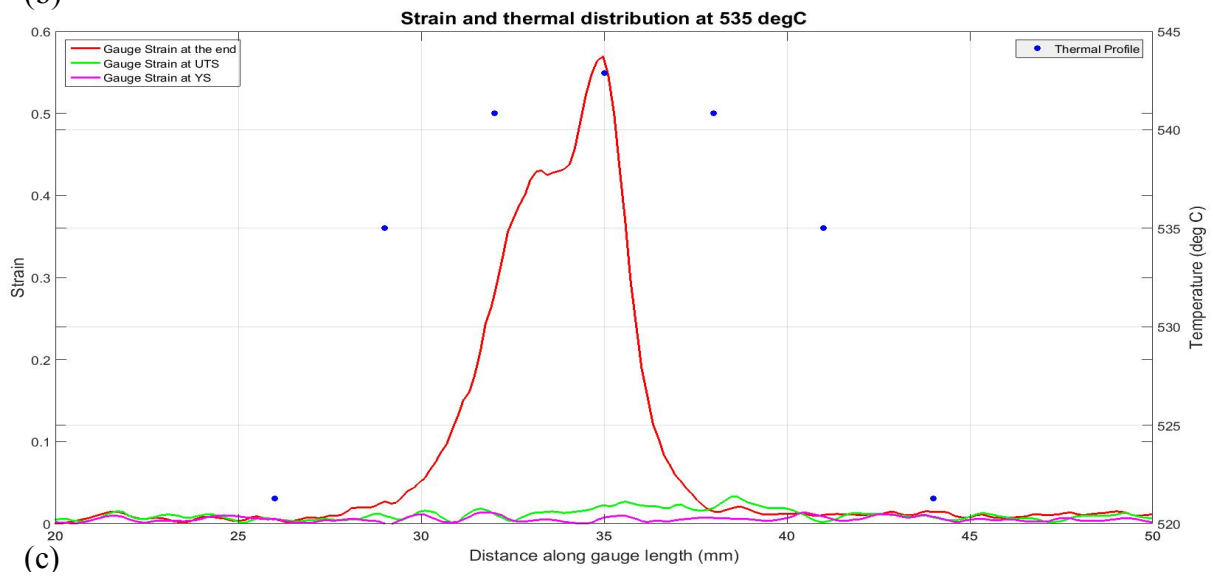

(c)

Figure 8.4-1: Strain and thermal distribution across the THW gauge length at (a) RT, (b) 300 ^{o}C and (c) 535 ^{o}C.

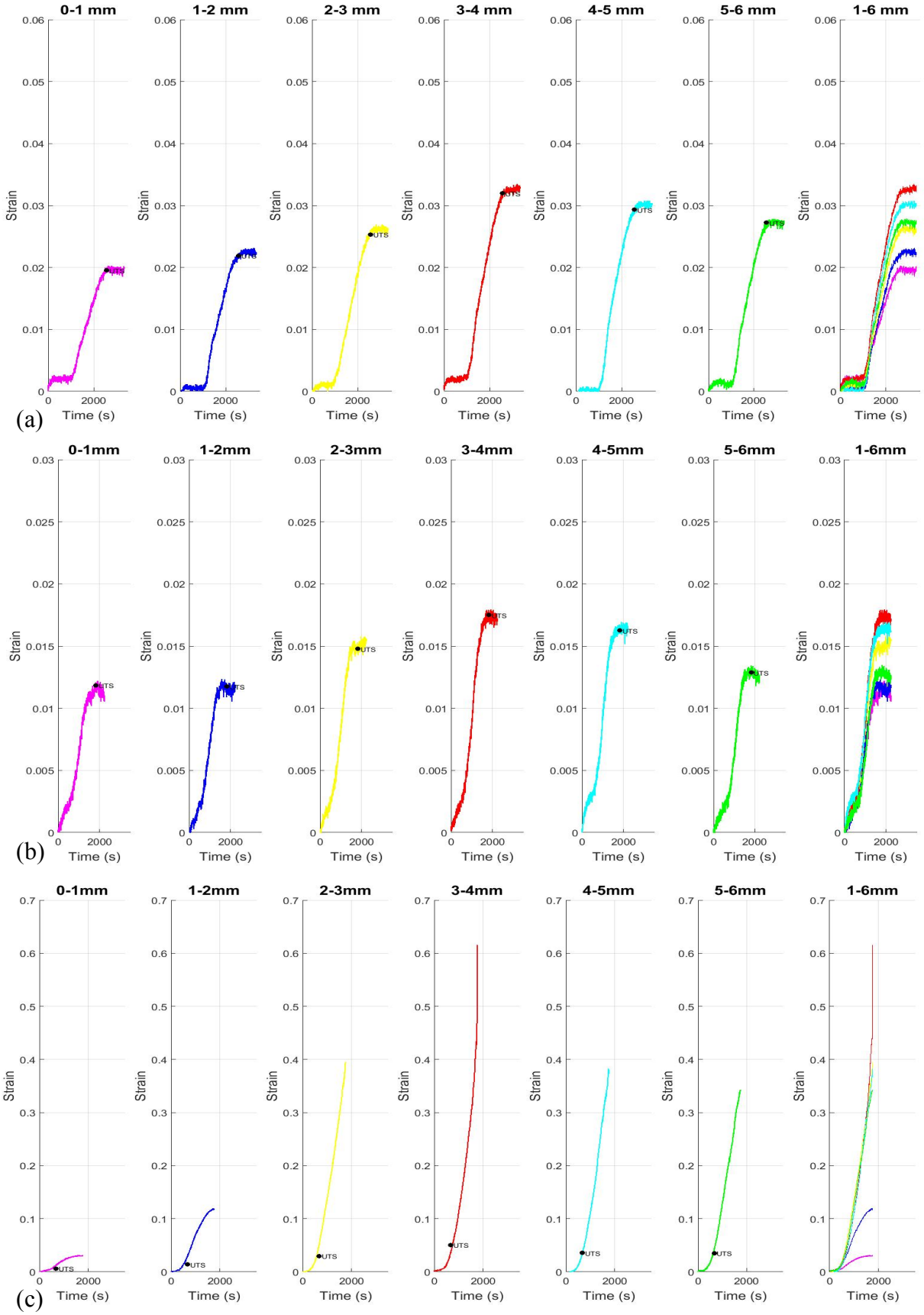

Figure 8.5-2: Incremental strain distribution across the THW HAZ at (a) RT, (b) 300 ^{o}C and (c) 535 ^{o}C

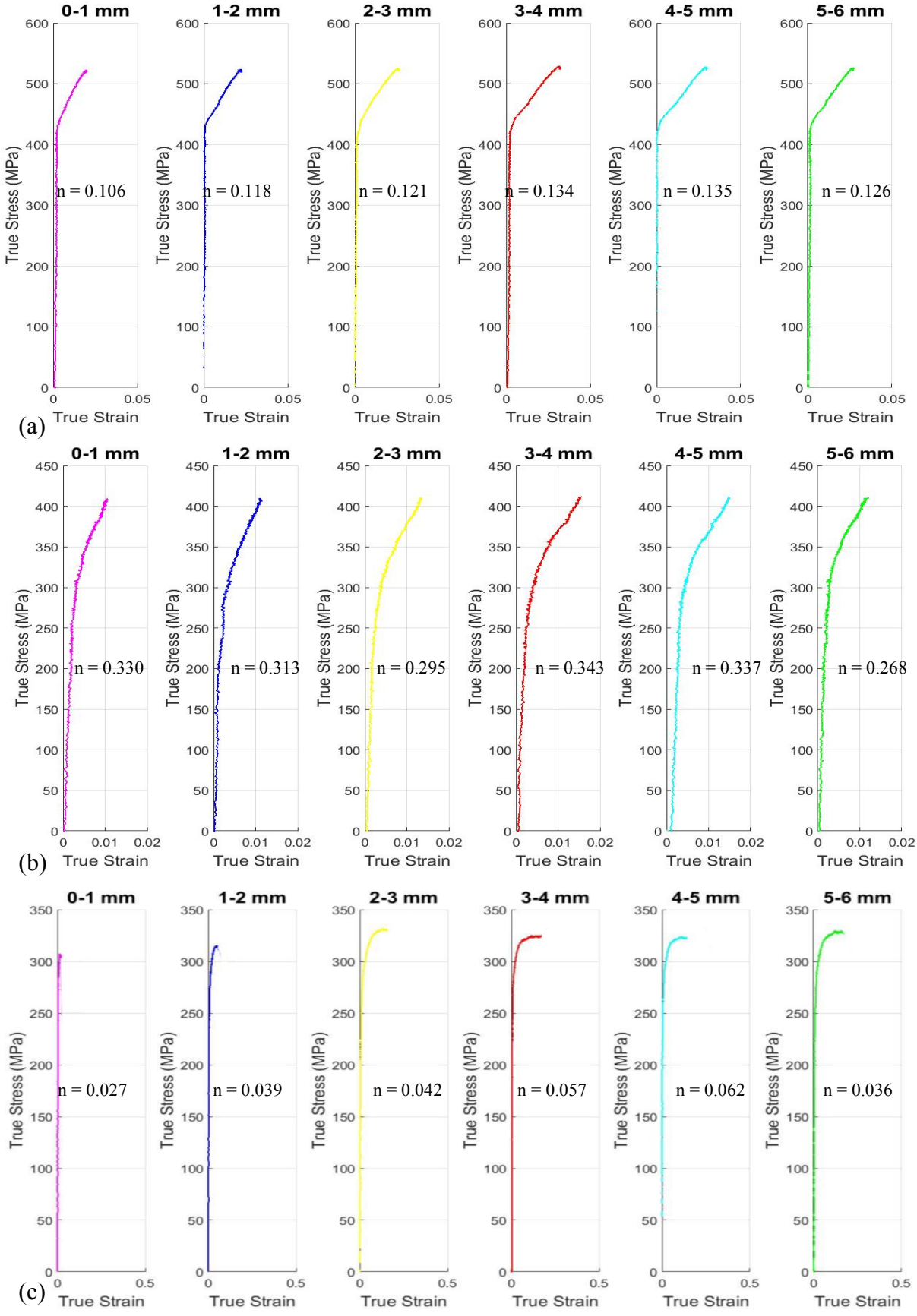

Figure 8.5-3: Incremental true stress - true strain curves of the THW at (a) RT, (b) 300 ^{o}C and (c) 535 ^{o}C